School of Computer Engineering and Telecommunications

Department of Computer Science and Artificial Intelligence

University of Granada

Ph.D. Thesis Dissertation:

Image Super Resolution Using Compressed Sensing Observations

Written by:

Wael H. AlSaafin

Supervised by:

Dr. Miguel Vega

Dr. Rafael Molina

Doctorate Program in Information and Communication Technologies

Editor: Universidad de Granada. Tesis Doctorales
Autor: Wael Hasan Abdallah Alsaafin
ISBN: 978-84-9125-921-3
URI: http://hdl.handle.net/10481/43889

El doctorando D. Wael H. AlSaafin y los directores de la tesis Dr. Miguel Vega y Dr. Rafael Molina, Profesores Titular y Catedrático de Universidad, respectivamente, del Departamento de Lenguajes y Sistemas Informáticos y Ciencias de la Computación e Inteligencia Artificial respectivamente, de la Universidad de Granada

GARANTIZAMOS AL FIRMAR ESTA TESIS DOCTORAL

que el trabajo ha sido realizado por el doctorando bajo nuestra dirección y, hasta donde nuestro conocimiento alcanza, en la realización del trabajo se han respetado los derechos de otros autores a ser citados, cuando se han utilizado sus resultados o publicaciones.

Granada, a 28 de Marzo de 2016

Directores de la Tesis

Dr. Miguel Vega

Dr. Rafael Molina

El Doctorando

D. Wael H. AlSaafin

Dedications

To my family...
Especially Ahmad, Mohammad, and Saad

Acknowledgements

It was a great job, full of hardworking and determination. It could not succeed without the help and support I could receive. Thanks to my supervisors Rafael Molina and Miguel Vega. Thanks also to Aggelos Katssagelos, Javier Mateos, Salvador Villena, Bruno Amizic, and Gokhan Bilgin, and my colleagues in CITIC for their cooperation and assistance. Thanks to University of Granada, Yildiz Technical University and Erasmus Mundus program.
Thank you all, you have made it an unforgettable successful period.

Wael

Contents

Resumen y Conclusiones **xxi**

Summary and Conclusions **xxv**

1 Introduction **1**

1.1 Background 2

1.1.1 Classical Digital Imaging 2

1.1.2 Color Images 3

1.1.3 Millimeter Wave Images 4

1.1.4 Super Resolution 6

1.1.5 Compressed Sensing 11

1.2 Objectives and Hypothesis 14

1.3 Methodology and Contributions 14

1.4 Thesis Document Structure 15

2 State of the Art **17**

2.1 Image Super Resolution Works 17

2.1.1 Image Regularizers 18

2.1.2 Image Registration 20

2.1.3 Blur Model 21

2.2 Compressed Sensing Works 22

2.3 CSSR Modeling and Formulation 23

3 Compressive Sensing Super Resolution Algorithm 33

3.1 Preliminary Work 33

3.2 The Proposed CSSR Approach 39

3.2.1 HR Image Estimation 40

3.2.2 Transformed Coefficient Estimation 41

3.2.3 Registration from Estimated HR Image 42

3.2.4 Registration from Estimated LR Reference Image 43

3.2.5 CSSR Algorithm Statement 44

3.3 Proposed Color CSSR (CCSSR) 44

3.3.1 Modeling and Problem Formulation 44

3.3.2 CCSSR Optimization Approach 45

3.3.3 CCSSR Algorithm Statement 48

4 Experimental Results 49

4.1 Quality Assessment 49

4.2 Intra CSSR Analysis 50

4.2.1 CS Reconstruction 50

4.2.2 Registration Estimation 54

4.3 CSSR vs ID Works 59

4.4 CSSR vs SR Works 59

4.5 CSSR: The General Case 71

4.5.1 CSSR from a single image 74

4.5.2 CSSR vs Sequential Approach 85

4.5.3 CSSR1 vs CSSR2 86

4.6 CSSR of PMMW Images 92

4.7 CCSSR of Color Images 94

5 Conclusions and Future Work 103

5.1 Conclusions 103

5.2 Future work 104

Bibliography **105**

List of Figures

1.1 Image representation: (a) gray scale image for the letter 'a', (b) exaggerated version of the image (×16), (c) the corresponding pixel values. 3

1.2 RGB color Image. (a) Original RGB image, (b) Red channel, (c) Green channel, (d) Blue channel. (Adapted from [1]). 4

1.3 YCbCr colored image. 5

1.4 Electromagnetic wave spectrum 5

1.5 PMMW threat detect system. 6

1.6 Sample PMMW image of a man. 7

1.7 Illustartion of SR process 7

1.8 Degradation process illustrative example. (a) 256×256 Original Cameraman image, (b) Warped image, $\theta = -0.1047 rad$, $c = 3$, $d = 2$, (c) Blurred image, Gaussian blur with variance 3, (d) 64×64 Down-sampled image, P=4, (e) Noised image, white Gaussian noise SNR=40dB 8

1.9 SR Estimation. Upper part: three LR images each of resolution= 9. Lower part: estimated HR image of resolution=36, formed by the original pixels in LR observation and the crossings made by the red dashed lines (P=2). 10

1.10 Bilinear interpolation. Given $\mathbf{x}$ at four neighboring pixels, find the intensity value at (m, n) 11

1.11 Typical CS camera 12

1.12 Compressed sensing acquisition model. Measurement matrix $\mathbf{\Phi}$ with real entries, M=8, N=16 13

2.1 q-th HR grid calculation. (a) HR grid (in black) and the q-th image grid (in red), (b) Detailed view of (a), with the pixel notation used for the bilinear interpolation of grid element (u_q, v_q) 25

2.2 Simulation process. Warped with motion vectors $(0,0,0)^t$, $(.0524,2,-3)^t$, $(-.0698,-1,-2)^t$, $(-.0349,3,-1)^t$, Gaussian blur of variance 5, zooming factor 2, compression ratio R=0.6, SNR of added noise 30dB (a) Original Shepp-Logan image, (b) Four simulated LR images., (c) Four CS observations, (d) Original Lena image, (e) Four simulated LR images, (f) Four CS observations. 26

2.3 1-level discrete wavelet transform. (a) Barbara image (b) DWT decomposition . 30

2.4 3-level discrete wavelet transform decomposition. 30

3.1 Sequential estimation process. Observations have been simulated using Gaussian Blur of variance 3, zooming factor P=2, Gaussian circulant Toeplitz measurement matrix with compression ratio R=0.8 and additive noise of SNR=40dB. (a) LR reconstructed observations, (b) initial estimate of HR image, PSNR=9.8 dB, (c) estimated HR image, PSNR=23.2 dB 35

3.2 Joint estimation process. Observations have been simulated using Gaussian Blur of variance 3, zooming factor P=2, Gaussian circulant Toeplitz measurement matrix with compression ratio R=0.8, and additive noise of SNR=40dB. (a) First iteration estimate with PSNR=22.8 dB, (b) last iteration estimate with PSNR=23.9 dB 37

3.3 Joint estimation process. Observations have been simulated using Gaussian Blur of variance 3, zooming factor P=2, Bernoulli circulant Toeplitz measurement matrix with compression ratio R=0.8 and additive noise of SNR=40dB. (a) First iteration estimate with PSNR=22.7 dB, (b) last iteration estimate with PSNR=23.9 dB 38

3.4 Joint estimation process with motion estimation . Observations have been simulated using Gaussian Blur of variance 3, zooming factor P=2, Bernoulli circulant Toeplitz measurement matrix with compression ratio R=0.8 and additive noise of SNR=40dB. (a) Estimated image using the minimization in Equation (3.16), (b) estimated image using minimization in Equation (3.17) 38

4.1 LR 3-level Haar wavelet coefficient decay, using simulated observations (SNR= 40 dB), (a,b) Cameraman image affected by Gaussian blur of variance 3 and 9, respectively. (c,d) Shepp-Logan image affected by blur of variance 3 and 9, respectively. 51

4.2 LR Cameraman image restoration using a simulated observation with blur variance 3, zooming factor P=1, R=0.8, noise SNR= 40 dB. (a) LR reconstructed observation using all elements of the coefficient vector $\mathbf{a}_q$ (PSNR=22.65 dB), (b) LR reconstructed observation using the first 60% of elements in $\mathbf{a}_q$ (PSNR=22.47 dB), (c) LR reconstructed observation using the first 20% of elements in $\mathbf{a}_q$ (PSNR=22.24 dB). Transform basis used is 3-level Haar wavelet transform. . . . 52

4.3 LR Shepp-Logan image restoration using a simulated observation with blur variance 3, zooming factor P=1, R=0.8, noise SNR=40dB. (a) LR reconstructed observation using all elements of the coefficient vector $\mathbf{a}_q$ (PSNR=21.35 dB), (b) LR reconstructed observation using the first 60% of elements in $\mathbf{a}_q$ (PSNR=21.18 dB), (c) LR reconstructed observation using the first 20% of elements in $\mathbf{a}_q$ (PSNR=20.68 dB). Transform basis used is 3-level Haar wavelet transform. . . . 53

4.4 Reconstruction of LR images. (a) Original HR Shepp-Logan image, (b,c) Down-sampled images Q=2, P=2, Blur Var=3, R=0.8, SNR=30 dB, (d,e) First estimates of the LR images, PSNR= 40.22 dB and , 40.16 dB respectively, (f,g) Final estimates of the LR images, PSNR=42.88 dB and 42.77 dB respectively. PSNR values were calculated with respect to the simulated LR images. 53

4.5 Reconstruction of LR images. (a) Cameraman original HR image, (b,c) Down-sampled images Q=2, P=2, Blur Var=3, R=0.8, SNR=30dB, (d,e) First estimates of the LR images, PSNR=35.52 dB and 35.29 dB, respectively, (f,g) Final estimates of the LR images, PSNR=35.55 dB and 35.34 dB, respectively. PSNR values were calculated with respect to the simulated LR images. 54

4.6 Reconstruction of LR images. (a) Lena original HR image, (b,c) Down-sampled images Q=2, P=2, Blur Var=3, R=0.8, SNR=30dB, (d,e) First estimates of the LR images, PSNR=40.22 dB and 40.16 dB, respectively, (f,g) Final estimates of the LR images, PSNR=42.88 dB and 42.77 dB, respectively. PSNR values were calculated with respect to the simulated LR images. 55

4.7 Absolute error comparison of the four registration approaches. R=0.8, Q=4, blur var=3, SNR=40dB. on (a) P=2, (b) P=4. 58

4.8 Proposed CSSR vs CS ID algorithms comparison (Blur Var=5, SNR=30dB, for CSSR P=1, Q=1). (a) Cameraman (b) Lena (c) Shepp-Logan. 63

4.9 Proposed CSSR vs CS ID algorithms comparison (Blur Var=3, SNR=40dB, for CSSR P=1, Q=1). (a) Cameraman, (b) Lena, (c) Shepp-Logan. 64

4.10 Proposed CSSR vs CS ID algorithms comparison (R=0.6, SNR=30dB, for CSSR P=1, Q=1). (a) Cameraman, (b) Lena, (c) Shepp-Logan. 65

4.11 Proposed CSSR vs CS ID algorithms comparison (R=0.8, SNR=40dB, for CSSR P=1, Q=1). (a) Cameraman, (b) Lena, (c) Shepp-Logan. 66

4.12 Comparison between SR algorithms and the CSSR algorithm. P=4, SNR=40dB, Q=4, and for CSSR, R=1.0. (a) Cameraman image, (b) Lena, (c) Shepp-Logan image. 69

4.13 Comparison between SR algorithms and the CSSR algorithm. P=4, SNR=30dB, Q=4, and for CSSR, R=1.0. (a) Cameraman image, (b) Lena, (c) Shepp-Logan image. 70

4.14 Original Images. (a) Satellite, (b) Barbara, (c) Peppers, (d) Alhambra. 71

4.15 Performance of the CSSR algorithm (Q=4). Case 1: P=2, Blur Var=3, SNR=40 dB, Case 2: P=2, Blur Var=5, SNR=30 dB, Case 3: P=4, Blur Var=3, SNR=40 dB, Case 4: P=4, Blur Var=5, SNR=30 dB. (a) Satellite image, (b) Barbara image. . . 75

4.16 Performance of the CSSR algorithm (Q=4). Case 1: P=2, Blur Var=3, SNR=40 dB, Case 2: P=2, Blur Var=5, SNR=30 dB, Case 3: P=4, Blur Var=3, SNR=40 dB, Case 4: P=4, Blur Var=5, SNR=30 dB. (a) Peppers image, (b) Alhambra image . . 76

4.17 Estimated Satellite Images using the proposed CSSR method (R=0.8 and Q=5). (a) P=2, Blur Var=3, (b) P=2, Blur Var=5, (c) P=4, Blur Var=3, (d) P=4, Blur Var=5. 79

4.18 Estimated Barbara Images using the proposed CSSR method (R=0.8 and Q=5). (a) P=2, Blur Var=3, (b) P=2, Blur Var=5, (c) P=4, Blur Var=3, (d) P=4, Blur Var=5. 80

4.19 Estimated Peppers Images using the proposed CSSR method (R=0.8 and Q=5). (a) P=2, Blur Var=3, (b) P=2, Blur Var=5, (c) P=4, Blur Var=3, (d) P=4, Blur Var=5. 81

4.20 Estimated Alhambra Images using the proposed CSSR method (R=0.8 and Q=5). (a) P=2, Blur Var=3, (b) P=2, Blur Var=5, (c) P=4, Blur Var=3, (d) P=4, Blur Var=5. 82

4.21 CSSR performance for multiple and single input images. (P=4, Blur Var=3, SNR=40 dB. on (a) Satellite, (b) Barbara. 83

4.22 CSSR performance for multiple and single input images. (P=4, Blur Var=3, SNR=40 dB. on (a) Peppers, (b) Alhambra. 84

4.23 Comparison of the proposed CSSR vs the sequential approach for the Satellite image, (Q=4, P=4), using (a) Blur Var=5, SNR=30 dB, (b) Blur Var=3, SNR=40 dB. 86

4.24 Comparison of the proposed CSSR vs the sequential approach for the Barbara image, (Q=4, P=4), using (a) Blur Var=5, SNR=30 dB, (b) Blur Var=3, SNR=40 dB. 87

4.25 Comparison of the proposed CSSR1 vs CSSR2 for the Satellite image, (Q=4, P=4), using (a) Blur Var=5, SNR=30 dB, (b) Blur Var=3, SNR=40 dB. 90

4.26 Comparison of the proposed CSSR1 vs CSSR2 algorithms for the Barbara image, (Q=4, P=4), using (a) Blur Var=5, SNR=30 dB, (b) Blur Var=3, SNR=40 dB. . . . 91

4.27 PMMW image of a man free of threats (Q=4, R=1, P=2).(a) Four noisy real observations, (b) Bilinear interpolation from one reconstructed LR image, (c) Estimated image using CSSR algorithm. 93

4.28 PMMW image of a man free of threats (Q=4, R=0.8, P=2) (a) Four noisy real observations, (b) Bilinear interpolation from one reconstructed LR image, (c) Estimated image using CSSR algorithm. 94

4.29 PMMW image of a man with a threat attached to his arm (Q=4, R=0.8). (a) LR images, (b) Bilinear interpolation from one reconstructed image, P=2, (c) Estimated HR image using the CSSR algorithm, P=2, (d) Bilinear interpolation from one reconstructed image, P=4, (e) Estimated HR image using the CSSR algorithm, P=4. 95

4.30 PMMW image of a man with a threat attached to his chest (Q=7, R=0.8, P=2). (a) LR images, (b) Bilinear interpolation from one reconstructed LR image, (c) Estimated HR image using the CSSR algorithm. 96

4.31 Original Images (a) Barbara, (b) Lena, and (c) Peppers. (d) Simulated LR Barbara image ($\mathbf{s} = [.1222, -2, 3]^t$, blur variance 7, P=2), (e) simulated CS observation (R=0.5, SNR=40 dB). The black line represents the added zero-valued entries to illustrate a square image. 98

4.32 Comparison between CS algorithms and the CCSSR algorithm for the Lena image. For CCSSR, P=1, Q=3. 99

4.33 Performance of the proposed CCSSR vs R. Blur Var=5, SNR=40dB, Q=3. (a) P=2, (b) P=4. 100

4.34 Reconstructed Peppers Images using the CCSSR algorithm. R=0.6, Blur Var=5, SNR=40dB, and Q=3. (a) P=2, (b) P=4, ... 101

4.35 Image super resolution from real observations, R=0.8, P=2. (a) First 4 LR images (b) Bilinear interpolation of one reconstructed LR image, (c) Estimated HR image using the CCSSR algorithm, with Q=4, (d) Estimated HR image using the CCSSR algorithm, with Q=16. 101

4.36 Image super resolution from real observations, R=0.8, P=2. (a) First 4 LR images (b) Bilinear interpolation of one reconstructed LR image, (c) Estimated HR image using the CCSSR algorithm, with Q=4, (d) Estimated HR image using the CCSSR algorithm, with Q=16. 102

List of Tables

4.1 Registration parameter estimation at the HR level for the Shepp-Logan image, Q=4, Blur var=3, SNR=40dB, R=0.8. (a) using App1, (b) using App2 56

4.2 Registration parameter estimation at the LR level for the Shepp-Logan image, Q=4, Blur var=3, SNR=40dB, R=0.8. (a) using App3 (b) using App4 57

4.3 Performance comparison of state-of-the-art CS ID algorithms with proposed CSSR algorithm for the Cameraman image. For CSSR P=1 and Q=1. In bold blue are the highest PSNR values. 60

4.4 Performance comparison of state-of-the-art CS ID algorithms with proposed CSSR algorithm for the Lena image. For CSSR P=1 and Q=1. In bold blue are the highest PSNR values. 61

4.5 Performance comparison of state-of-the-art CS ID algorithms with proposed CSSR algorithm for the Shepp-Logan image. For CSSR P=1 and Q=1. In bold blue are the highest PSNR values. 62

4.6 Comparison of state-of-the-art SR algorithms with the CSSR algorithm for Cameraman and Lena images, with Q=4 and for CSSR R=1.0. In bold blue are the highest PSNR values. 67

4.7 Comparison of state-of-the-art SR algorithms with the CSSR algorithm for Shepp-Logan image, with Q=4 and for CSSR R=1.0. In bold blue are the highest PSNR values. 68

4.8 Performance of the CSSR algorithm for the Satellite and Barbara images, using $Q = 4$. 72

4.9 Performance of the CSSR algorithm for the Peppers and Alhambra images, using $Q = 4$. 73

4.10 Performance of the CSSR algorithm for the Satellite and Brabara images, using a single observation ($Q = 1$). 77

4.11 Performance of the CSSR algorithm for the Peppers and Alhambra images, using a single observation ($Q = 1$). 78

4.12 Performance of the sequential approach using $Q = 4$. 85

4.13 Comparison of CSSR1 vs CSSR2 algorithms for the Satellite image, using $Q = 4$. 88

4.14 Comparison of CSSR1 and CSSR2 algorithms for the Barbara image, using $Q = 4$. 89

4.15 Comparison of CS algorithms with the proposed CCSSR algorithm for CCSSR P=1.0, Q=3. In bold blue are the highest PSNR values. 97

4.16 CCSSR algorithm vs R (blur var 5, SNR=40dB, and Q=3). 99

Resumen y Conclusiones

Resumen

El Sensado Comprimido (SC) es una nueva tecnología que permite la captación de imágenes directamente comprimidas, con la consiguiente reducción del tiempo de adquisición y de la cantidad de memoria necesaria para almacenarlas, procesarlas y trasmitirlas. La teoría de SC establece que una imagen o señal que admita una representación rala se puede reconstruir a partir de un conjunto muy incompleto de medidas o proyecciones de la imagen. La Superresolución (SR) es una técnica de procesamiento de imágenes muy poderosa que permite reconstruir una o más imágenes de Alta Resolución (AR) a partir de varias imágenes de Baja Resolución (BR). La obtención de imágenes de AR de buena calidad mediante la aplicación de técnicas de SR requiere la aplicación de un buen proceso de registro de las imágenes observadas. La SR permite superar las limitaciones hardware, ópticas y espaciales de los dispositivos de captación de imágenes para obtener imágenes de buena calidad.

En la presente tesis doctoral proponemos un nuevo marco de estudio para la obtención de imágenes de AR a partir de varias imágenes de BR de la misma escena adquiridas mediante sistemas de SC. La hiptesis de que cuando una imagen admite una representacin rala en un dominio transformado, una versin borrosa de la misma tambin admitir una representacin rala en el dominio transformado, nos permite recuperar imgenes borrosas a partir de observaciones de SC. Por analogía, también se puede asumir que a una imagen de BR desplazada, borrosa y submuestreada se le puedan aplicar técnicas de SC. El nuevo marco de estudio de Superresolución de Sensado Comprimido (SRSC) propuesto en esta tesis combina la aplicación de algoritmos de reconstrucción de SC previamente existentes con una nueva técnica de SR basada en la aplicación de una regularización robusta que favorece la raleza de las imágenes, basada en un modelo a priori Bayesiano superGausiano.

El problema SRSC tiene muchas incógnitas, principalmente la imagen de AR, los coeficientes de la representación en el dominio trasformado de cada imagen de BR, y los vectores de desplazamientos. Estas incógnitas se pueden estimar de forma secuencial o simultáneamente. El método propuesto en esta tesis aplica una estrategia de estimación conjunta en la que las reconstrucciones de las imágenes de BR y la estimación de la imagen de AR se llevan a cabo simultáneamente de forma alternativa, e incluye una estimación automática de los vectores de desplazamientos. En este trabajo se estudian las ventajas de la estimación conjunta respecto a la estrategia secuencial. En la tesis se estudia también lo que aporta la utilización de varias imágenes de BR en lugar de una sola.

El enfoque del SRSC trasforma el problema de estimación conjunta con restricciones en

una secuencia de subproblemas no restringidos, mediante la aplicación del Método de los Multiplicadores en Direcciones Alternativas (MMDA). El subproblema de estimación de la imagen de AR se resuelve aplicando la técnica de mayorización-minimizazión. Para la estimación de los parámetros de registro de las imágenes se proponen cuatro estrategias diferentes, que son comparadas en este trabajo. El subproblema de la reconstrucción de SC se plantea como minimización de la norma $\ell 1$ sujeto a una restricción cuadrática.

El método propuesto se ha probado para imágenes naturales reales en escala de grises cuyas observaciones SC han sido simuladas y sintetizadas utilizando una matriz de medición que es posible elaborar prácticamente. Se han realizado comparaciones del método propuesto con algoritmos del estado del arte en SR que no aplican SC y también con algoritmos del estado del arte en deconvolución de imágenes de SC. Estas comparaciones han resultado favorables al método SRSC propuesto. También se han obtenido excelentes resultados en experimentos en los que intervenían tanto el SC como la SR, aunque éstos no se han podido comparar con otros métodos, porque no hay trabajos publicados, aparte de los nuestros, que estudien este problema al completo.

Una de las posibles e importantes aplicaciones del SRSC es el de las Imágenes Milimétricas Pasivas (IMMP), muy útiles en problemas de detección de amenazas ocultas. Los experimentos realizados con SRCS sobre IMMP reales con observaciones SC sintéticas han mostrado que es posible aplicar el marco de estudio propuesto para obtener imágenes de SR de alta calidad a partir de varias imágenes de BR adquiridas mediante SC, lo que se espera pueda facilitar los procesos de detección de amenazas ocultas.

Se ha extendido el SRSC para abordar también el problema de Superresolución de Sensado Comprimido de imágenes en Color (SRSCC), para el que también se ha propuesto un algoritmo que es otra de las aplicaciones de este trabajo. El SRSCC permite obtener imágenes en color de SR a partir de varias imágenes reales en color obtenidas mediante SC. El SRSCC se aplica a observaciones SC independientes de los canales rojo, verde y azul (RVA) de la imagen obtenidas utilizando una matriz de medición que es posible elaborar prácticamente. En el SRSCC la estimación de los parámetros de registro se realiza conjuntamente para los tres canales. En este trabajo se incluyen comparaciones entre los resultados del algoritmo SRSCC propuesto y los obtenidos aplicando otras técnicas de reconstrucción de SC de imágenes en color.

Conclusiones

En esta tesis doctoral hemos propuesto un nuevo marco de estudio para la SR de imágenes a partir de varias imágenes sin registrar de BR adquiridas mediante técnicas de SC. Cualquier técnica clásica de SR y/o de SC podría integrarse en la metodología desarrollada. En este trabajo se ha propuesto un modelo de degradación para este novedoso problema combinado y también un enfoque para el SRSC. Este trabajo ha sido el primero en tratar el problema propuesto y podría resultar muy útil para el campo del procesamiento de imágenes.

El método SRSC permite disminuir la frecuencia de muestreo, la velocidad de trasmisión y el ancho de banda requeridos para la transmisión de imágenes, así como los requerimientos de memoria del almacenamiento y proceso de las mismas. También permite un menor tiempo de adquisición de las imágenes, de mucho interés en aplicaciones médicas y de procesamiento de IMMP. La mejor calidad de las imágenes de SR facilita el reconocimiento de patrones y la diagnosis médica y permite realzar zonas específicas de las imágenes de videovigilancia o de satélite.

El método de reconstrucción propuesto utiliza una nueva regularización robusta que favorece la raleza de las imágenes de AR obtenidas resolviendo una ecuación lineal en $\mathbf{x}$ (la imagen de AR) mediante la aplicación del método del gradiente conjugado. El vector de coeficientes de la representación en el dominio trasformado de las imágeness de BR se estima minimizando la norma $\ell 1$ sujeta a una restricción cuadrática. Se pueden aplicar cuatro procedimientos diferentes de estimación de los paráetros de registro que permiten determinarlos con precisión; esto es muy importante porque existe una dependencia crítica entre la calidad de las imágenes de SR y la eficacia del proceso de registro. El registro puede realizarse con respecto a la imagen de AR o entre las imágenes de BR, lo que resulta en una menor dependencia respecto a los valores iniciales utilizados.

Summary and Conclusions

Summary

Compressed Sensing (CS) is a new technology that simultaneously acquires and compresses images reducing acquisition time and memory requirements to process or transmit them. It establishes that a sparsely representable image/signal can be recovered from a highly incomplete set of measurements or projections of the image. Image Super Resolution (SR) is an important post-processing technique where multiple input images are super resolved to obtain one or more images of higher resolution and better quality. SR necessitates a good image registration procedure in order to obtain a High Resolution (HR) image of enhanced quality. Such quality should overcome image degradation due to system hardware, optical and spatial limitations.

In this dissertation we propose a novel framework to obtain HR images from CS imaging systems capturing multiple Low Resolution (LR) images of the same scene. The assumption that when an image admits a sparse representation in a transformed domain, a blurred version of it will also be sparse in the transformed domain allows us to recover blurred images from CS observations Similarly, a warped, blurred, and down-sampled LR image is expected to be also sparse in a transformed domain and hence can be reconstructed from the corresponding CS observation. The proposed Compressed Sensing Super Resolution (CSSR) approach, combines existing CS reconstruction algorithms with an LR to HR approach based on the use of a new robust sparsity promoting prior based on super Gaussian regularization.

The CSSR problem has multiple unknowns, mainly the HR image, the transformed coefficients corresponding to each LR image, and the motion vectors. The unknowns can be estimated sequentially or simultaneously. The method we propose in this dissertation is a joint estimation framework where LR reconstructions and HR estimation are carried out simultaneously by alternating between them including the automatic estimation of registration parameters. The advantages of the joint estimation over the sequential approach are discussed in this work. The advantage of utilizing multiple input images over a single one is also discussed in this dissertation.

The CSSR approach converts the constrained joint optimization problem into a sequence of unconstrained sub-problems using Alternate Direction Method of Multipliers (ADMM). The HR image estimation sub-problem is solved using majorization-minimization. The registration parameters are estimated using four different approaches, which are compared in this work. The CS reconstruction sub-problem becomes an ℓ_1 minimization subject to a quadratic constraint.

Our proposed framework has been tested on gray scale simulated and synthetically compressed real natural images, which were compressed using a measurement matrix that can be synthesized practically. This is compared with state-of-the-art SR algorithms which do not use CS in their work, and with state-of-the-art image deconvolution algorithms from CS images, which do not use down-sampling in their work. The proposed CSSR performs favorably compared to them. Moreover, the proposed CSSR has been tested when both compression and down-sampling are present. In this case, no comparison with other methods is provided since this is the first time both problems are approached jointly.

One important CSSR application is Passive Millimeter Wave (PMMW) images which are used for threat detection. The performed CSSR experiments on synthetically compressed real millimeter wave images, demonstrate the capability of the proposed framework to provide very good quality super resolved images from multiple low resolution compressed acquisitions, which is expected to improve threat detection rates.

CSSR can be extended to the proposed Color Compressed Sensing Super Resolution (CCSSR) algorithm, which constitutes another application of this work. In the CCSSR the SR image is estimated from true color CS observations. While the red, green, blue (RGB) channels are sensed separately using a measurement matrix that can be synthesized practically, the registration parameters are jointly estimated from the three channels simultaneously. This work compares the proposed CCSSR algorithm with other color CS reconstruction techniques.

Conclusions

In this dissertation we have proposed a novel framework to reconstruct SR images from multiple unregistered LR images acquired using CS techniques. Any classical SR and/or CS techniques can be incorporated in the developed methodology. The degradation model of this novel combined problem has been modeled and a CSSR approach has been proposed in this work.

The CSSR method lowers the sampling frequency, transmission rates, and the bandwidth of the image signal, and memory requirements to store and/or send the image. Moreover, the acquisition time can be lowered, which is very important in medical and PMMW imaging applications. The enhanced SR image quality is advantageous in pattern recognition, medical diagnostics, and to emphasize a specific area of an image in surveillance cameras and satellite applications.

The proposed HR reconstruction uses a new robust sparsity promoting prior and solves a linear equation in $\mathbf{x}$ (the HR image), using conjugate gradient method. The transformed coefficient vector estimation is an ℓ_1 norm subject to a quadratic term optimization problem. The registration parameters can be estimated using four different procedures, to finally obtain accurate results, since any SR estimation process is highly dependent on the performance of the registration estimation step. The parameters can be estimated from the estimated HR image, or the LR images themselves, with the estimation from reconstructed LR images being less sensitive to the initial conditions. Furthermore we found that the estimation at LR level results in better quality of the reconstructed image.

The proposed optimization framework uses ADMM to jointly estimate all the unknowns including HR image, LR images, and registration parameters. We have experimentally shown that this simultaneous reconstruction outperforms the sequential method, that first performs LR reconstruction to then obtain an HR image from a set of LR observations. The sequential ap-

proach estimates every unknown just once, while the alternate approach iteratively updates the estimated unknowns. The better performance of the alternate approach is due to the additional information provided during the estimation process.

We also showed experimentally the enhancement obtained due to the multiple input images when compared with a single one. This is expected due to the additional information every input image provides. However, the multiplicity necessitates accurate registration estimation procedure which inherently affects the overall process.

The proposed framework has been tested and compared, at a unity compression ratio, with state-of-the-art SR algorithms which do not use compression in their work. It has been also compared, at a unity zooming factor, with state-of-the-art ID algorithms that deblur CS images, which do not use down-sampling in their work. Both comparisons used synthetic images and showed better performance of the proposed CSSR over others. The performance of CSSR when using practical values of P and R has also been tested and analyzed.

Besides, the CSSR effectiveness has been demonstrated experimentally on synthetically CS noisy real images. This represents the practical application of the CSSR method, which showed very good results. The proposed framework can be extended to CS video for the estimation of both intra-frame and inter-frame SR.

The proposed CSSR method has been tested on PMMW images. These images usually have poor qualities and limited resolution, which makes super resolving them a challenging task and is a hard test of the CSSR approach. The CSSR could be used to improve the quality of PMMW images. This is expected to improve threat detection rates, which is an expected field of future research. Notice here that the nature of PMMW is similar to astronomical images and medical images, and the good performance of the proposed CSSR algorithm can be extended to these images.

The proposed approach can also be applied to true color CS images. The separately sensed channels are utilized in a joint registration estimation to effectively and accurately estimate registration parameters for the three channels. The obtained results present an excellent image quality, even better than the obtained using previous CS reconstruction methods which correlate the color channels. The efficient optimization process can be extended in future works to deal with mosaic color images.

Chapter 1

Introduction

This work is devoted to estimate High Resolution (HR) images from multiple Low Resolution (LR) observations acquired using Compressed Sensing (CS) techniques. We propose a framework that combines Super Resolution (SR) reconstruction with CS acquisition.

CS imaging lowers the sampling frequency beyond that required by the Nyquist-Shannon theorem, and hence lowers transmission rate and bandwidth requirements. The smaller data size obtained during the acquisition process lowers the memory requirements to save or transmit. Another important benefit CS offers is the lower acquisition time, due to the smaller data size, which is vital in applications like medical imaging and millimeter wave images.

Furthermore, SR offers a higher pixel density and overcomes the limited resolution imaging. The higher resolution enhances the image quality by showing more details of the original scene. Resolution enhancement is needed in computer vision applications like pattern recognition and analysis of images, in medical imaging for diagnosis, and in applications that require specific areas of the image to be zoomed, like surveillance cameras, satellite applications, and threat detection devices. Moreover, SR promises a better use of high performance screens, like High Definition Liquid Crystal Displays (HD LCDs).

In the framework proposed in this dissertation, classical SR methods are combined with existing CS methods. The experimental results to be presented will prove the applicability of this framework, and the good quality of the output images.

This chapter introduces basic background to this dissertation, then presents its motivations, hypothesis, and objectives. This is followed by stating the research methodology and main contributions of this work. Finally, the thesis outline is presented.

1.1 Background

Independently of how well designed an imaging system is, its performance comes to a certain limit. Limitations on image spatial resolution lead to the use of SR techniques to improve the pictorial perception of the human eye and/or automatic machines. After a certain limit, an imaging system suffers from many hardware problems, such as limited pixel density, lens point spread function and aberration effects. Other problems may accompany the acquisition process, such as blurring due to motion of the camera or objects in the scene. The acquired images can be considered as decimated LR versions of the original scene. These LR images can be used to estimate an HR image using SR techniques.

SR techniques are post-processing techniques, they use multiple LR images as input images to estimate one, or more, HR output image(s). The process increases the spatial resolution, removes degradations in the input images, and increases the high frequency content of the scene image.

Traditionally, all pixel values of the LR image have to be acquired. However, this information can be successfully recovered from only a small number of linear projections utilizing CS techniques. This dissertation studies how to estimate SR images from CS observations.

1.1.1 Classical Digital Imaging

A digital image is a discrete representation of both spatial coordinates and intensity information in a scene. The spatial information is determined by an array of sensors or pixels at fixed positions of the image plane of the camera. Every pixel receives a different optical intensity. Hence, each sensor integrates the image locally to form the whole representation with other sensors. An imaging sensor can be a Charge-Coupled Device (CCD) or a Complementary Metal-Oxide-Semiconductor (CMOS) active-pixel sensor.

An image can be represented mathematically using a two-dimensional (2D) array. The coordinates represent the spatial information and the intensity is represented by the value at the corresponding coordinates.

Figure 1.1(a) shows a 14×12 gray scale image for the letter 'a'. The image layout was exaggerated in Figure 1.1(b) to show every pixel in the image, with the horizontal and vertical coordinates of all pixels representing the image. The value at a pixel represents the intensity, scaled to the range [0,1], sensed by the corresponding sensor at the same location, shown in Figure 1.1(c). The highest value represents the White color, and the lowest represents the Black color. In summary, the image shown in Figure 1.1(a) can be represented by the $2D$ matrix shown in Figure 1.1(c).

The pixel density of a camera, measured in pixels per unit area, determines its spatial resolution. Given a CCD or CMOS size, we would like to use the largest possible number of sensors. However, aside from hardware cost, decreasing the sensor size results in a lower incident light and hence increases the shot-noise. The increased number of pixels also decreases the camera speed [2]. This forms the first limitation on the spatial resolution of imaging systems.

The camera lens also adds optical limitations on the image details, and some high-frequency components may be lost due to the point spread function of the lens, aberration effects and aperture diffraction (see [3]). Camera or object motion in the scene may affect negatively the

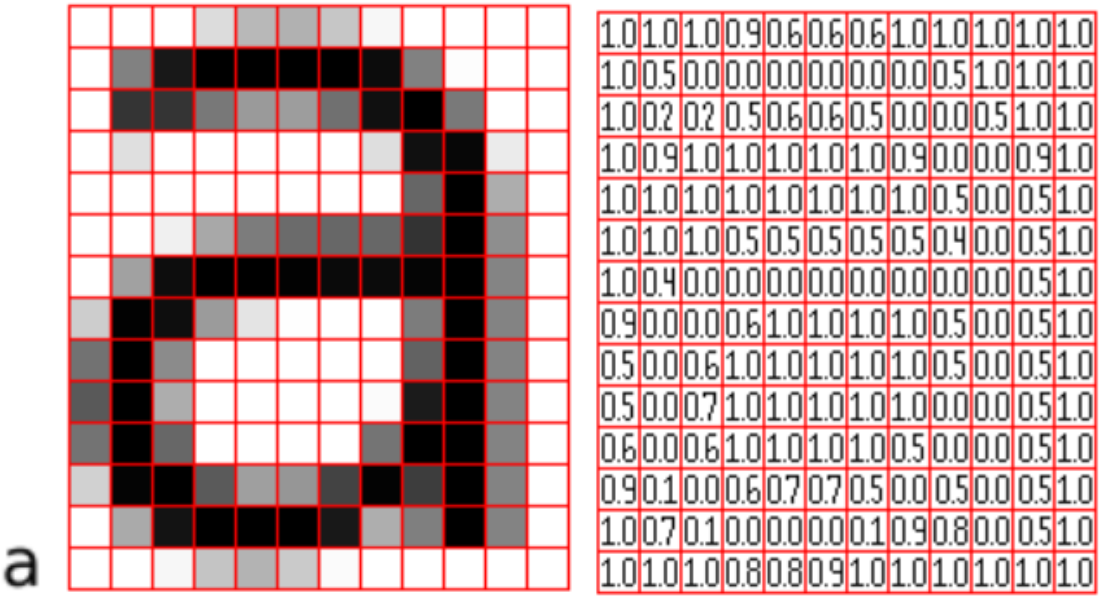

Figure 1.1: Image representation: (a) gray scale image for the letter 'a', (b) exaggerated version of the image (×16), (c) the corresponding pixel values.

imaging process.

Particular applications may add some additional limitations, such as portability in surveillance cameras, cell phone built-in cameras, and satellite imaging, among others. Furthermore, notice also that the resolution is limited by the camera speed, memory size, and physical constraints.

On the other hand, as stated by the Nyquist Shannon sampling theorem, high spatial resolution of an image necessitates high sampling frequencies for a better acquisition and processing. This requires a high bandwidth, or bit rate to send or process the image. The solution for such a challenge could be compression techniques that seek for a compact representation of acquired images. Many compression techniques have been utilized to better represent an image. Transform coding, for example, makes use of sparsity and compressibility of an image.

For a given image quality, the higher the difference between the rate after compressing the image, and the nominal bandwidth of the original version the better compression technique is. Based on this, many standards such as JPEG, JPEG2000, MPEG, and MP3 are used.

1.1.2 Color Images

In gray scale images, there is only one intensity value for each pixel, while color images need more intensity values, or channels, to be represented as is the case in Red-Green-Blue (RGB) representation, which uses three channels, one per color. Figure 1.2 shows how the RGB channels look like.

RGB representation is inherently difficult for humans to work with and it is not related to the natural way the human eye perceive colors, see [1]. An alternative representation is the YCbCr color space. Y is the luminance, Cb chroma is the blue difference, and Cr chroma is the red difference. The nominal values of chroma range from -0.5 to 0.5 when Y is normalized to the range [0,1]. Figure 1.3 shows how the three channels look like. YCbCr is a practical approximation to color processing and perceptual uniformity and is used in standard definition television.

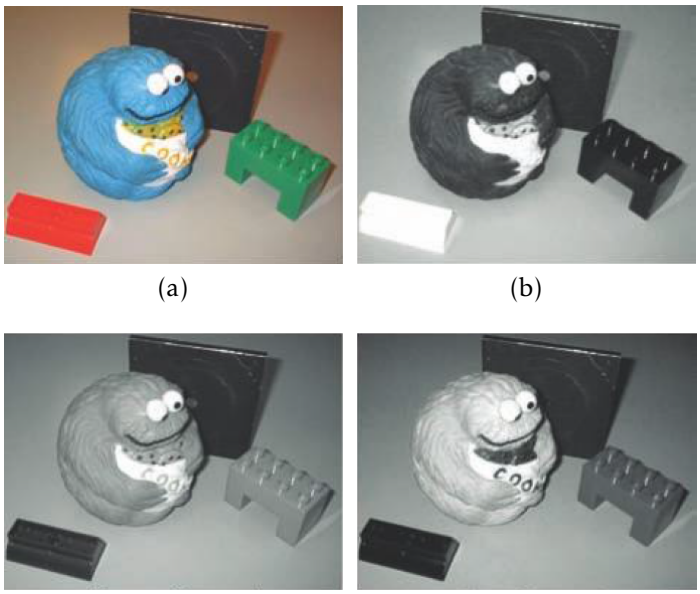

(a) (b)

(c) (d)

Figure 1.2: RGB color Image. (a) Original RGB image, (b) Red channel, (c) Green channel, (d) Blue channel. (Adapted from [1]).

A color image is represented by a 3 dimensional matrix. If the gray scale image uses an $x \times y$ matrix, then the corresponding color image utilizes an $x \times y \times 3$ matrix. In Chapter 4 we discuss the ability to extend SR from CS observations to color images, as an application of the proposed CSSR framework.

1.1.3 Millimeter Wave Images

Electromagnetic wave (EM) spectrum extends from Extra Low Frequency (ELF) signals, with frequencies of few Hertz (Hz), to Gamma rays, with frequencies in powers of 10^{18} Hz (exa Hertz, EHz). The wavelength of a signal is inversely proportional to its frequency and extends from 10^{8}m for ELF to 10^{-12}m for Gamma rays. The EM wave spectrum is shown in Figure 1.4, with the borders between bands being not strict and may vary slightly from one reference to another.

Of special interest in the EM wave spectrum is the visible light spectrum which extends from 400THz, at the border of the red color, to 789THz, at the border of the violet color. This range defines the various colors the human eye can distinguish. The wavelet range for this

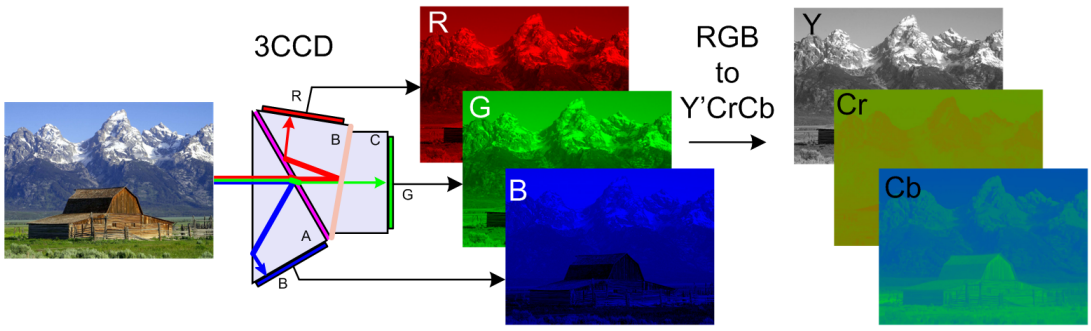

Figure 1.3: YCbCr colored image.

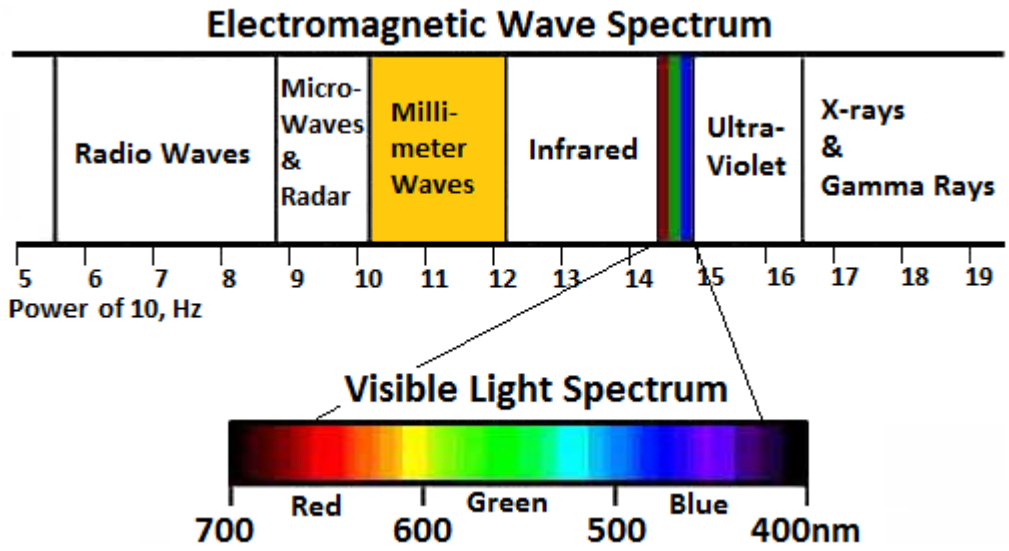

Figure 1.4: Electromagnetic wave spectrum

spectrum is from 620nm to 450nm. Images acquired using the radiations in this band are usually called natural images and can be recognized by the human eye.

Another important frequency band is the Millimeter (MM) wave spectrum. MM waves are those signals of wavelengths in millimeters, from 1mm to 10mm. This lies in the Extremely High Frequency (EHF) range that extends from 30GHz to 300GHz, although not all this range has been used practically in millimeter wave imaging.

The main advantage of MM waves is its penetrability through a variety of materials like clouds, fog, smoke, sandstorms, and even through clothes. This enables a good performance in low-visibility conditions. Also, it serves in day and night conditions [4].

An MMW imager, or scanner, can be of two types: Active and Passive. Active imagers use a MMW source to illuminate the scene. Passive imagers do not use any artificial MMW source,

instead they work with MMW radiation that occurs naturally in the scene. In the experimental part of the dissertation, we use Passive Millimeter Wave (PMMW) images. An example of the PMMW imager is the system shown in Figure 1.5, which is widely used at airports for threat detection.

Figure 1.5: PMMW threat detect system.

Both types of imagers form images through the detection of MMW radiation from a scene. The detected radiation relies on the idea that objects reflect and emit MMW radiation differently depending on the emissivity of the object, which is a function of the nature of the object itself. A perfect absorber object has a unity emissivity, while a perfect non absorber (reflector) has zero emissivity. Depending on variations in emissivities of various scene materials, which differ from an object to another, the power will be differently radiated from various objects in the image. The radiated powers in the scene are detected by the MMW detector, then translated, in a way, to different brightness levels of the image. Figure 1.6 shows a typical PMMW image of a man.

MMW imaging has many advantages like high sensitivity to metal objects, and it is suggested in applications requiring near-all-weather operations since the changes in performance due to weather variations are minimal. Many applications like aircraft landing and guidance, low-visibility navigation, situational awareness, and concealed threat detection, to name a few benefit from MMW imaging.

1.1.4 Super Resolution

As we have already indicated, both hardware limitations, such as sensor size, camera speed, cost, and optical limitations such as blurring action, etc. make it necessary to explore alternative ways to enhance the resolution of an image.

(a)

Figure 1.6: Sample PMMW image of a man.

Instead of decreasing the effects of these limitations by working on the camera itself, resolution enhancement or SR techniques processes the images acquired under these limitations and try to reconstruct one or more HR image(s). This post-processing step utilizes multiple input LR images of the same scene to estimate images of higher spatial resolution, with less degradation effects, and better quality. The estimated image should not only provide a better visualization (visual quality issue), but also extracts additional information details from the input images (recognition issue).

The multiple input images can be acquired successively by the same camera, or by multiple cameras imaging the scene simultaneously. In both cases, it is expected to result in some shifts between the various acquired images. The shifts may be due to a small camera movement with respect to the scene, for example. These subpixel shifts or displacements give the added information that enables to efficiently estimate the HR image. Figure 1.7 shows an illustration

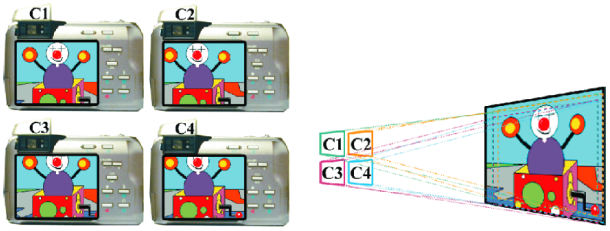

Figure 1.7: Illustartion of SR process

of the SR process. The acquired images can be considered down-sampled, blurred, and warped versions of the original HR image. Assume that we have the LR image sequence $\{\mathbf{y}_q\}$ where $q \in \{1, \cdots, Q\}$. Each $\mathbf{y}_q$ is represented by a $D \times 1$ vector. The obsevation process of the LR image sequence can be modelized as follows,

$$\mathbf{y}_q = \mathbf{A}\mathbf{H}_q\mathbf{C}(\mathbf{s}_q)\mathbf{x} + \mathbf{n}_q = \mathbf{B}_q(\mathbf{s}_q)\mathbf{x} + \mathbf{n}_q, \text{ for } q = 1, \ldots, Q, \tag{1.1}$$

where $\mathbf{A}$ is a $D \times N$ down-sampling matrix, $\mathbf{H}_q$ is an $N \times N$ blurring matrix, $\mathbf{C}(\mathbf{s}_q)$ is the $N \times N$ warping matrix corresponding to a 3×1 motion vector $\mathbf{s}_q$, $\mathbf{x}$ is the $N \times 1$ HR image vector, and $\mathbf{n}_q$

is a $D \times 1$ vector representing the noise assumed to be additive. Elements of the motion vector $\mathbf{s}_q = [\theta, c, d]^t$ correspond respectively to rotation angle, horizontal and vertical displacements. $\mathbf{B}_q(\mathbf{s}_q)$ is a $D \times N$ matrix modeling the acquisition system. The zooming factor is defined to be $P \geq 1$ and represented by the factor of increase in each dimension of the image, hence the factor of increase in resolution is $P^2 = N/D$. Figure 1.8 shows an example of application of the four degradation steps of this acquisition model to the Cameraman image.

(a) (b)

(c) (d) (e)

Figure 1.8: Degradation process illustrative example. (a) 256×256 Original Cameraman image, (b) Warped image, $\theta = -0.1047rad$, $c = 3$, $d = 2$, (c) Blurred image, Gaussian blur with variance 3, (d) 64×64 Down-sampled image, P=4, (e) Noised image, white Gaussian noise SNR=40dB

Warping, in out context, is the displacement affecting the acquired images with respect to the reference image or the original image. This displacement can be horizontal or vertical when all the objects in a scene are shifted in the $x-, y-$ direction by the same distance c, d respectively. It may also be rotational, when the observation is a rotated version of the reference image, by a rotational angle θ. The three parameters (θ, c, d) form the motion vector of the observation. An example of a warped image is shown in Figure 1.8(b), where the motion vector used was $[-0.1047, 3, 2]^t$, θ is in radians, and the last two entries are the number of pixel shifts in the horizontal and vertical directions respectively.

A blurred image may be the result of many factors affecting the imaging system, like mo-

tion blur and out-of-focus blur, among others. An object moving within a scene or the motion of the camera itself may result in motion blur. Out-of-focus blur depends on many parameters like focal length, camera aperture size and shape, distance between the camera and the observed scene, wavelength of the incoming radiation, and the effects due to diffraction (see [5]). However, in our work, we are not interested in the type of blur or the phenomena affecting it. Instead, we include an approximation that models its effect on the observed image. In Figure 1.8(c) a Gaussian blur, with variance 3, has been added to the warped image.

Down-sampling, or decimation, is the process of reducing the sampling rate of an image signal. Let us describe the down-sampling of the image shown in Figure 1.8(c), to obtain the image in Figure 1.8(d). In the two dimensional representation of the Figure 1.8(c) image, divide the 256×256 matrix into square blocks, each of $P \times P$ size. Then from the P^2 pixels in each block, keep the first pixel (or the mean) and discard all the others. The down-sampled image is represented only by the pixels kept, and each dimension of the original image will be P times that of the decimated version. In vector form, the length of the resulting image will be N/P^2. In Figure 1.8(d), the zooming factor in each dimension is $P = 4$, hence the block size is 4×4. The pixels kept form the 64×64 down-sampled image shown in Figure 1.8(d). Notice that the factor of increase in resolution is $P^2 = 16$.

SR reconstruction collects information from various LR images to estimate one HR image. Figure 1.9 illustrates the process, for a zooming factor P=2, and shows how the information from each image is shared in the estimation process of the HR image pixels. The crossings made by red dashed lines in Figure 1.9 represent the new added pixels to the estimated HR image. Notice that the HR image is not in its final stage, and still there are some works to be applied to it, as it will be clear later in this dissertation.

SR reconstruction starts from the LR image sequence represented in the upper row of Figure 1.9 and can be achieved by the following minimization problem, as it will be explained later,

$$\hat{\mathbf{x}}, \hat{\mathbf{s}} = \arg\min_{\mathbf{x},\mathbf{s}} \frac{\beta}{2} \sum_{q=1}^{Q} \| \mathbf{B}_q(\mathbf{s}_q)\mathbf{x} - \mathbf{y}_q \|^2 + \gamma \, \mathbf{Q}(\mathbf{x}), \tag{1.2}$$

where β and γ are positive parameters, $\mathbf{Q}(\mathbf{x})$ is a regularization term, and $\mathbf{s} = (\mathbf{s}_1, \cdots, \mathbf{s}_Q)$. If the LR images were previously registered the motion vectors $\mathbf{s}_q$ would be known, and the only unknown to be estimated by the SR process would be $\mathbf{x}$. Otherwise, which is usually the case, the input images are not registered and the motion vectors have to be estimated like the other unknown.

SR has been already applied to many fields like high performance color liquid crystal display screens, remote sensing, and medical imaging. Also, it has been used to enhance the resolution of still images from video sequences. For an extended list of applications using SR, refer to [6].

SR is different from, and expected to perform better than, interpolation techniques. Interpolation uses only one image to increase its spatial resolution, but it does not enhance the quality of the estimated image. On the contrary, it usually adds some smoothness and loss of some edges is expected. Examples of interpolation methods are:

- Bilinear interpolation: the output pixel value is a weighted average of the nearest four pixel values. In Figure 1.10, the intensity value at the point (m, n) is calculated, using

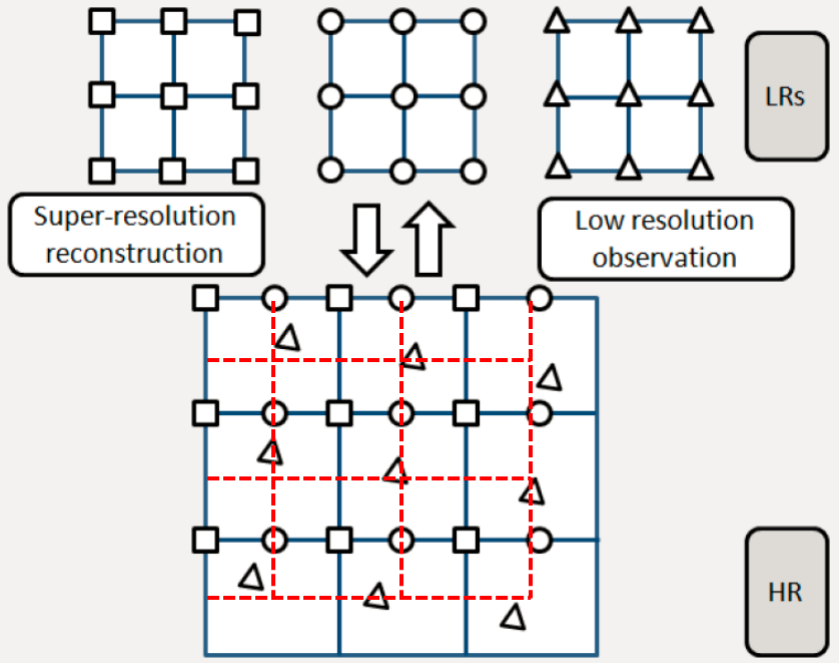

Figure 1.9: SR Estimation. Upper part: three LR images each of resolution= 9. Lower part: estimated HR image of resolution=36, formed by the original pixels in LR observation and the crossings made by the red dashed lines (P=2).

bilinear interpolation by,

$$BIL(m,n) = (1-a)(1-b)\mathbf{x}(i,j) + a(1-b)\mathbf{x}(i+1,j) + ab\mathbf{x}(i+1,j+1) + (1-a)b\mathbf{x}(i,j+1), \tag{1.3}$$

where a, b are respectively the horizontal and vertical displacements of the point (m,n) with respect to the top left neighboring pixel (i,j).

- Bicubic interpolation: the output pixel value is a weighted average of pixel values in the nearest neighborhood. While the process is similar to that in bilinear interpolation, however, the neighboring 16 pixels are used in the estimation process, and the result is a smoother image with fewer interpolation artifacts compared to the bilinear interpolation.

It is worth to discuss here the case where, in the model in Equation (1.1), both warping $\mathbf{C}(\mathbf{s})$ and down-sampling matrices are the identity matrix, and so we only have the blur matrix $\mathbf{H}$, the modeling becomes

$$\mathbf{y}_q = \mathbf{H}_q\mathbf{x} + \mathbf{n}_q, \tag{1.4}$$

where again $\mathbf{y}_q$ is the observed image, $\mathbf{H}_q$ is the blur matrix applied to the original image $\mathbf{x}$, and $\mathbf{n}_q$ is the noise accompanying the blur operation. In this case, it is required to remove the blur from the observed image, and the problem becomes an Image Deconvolution (ID), or deblurring, problem. If $\mathbf{H}$ in the equation is assumed known then the problem falls into the

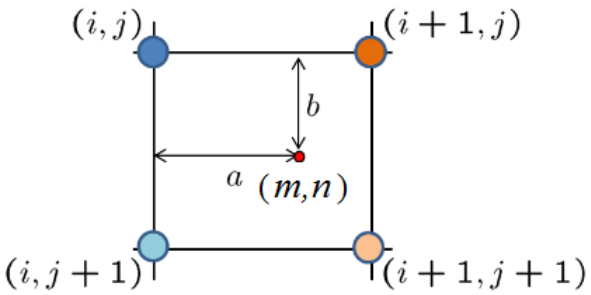

Figure 1.10: Bilinear interpolation. Given **x** at four neighboring pixels, find the intensity value at (m,n)

Non-Blind Image Deconvolution (NBID), the more realistic case is where the matrix $\mathbf{H}_q$ has to be estimated, then the problem turns to be of the Blind Image Deconvolution (BID) type. Notice Equation (1.4) also describes the image deconvolution problem from multiple images (see [7]), if the deconvolution is made from only one single observation (see [8]), then the subscript q can be discarded.

ID is a post processing step to estimate a better quality image by restoring the high frequency content lost in the acquisition process. BID techniques can be included in the SR problem; by this the BID can form an additional step in SR post processing techniques. However, we will not go further in ID direction, as this work is devoted mainly to the SR problem from CS observations, assuming the blur is known.

Finally, it is worth noting that the term SR has been used in other research areas as well. For example, in the field of optics, SR refers to a set of restoration procedures that seek to recover the information beyond the diffraction limit. In the scanning antenna research, SR techniques are exploited to resolve two closely spaced targets when a one-dimensional stepped scanning antenna is used (see [9]). It has also been used to refer to the problem of increasing the resolution of an image using learning techniques, a problem not addressed in this thesis (see [10–12]).

1.1.5 Compressed Sensing

All classical compression techniques still obey the Nyquist's theorem, and must firstly sample the signal at a high rate and then compress it. Hence, the limitation on the sampling step still holds. Alternatively, CS is a new framework to sense in a compressed form data during the acquisition process itself, on sampling rates that can be lower than that of Nyquist's theorem. CS calculates projections of an image to represent it, rather than its original pixels.

CS, or compressed sampling, designs efficient sampling protocols to better capture only the useful information in an image utilizing sparsity property. Assuming sparsity of an image in a transformed domain, then many transformed image components can be neglected as them introduce minimal information. As the significant components, those bearing most information, are not known a priori, a high incoherence between the sparse representation and the one utilized for sensing the image is required, see [13–15].

Figure 1.11, shows the design of a typical CS image/video camera, designed by Rice University. The camera architecture employs a digital micromirror array to optically calculate linear projections of the scene onto pseudorandom binary patterns. Its key hallmark is its ability to obtain an image or video with a single detection element, a single pixel, while measuring the scene fewer times than the number of pixels/voxels. Since the camera relies on a single photon detector, it can also be adapted to image at wavelengths where conventional CCD and CMOS imagers are blind.

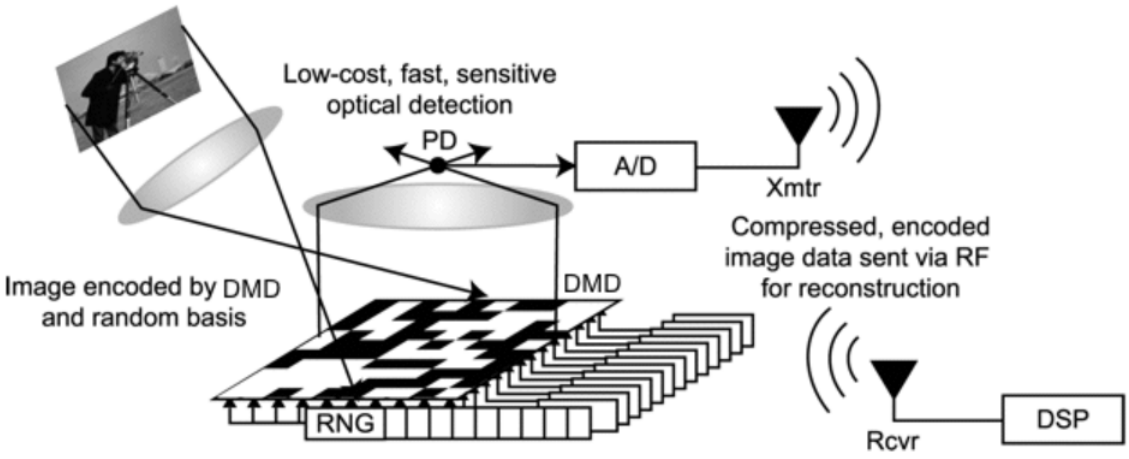

Figure 1.11: Typical CS camera

To model the process, let us assume that we have an $P \times Q$ image. The rectangular matrix can be converted to the $N \times 1$ vector, $\mathbf{x}$, with $N = PQ$, as shown in Figure 1.12. The sampling, or measurement, process can be modeled by a 2-dimensional $M \times N$matrix $\mathbf{\Phi}$, with $M \leq N$. The sensing process is equivalent to multiplying $\mathbf{\Phi}$ by $\mathbf{x}$ to give the $M \times 1$ observation vector $\mathbf{y}$. In the figure M=8, N=16, and the measurement matrix uses real valued entries, as will be explained later. CS theory establishes that a limited number of projections of the image, represented as entries of $\mathbf{y}$, are needed to recover the original image $\mathbf{x}$ efficiently. Mathematically,

$$\mathbf{y} = \mathbf{\Phi x} + \mathbf{n}, \tag{1.5}$$

where $\mathbf{n}$ represents the measurement noise assumed to be additive. Every entry in $\mathbf{y}$ is a projection of the original image, obtained by multiplying the corresponding row in $\mathbf{\Phi}$ by $\mathbf{x}$.

To recover the image $\mathbf{x}$ from the observation $\mathbf{y}$, CS theory relies on the idea that the recovered image should be sparse in a transformed domain, that is, we can use the transform basis $\mathbf{W}$ to find the transform coefficients $\mathbf{a}$ such that

$$\mathbf{x} = \mathbf{Wa}, \tag{1.6}$$

where $\mathbf{W}$ is an $N \times N$ matrix, and $\mathbf{x}$ is said to be S-sparse if only S of the $\mathbf{a}$ components of its representation in the $\mathbf{W}$ basis are non vanishing. Then Equation (1.5) becomes

$$\mathbf{y} = \mathbf{\Phi W a} + \mathbf{n}. \tag{1.7}$$

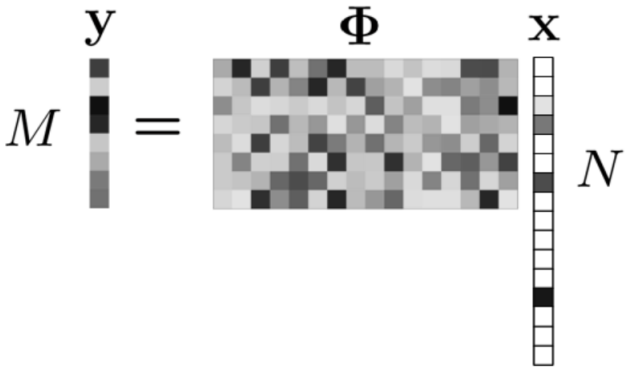

Figure 1.12: Compressed sensing acquisition model. Measurement matrix $\mathbf{\Phi}$ with real entries, M=8, N=16

The coherence μ, of a CS system measures the maximum correlation between the measurement basis and transform basis vectors. It can be expressed as:

$$\mu = \sqrt{N} \max_{k,j} | \mathbf{\Phi}_k \mathbf{W}_j |, \tag{1.8}$$

where $\mathbf{\Phi}_k$ represents the k–th vector of the $\mathbf{\Phi}$ basis, $\mathbf{W}_j$ represents the j–th column in $\mathbf{W}$ with $1 \leq j \leq N$, and $|\,.\,|$ is the absolute value. In Equation (1.8), if matrices used were in normalized form, which is usually the case, then the range of possible values for μ is $1 \leq \mu \leq \sqrt{N}$. For a CS theory efficient application, CS systems coherence coefficient values μ have to be low.

A measurement matrix $\mathbf{\Phi}$ obeys the Restricted Isometry Property (RIP) of order S if the isometry constant δ_S of $\mathbf{\Phi}$ is not too close to one for each integer $S = 1, 2, \cdots$. The δ_S is defined as the smallest number such that the following holds for all S-sparse vectors of $\mathbf{x}$

$$(1 - \delta_S) \| \mathbf{x} \|^2 \leq \| \mathbf{\Phi x} \|^2 \leq (1 + \delta_S) \| \mathbf{x} \|^2 \tag{1.9}$$

This is equivalent also to say that all subsets of S columns taken from $\mathbf{\Phi}$ are nearly orthogonal. Notice that the columns cannot be exactly orthogonal since number of columns usually is larger than number of rows in $\mathbf{\Phi}$, see [13, 16].

A random sensing matrix $\mathbf{\Phi}$ and a basis $\mathbf{W}$ allowing an S-sparse representation of $\mathbf{x}$ will have the RIP if the following expression is accomplished

$$M \geq c.S \log(N/S), \tag{1.10}$$

where c is a constant. This ensures that the reconstruction of an $\mathbf{x}$ image with an S–sparse representation in a vector basis can be obtained from a compressed sensing observation $\mathbf{y}$ through the following minimization problem.

$$\hat{\mathbf{a}} = \arg\min_{\mathbf{a}} \frac{\alpha}{2} \| \mathbf{\Phi W a} - \mathbf{y} \|^2 + \tau \| \mathbf{a} \|_1, \tag{1.11}$$

where α and τ are positive parameters. $\| \,.\, \|$ is the Eucledian norm and $\| \,.\, \|_1$ is the l_1 norm.

CS is a promising technology which decreases the acquisition time and memory size by using only one sensor. The use of a single sensor makes it suitable for imaging at wavelengths where CCD and CMOS are blind (see [13] for more information).

1.2 Objectives and Hypothesis

The main objective for this work is to apply SR techniques to multiple compressed sensing LR observations. It is logical to tackle such a problem because it has been shown that a blurred image is compressible in various scenarios and a constrained optimization framework for compressive BID has been proposed [5, 17].

If the blurred observations are sparse in some domain and CS techniques can be applied to a blurred HR image, then the LR images $\{\mathbf{y}_q\}$ at Equation (1.1) are also expected to be sparse in a transformed domain, and CS can be applied to them. So why not to extend this idea to super resolve multiple LR images, by combining CS with SR techniques.

Following this preliminar idea, in a combined Compressed Sensing Super Resolution (CSSR) problem, we have two approaches to solve the problem: The first is the sequential approach, and the second is the alternate approach. The sequential approach consists of three steps: 1) the LR images are reconstructed, 2) the motion parameters are estimated and finally 3) the HR image is estimated. Notice that this sequence is followed only once. The alternate approach estimates the three unknowns simultaneously in an iterative manner. In the alternate approach the previous sequence is repeated, updating at each step the values obtained in the previous iteration. The alternate approach is expected to give better performance, as it will be proved experimentally in this dissertation.

Another objective of this work is to include the estimation of all unknowns in an iterative framework to solve the CSSR problem.

In this work, image registration parameters are assumed to be unknown. The parameters are estimated using four different approaches, as it will be discussed later in this dissertation.

Another important objective of this work is to apply the CSSR approach to PMMW images. Although they are important and powerful in threat detection problems and many other applications, PMMW images have very poor image quality and suffer from small resolution and long acquisition times. The CSSR with its CS acquisition is expected to require shorter acquisition times. Moreover, the SR step can increase the spatial resolution of these acquired images. This has been investigated in Chapter 4 as it will be shown later. Besides, the proposed framework is applied to color images.

1.3 Methodology and Contributions

A strict work plan has been prepared that starts with a wide literature survey to build a deep knowledge of CS and SR techniques. A model to combine both techniques is suggested and tested.

The work starts by assuming that some parameters are known, like the warping and regularization parameters, to simplify matters, then these parameters are estimated as the work progresses. Two types of images will be utilized in the experiments: simulated and real. Numerical measures can be applied only to simulated experiments, so it constituted most of the preliminary work. The simulation followed the suggested degradation model, on which the reconstruction process also depends.

Before presenting the thesis outline, let us mention the main contributions of this work:

- We propose a degradation model to generate CS LR observations. The optimization process of the CSSR framework mainly depends on this degradation model.
- The combined CSSR approach. Until the time of writing this thesis, to the best of our knowledge, there is no published work that combines compressed sensing and super resolution techniques of multiple unregistered observations, except our published works. All existing published works that combine SR with CS perform SR from one single observation. The following papers address the CSSR estimation process:
  - [18]. W. AlSaafin, S. Villena, M. Vega, R. Molina, and A.K. Katsaggelos. Compressive Sensing Super Resolution From Multiple Observations With Application To Passive Millimeter Wave Images. Digital Signal Processing, pages 180-190, 2016. DOI: 10.1016/j.dsp.2015.12.005
  - [19]. Wael Saafin, Miguel Vega, Rafael Molina, and Aggelos K. Katsaggelos. Image Super Resolution From Compressed Sensing Observations. In Image Processing (ICIP), 2015 IEEE International Conference on, pages 4268-4272, Sept 2015. DOI: 10.1109/ICIP.2015.7351611
  - [20]. Wael Saafin, Salvador Villena, Miguel Vega, Rafael Molina, and Aggelos K. Katsaggelos. PMMW Image Super Resolution From Compressed Sensing Observations. In Signal Processing Conference (EUSIPCO), 2015 23rd European, pages 1815-1819, Aug 2015. DOI: 10.1109/EUSIPCO.2015.7362697
- ADMM is used to include the estimation of the unknown regularization parameters. Motion vectors are estimated through ADMM, using four different approaches three of them were published in [18–20], the fourth is presented in this dissertation.
- The proposed CSSR is applied to PMMW images, to be considered as a first processing step, that can serve, and enhance, later processing like threat detection problems. The related work has been published in [18, 20]. Also, the CSSR is applied to color images as will be shown later in this dissertation ([21]).

1.4 Thesis Document Structure

This thesis is presented in the following order:

- The introductory work is presented in Chapter 1 where background is introduced. This covers a discussion on classical digital imaging techniques to compare with CS techniques. SR and ID techniques are discussed for both natural and millimeter wave images.
- In Chapter 2, the state of the art is studied. SR section includes a discussion of image regularizers and some blur models utilized in the literature. CS works are discussed then the CSSR problem is modeled and formulated. Then some PMMW and CS color image works are presented.
- In Chapter 3 the proposed CSSR framework is introduced and stated.
- Experimental results are presented in Chapter 4 for gray scale, PMMW, and color images.
- Conclusions are drawn in Chapter 5. This chapter also includes future work that we consider relevant to CSSR.

Chapter 2

State of the Art

In this chapter we discuss SR works that use images captured using conventional acquisition systems, we then analyze relevant works which utilize images acquired by CS cameras, and finally the proposed Compressive Sensing Super Resolution (CSSR) problem is modeled and formulated.

2.1 Image Super Resolution Works

As explained in Section 1.1.4, the LR observation process can be modeled as follows,

$$\mathbf{y}_q = \mathbf{A}\mathbf{H}_q\mathbf{C}(\mathbf{s}_q)\mathbf{x} + \mathbf{n}_q = \mathbf{B}_q(\mathbf{s}_q)\mathbf{x} + \mathbf{n}_q, \tag{2.1}$$

where $\mathbf{A}$ is a down-sampling matrix, $\mathbf{H}_q$ is a blurring matrix, $\mathbf{C}(\mathbf{s}_q)$ is the warping matrix corresponding to a motion vector $\mathbf{s}_q$, $\mathbf{n}_q$ represents the noise accompanying the process. $\mathbf{B}_q(\mathbf{s}_q)$ is a matrix modeling the imaging process. SR techniques aim at finding an estimate of $\mathbf{x}$ given Q LR images, $\mathbf{y}_q$.

SR research started in 1984 with the pioneer work by Tsai and Huang [22]. Many works since then have addressed the problem (see [3, 6, 9, 23]). Many SR methods have been proposed, which can be grouped into the following classes: Frequency domain based approach [22, 24, 25], interpolation based approach [26], Bayesian approach [27–33], regularization based approach [34–38], and learning based approach [39–41]. There are some variants of the SR problem: an HR image can be reconstructed from multiple LR observed images, it is also possible to reconstruct an HR image sequence from an observed LR image sequence, and finally an HR image can be reconstructed form only one LR observed image using the learning based approach.

In this work we use the regularization-based approach. The basic idea of this approach to solve the ill-posed inverse SR problem, is to introduce in the cost function to be optimized a regularization term constraining the estimation process. This should be sufficient to solve for the unknown HR image. From a Bayesian point view, the data fidelity term corresponds to the

observation model probability distribution, and the regularization term to the prior probability distribution which incorporates our a priori knowledge on the unknown HR image.

In Equation (2.1), beside the HR image $\mathbf{x}$, the warping matrix $\mathbf{C}(\mathbf{s}_q)$ is also unknown and has to be estimated. Those unknowns can be estimated sequentially or simultaneously. In the sequential approach, we use the LR images to estimate the first unknown, that is, the motion vector, just once, then the second unknown is estimated, that is, the HR image, assuming the blur in known. In the simultaneous approach, all unknowns are estimated alternatively in an iterative way, this allows to the estimated unknowns to feed some information into the estimation of the other unknowns. The simultaneous approach produces better results as we will show in the experimental section (see also [18, 30]).

Given the motion vectors $\{\mathbf{s}_q\}$ a regularization based SR solves the following optimization problem,

$$\hat{\mathbf{x}} = \arg\min_{\mathbf{x}} \frac{\beta}{2} \sum_{q=1}^{Q} \| \mathbf{B}_q(\mathbf{s}_q)\mathbf{x} - \mathbf{y}_q \|^2 + \gamma \, \mathbf{Q}(\mathbf{x}), \tag{2.2}$$

where β and γ are positive parameters, and $\mathbf{Q}(\mathbf{x})$ is the regularizer. In the following subsection, we present some regularization terms, $\mathbf{Q}(\cdot)$, utilized in the SR literature.

2.1.1 Image Regularizers

In this section we explore some regularization terms, or priors under the Bayesian approach. For some of these regularizers, we describe SR algorithms which use them. The performance of the selected SR algorithms is compared with the proposed CSSR algorithm in Section 4.4.

- **Huber Markov random field (HMRF)**
  It is a convex non-quadratic regularizer, which results in nonlinear cost functions, used to preserve edges, see [29, 42]. The energy function of an HMRF is defined as:

$$\rho(f_{\mathbf{x}}) = \begin{cases} f_{\mathbf{x}}^2, & if \mid f_{\mathbf{x}} \mid \leq \alpha \\ 2\alpha \mid f_{\mathbf{x}} \mid -\alpha^2, & otherwise \end{cases} \tag{2.3}$$

  where $f_{\mathbf{x}}$ is the first or second order differences of the HR image $\mathbf{x}$, α is a parameter separating the quadratic and the linear regions, that controls the size of discontinuities modeled by the prior by providing a less severe edge penalty. This regularizer has been used in [29] to extract SR frames from video sequences.

- **Total Variation (TV) regularizer**
  The TV regularizer preserves image edges while smooths flat regions and avoids ringing artifacts (see [43]. The TV energy function is defined as

$$\rho(\mathbf{x}) = \| \nabla \mathbf{x} \|, \tag{2.4}$$

  where ∇ is the gradient operator and $\| \, . \, \|$ is the Euclidean norm. It can be approximated using

$$TV(\mathbf{x}) = \sum_{i=1}^{N} \sqrt{(\Delta_i^h(\mathbf{x}))^2 + (\Delta_i^v(\mathbf{x}))^2}, \tag{2.5}$$

where N is the number of pixels in $\mathbf{x}$, $\Delta_i^h(\mathbf{x})$ and $\Delta_i^h(\mathbf{x})$ correspond respectively to the horizontal and vertical first order differences at pixel i.

- **ℓ1 norm regularizer**

  It is similar to the TV regularizer in its capability to preserve edges while imposing smoothness in the rest of image regions. Its energy function is defined as

$$\rho(\mathbf{x}) = \| \nabla \mathbf{x} \|_1, \tag{2.6}$$

  where ∇ is the gradient operator and $\| . \|_1$ is the $\ell 1$ norm, it can be expressed as

$$L1(\mathbf{x}) = \sum_{i=1}^{N} \alpha^h \| \Delta_i^h(\mathbf{x}) \|_1 + \sum_{i=1}^{N} \alpha^v \| \Delta_i^v(\mathbf{x}) \|_1, \tag{2.7}$$

  where $\Delta_i^h(\mathbf{x})$ and $\Delta_i^v(\mathbf{x})$ represent the horizontal and vertical first order differences, respectively, at pixel i, and α^h, α^v are regularizer parameters. Notice here the use of two model parameters α^h and α^v to make this model more adaptable to image characteristics than the TV regularizer case.

  In Section 4.4, we compare the proposed CSSR algorithm with the SR using $\ell 1$ prior (L1S) algorithm [28] which solves the minimization problem in Equation (2.2).

- **The Simultaneous Autoregressive (SAR) regularizer**

  It applies a uniform smoothness to all locations in the image. It is a non sparse prior that reconstructs textures better, see [30]. It uses the Euclidean norm of the second order difference, as follows

$$SAR(\mathbf{x}) = \| C\mathbf{x} \|^2, \tag{2.8}$$

  where C is the Laplacian operator, and $\| . \|$ is the Euclidean norm.

  In Section 4.4, we compare the proposed CSSR algorithm with the SR using SAR prior (SAS) algorithm [30] which solves the minimization problem in Equation (2.2).

- **Bilateral Total Variation (BTV) regularizer**

  BTV preserves edges in the image, (see [34, 42, 44]). It is expressed as:

$$BTV(\mathbf{x}) = \underbrace{\sum_{l=-P}^{P} \sum_{m=0}^{P}}_{l+m \geq 0} \alpha^{|m|+|l|} \| \mathbf{x} - \mathbf{S}_h^l \mathbf{S}_v^m \mathbf{x} \|_1, \tag{2.9}$$

  where matrices $\mathbf{S}_h^l, \mathbf{S}_v^m$ shift the image $\mathbf{x}$ by l, m pixels in the horizontal and vertical directions, respectively; presenting several scales of derivatives. α is a positive parameter less than one, which gives more weight to closer pixels, $\| . \|_1$ is the $\ell 1$ norm and P is a positive integer. The BTV regularizer has been used in [34]. Notice that when $P = 1$, the regularizer becomes the TV regularizer, and a comparison between the two regularizers was performed in [34].

  A fast and robust SR (FRSR) algorithm has been proposed in [34] which employs the $\ell 1$ norm minimization in pursuit of robustness against motion errors and blurring. It uses

the BTV regularizer. The following minimization problem was solved to estimate $\mathbf{x}$

$$\hat{\mathbf{x}} = \arg\min_{\mathbf{x}} \left\{ \sum_{q} \| \mathbf{B}_q \mathbf{x} - \mathbf{y}_q \|_1 + \underbrace{\sum_{l=-P}^{P} \sum_{m=0}^{P}}_{l+m\geq 0} \alpha^{|m|+|l|} \| \mathbf{x} - \mathbf{S}_h^l \mathbf{S}_v^m \mathbf{x} \|_1 \right\}. \tag{2.10}$$

In Section 4.4, we compare the proposed CSSR algorithm with the FRSR algorithm.

- **Generalized Gaussian MRF (GGMRF)**
  It is a convex non-quadratic regularizer, see [42, 45]. It has the following energy function:

$$\rho(\mathbf{x}) = | \mathbf{x} |^p, \tag{2.11}$$

  where $1 < p < 2$. This regularizer tends to overly smooth the whole image including the edges, see [46], and it has been utilized in [45] for tomographic image reconstruction problems.

The combination of some image regularizers in SR and image restoration has been addressed in [30, 47, 48]. In [30, 48] sparse and non sparse priors were combined and applied to the SR image reconstruction problem.

A robust SR (RSR) Algorithm has been proposed in [49] where instead of minimizing the sum of the difference images, a robust median estimator is combined in an iterative process to obtain a SR algorithm. The HR image is estimated iteratively using the following update equation

$$\mathbf{x}^{k+1} = \mathbf{x}^k + Q \cdot \lambda \cdot median\{\mathbf{B}_q^t(\mathbf{B}_q \mathbf{x}^k - \mathbf{y}_q)\}_{q=1}^{Q}, \tag{2.12}$$

where k is the iteration number, Q is the number of LR input images, and λ is a scale factor. The performance of this algorithm is compared with the proposed CSSR algorithm in Section 4.4.

2.1.2 Image Registration

In the previous section, we discussed the modeling of the HR image. However, for the SR image estimation to succeed, it is essential to find a highly accurate image registration of the input LR images. Image registration will give us an estimation of the $\mathbf{s}_q$ motion vectors and consequently of the warping matrix $\mathbf{C}(\mathbf{s}_q)$ appearing in Equation (2.1).

Image registration, in general, overlays multiple images of the same scene taken at different times, from different viewpoints, and/or by different sensors. In the SR problem, image registration finds a geometric transformation to align pixels in various images to the corresponding locations in the estimated HR image, which is considered to be the reference image.

Many methods have been proposed in the literature, see [50] for details. In this work we use the geometric transformation defined next.

The geometric transformations utilized in this dissertation consist of translations and rotations. Assume that it is required to register the image $\mathbf{g}$ with respect to a reference image $\mathbf{x}$, then

the transformation relating pixel g_i to x_i, with coordinates (g_{ih}, g_{iv}) and (x_{ih}, x_{iv}) respectively, is modeled as

$$\begin{bmatrix} g_{ih} \\ g_{iv} \\ 1 \end{bmatrix} = \begin{bmatrix} \cos\theta & -\sin\theta & c \\ \sin\theta & \cos\theta & d \\ 0 & 0 & 1 \end{bmatrix} \begin{bmatrix} x_{ih} \\ x_{iv} \\ 1 \end{bmatrix} \tag{2.13}$$

where θ is the rotation angle, and c, d are the horizontal and vertical displacements, respectively. The motion vector, for observation q, can be expressed as $\mathbf{s}_q = [\theta_q, c_q, d_q]^t$. A detailed description of the registration model is presented later, in Section 2.3.

2.1.3 Blur Model

In this dissertation we assume that the blur affecting the image is known and can be approximated by a relevant blur model. Many models have been proposed in the literature which simulate blur encountered in real world imaging systems. Next we mention some blur models (see [5, 51, 52])

- **1D Motion Blur**
  This type of blur represents the one dimensional (1D) local averaging of neighboring pixels, a common result of camera panning or fast object motion. For example, the horizontal motion blur can be modeled by

$$h(\mathbf{u}) = \begin{cases} \frac{1}{L+1}, & -\frac{L}{2} \leq u_h \leq \frac{L}{2}; u_v = 0 \\ 0, & otherwise \end{cases} \tag{2.14}$$

  where L is assumed to be an even integer, $\mathbf{u} = (u_h, u_v)$, being the pixel range of horizontal and vertical distance u_h, u_v from the current pixel. Motion blur may also occur in two dimensions (2D), e.g., following a random trajectory.

- **Atmospheric Turbulence Blur**
  This type of blur represents a long term exposure through the atmosphere which is typically modeled by a Gaussian Point Spread Function (PSF). A Gaussian blur can be modeled as

$$h(\mathbf{u}) = K\, e^{-\frac{|\mathbf{u}|^2}{2\sigma^2}} \tag{2.15}$$

  where K is a constant ensuring that the blur values sum up to 1, σ^2 is the variance that determines the severity of the blur.

- **Uniform Out-of-Focus Blur**
  This type of blur is primarily due to the effects of the camera focal length and the distance between camera and observed scene. Out-of-Focus blur can coexist with diffraction blur, which depends on the camera aperture size and shape, and the wavelength of the incoming radiation. Accurate knowledge of all these parameters is not frequently available when a picture is taken. When the blur due to poor focusing is large, the following uniform model has been used as an approximation of such PSFs,

$$h(\mathbf{u}) = \begin{cases} \frac{1}{\pi r^2}, & |\,\mathbf{u}\,| \leq r \\ 0, & otherwise \end{cases} \tag{2.16}$$

where r denotes radius and controls the severity of the blur.

A blurred image can be simulated utilizing a blur model by

$$BLURRED = h(\mathbf{u}) * \mathbf{x}, \tag{2.17}$$

where $*$ is the convolution operator.

2.2 Compressed Sensing Works

Different CS image/video cameras have been proposed (see [53–58]). The concept of single pixel camera has been extended to a multi-detector device in [59], where the detectors are placed on an arbitrary grid on the source signal and each detector integrates the source signals only locally to reduce the required measurements, and hence the measurement time, by using more detectors.

Super Resolution (SR) from a single image has benefited from the introduction of CS theory in works like [60–62]. In [63, 64] learning based SR is used to estimate an HR image from a single CS observation of a down-sampled remote sensing image. In [65] the down-sampling is incorporated in the measurement matrix, the CS image is reconstructed in the wavelet domain and the signal is deconvolved in the Fourier domain.

BID from CS measurement has been studied in [5, 66], and NBID in [67–71]. Next we describe selected CS ID works which will be compared with our proposed CSSR algorithm in Section 4.3.

The Large Scale $\ell 1$ regularized (L1-LS) logistic regression algorithm proposed in [67], and Gradient Projection for Sparse Reconstruction (GPSR) algorithm proposed in [68], both solve the following problem

$$\hat{\mathbf{a}} = \arg\min_{\mathbf{a}} \| \mathbf{\Phi H W a} - \mathbf{y} \|^2 + \tau \| \mathbf{a} \|_1 , \tag{2.18}$$

where $\mathbf{y}$ is the CS blurred observation, $\mathbf{\Phi}$ the measurement matrix, $\mathbf{H}$ the blur matrix, $\mathbf{W}$ is the transform domain basis, $\mathbf{a}$ is the transformed domain representation of the original image $\mathbf{x} = \mathbf{W a}$ and τ is a non-negative parameter.

The Compressive Sampling Matching Pursuit (CoSaMP) algorithm proposed in [69] is based on Orthogonal Matching Pursuit (OMP) schemes and produces an s–sparse approximation $\mathbf{z}$ that satisfies

$$\| \mathbf{x} - \mathbf{z} \|_2 \leq C \cdot \max \left\{ \eta , \frac{1}{\sqrt{s}} \| \mathbf{x} - \mathbf{x}_{s/2} \|_1 + \| \mathbf{y} - \mathbf{\Phi z} \|_2 \right\}, \tag{2.19}$$

where C and η are parameters, and $\mathbf{x}_{s/2}$ is the best $(s/2)$–sparse approximation to $\mathbf{x}$.

The NESTerov's Algorithm (NESTA) proposed in [70], and Your ALgorithm for L1 (YALL1) proposed in [71], solve the following problem

$$\hat{\mathbf{x}} = \arg\min_{\mathbf{x}} \| \mathbf{W}^{-1} \mathbf{x} \|_1 \quad \mathbf{s.t.} \quad \| \mathbf{\Phi H x} - \mathbf{y} \| < \epsilon , \tag{2.20}$$

2.3 CSSR Modeling and Formulation

In the Compressed Sensing Super Resolution (CSSR) problem, we are given multiple CS LR observations of a scene to estimate an HR image. The LR images can be considered as a warped, blurred, and down-sampled versions of the HR image to be estimated. Let us assume that the number of input images is Q, the acquisition model for each observation is

$$\mathbf{y}_q = \mathbf{\Phi}\mathbf{z}_q + \mathbf{r}_q \quad q = 1,\dots,Q, \tag{2.21}$$

where $\mathbf{y}_q$ is an $M \times 1$ vector representing the compressed observations, $\mathbf{\Phi}$ is a CS $M \times D$ measurement matrix, $\mathbf{z}_q$ is a column vector of size $D \times 1$ representing the q–th LR image and $\mathbf{r}_q$ represents the observation noise. We denote by R the compression ratio of the measurement system, that is, $R = M/D$, $R \leq 1$.

As shown in Section 2.1 the observation process of the LR observations $\mathbf{z}_q$ in Equation (2.21) can be modeled as follows,

$$\mathbf{z}_q = \mathbf{A}\mathbf{H}_q\mathbf{C}(\mathbf{s}_q)\mathbf{x} + \mathbf{w}_q = \mathbf{B}_q(\mathbf{s}_q)\mathbf{x} + \mathbf{w}_q, \tag{2.22}$$

where $\mathbf{A}$ is a $D \times N$ down-sampling matrix, $D \leq N$, which models the limited resolution of the acquisition system, when capturing the high resolution image, where $N = P^2 D$ and P≥1 is the zooming factor, in each dimension of the image. $\mathbf{H}_q$ is an $N \times N$ blurring matrix, modeling the blur action accompanying the imaging process. In this work, the convolution matrix $\mathbf{H}_q$ is assumed to be known. $\mathbf{C}(\mathbf{s}_q)$ is the $N \times N$ warping matrix for the motion vector $\mathbf{s}_q = [\theta_q, c_q, d_q]^t$, where θ_q is the rotation angle, c_q and d_q are respectively the horizontal and vertical translations of the q–th LR image with respect to the reference frame, and $\mathbf{x}$ is the HR image of size $N \times 1$. Finally, $\mathbf{w}_q$ models the noise associated to the LR acquisition process. We write $\mathbf{B}_q(\mathbf{s}_q) = \mathbf{A}\mathbf{H}_q\mathbf{C}(\mathbf{s}_q)$ for simplicity.

Using Equations (2.21) and (2.22) we can write

$$\mathbf{y}_q = \mathbf{\Phi}\mathbf{B}_q(\mathbf{s}_q)\mathbf{x} + \mathbf{n}_q, \text{ for } q = 1,\dots,Q, \tag{2.23}$$

where $\mathbf{n}_q$ represents the combined CS and LR acquisition noise and $\mathbf{x}$ is the HR image we want to estimate.

Next we describe the sensing matrices we use in this dissertation. The measurement matrix we use ($\mathbf{\Phi}$) is a random circulant Toeplitz matrix. A circulant Toeplitz matrix is a matrix $\mathbf{T}_n$, in which each row is a cyclic shift of the row above. It has the following form

$$\mathbf{T}_n = \begin{bmatrix} t_0 & t_1 & t_2 & \cdots & t_{n-1} \\ t_{n-1} & t_0 & t_1 & & t_{n-2} \\ t_{n-2} & t_{n-1} & t_0 & & \\ \vdots & & & \ddots & \\ t_1 & & & & t_0 \end{bmatrix} \tag{2.24}$$

The entries in the first row are random, following a Gaussian, or Bernoulli distribution. Gaussian, or normal, distribution function is given by

$$f(x|\mu,\sigma) = \frac{1}{\sigma\sqrt{2\pi}}\, e^{-\frac{(x-\mu)^2}{2\sigma^2}} \tag{2.25}$$

where μ and σ^2 are respectively the mean and the standard deviation of the distribution. Bernoulli probability function is given by

$$f(k|p) = p^k(1-p)^{1-k}, \quad \text{for } k \in \{0,1\}, \tag{2.26}$$

where (p) and $(1-p)$ are respectively the probabilities of k being 1 and 0.

Both Gaussian and Bernoulli random circulant Toeplitz matrices were tested to work well in CS [72–74]. In both cases the rows of $\mathbf{\Phi}$ are normalized to 1. However, a Gaussian matrix consists of real entries while a Bernoulli matrix consists of binary entries, and hence it can be synthesized 256×256 practically, see [18, 56]. In this dissertation we used the Bernoulli circulant Toeplitz matrix.

Next we describe the down-sampling matrix ($\mathbf{A}$). Let us assume that we have an image $\mathbf{x}$ of size 256×256, and the zooming factor P=2. We divide the matrix $\mathbf{x}$ into $P \times P$ blocks, then from each block only one pixel value is preserved, and the other three are discarded. The preserved pixels constitute a 128×128 matrix, which is the down-sampled version of $\mathbf{x}$. Notice here that there is no interpolation process neither in the down-sampling nor in the up-sampling process. If the down-sampled 128×128 matrix in the previous example is up-sampled, then each pixel value will form a block in the up sampled image, the upper-left pixel of the four pixels forming this block will have the pixel value from the down-sampled image, the other three pixels will have a zero value.

The blur matrix ($\mathbf{H}$) we used in all experiments utilizes a spatially invariant Gaussian blur filter given by

$$h(\mathbf{u}) = K\, e^{-\frac{|\mathbf{u}|^2}{2\sigma^2}} \tag{2.27}$$

where K is a constant and σ^2 is the blur variance.

Next we describe how to calculate the warping matrix ($\mathbf{C}(\mathbf{s}_q)$). Let us denote the coordinates of the reference HR grid by (u, v) and the coordinates of the $q{-}th$ warped HR grid, after applying $\mathbf{C}(\mathbf{s}_q)$ to $\mathbf{x}$, by (u_q, v_q). Then it holds that

$$u_q = u\cos(\theta_q) - v\sin(\theta_q) + c_q \tag{2.28}$$

$$v_q = u\sin(\theta_q) + v\cos(\theta_q) + d_q. \tag{2.29}$$

Let us denote the displacements between the grids by $\Delta(u_q, v_q)^T = (u, v)^T - (u_q, v_q)^T$. The vector difference between the pixel at (u_q, v_q) and the pixel at its top-left position in the reference HR grid is denoted by $(a_q(\mathbf{s}_q), b_q(\mathbf{s}_q))^T$ (see Figure 2.1), that is,

$$a_q(\mathbf{s}_q) = \Delta u_q - \text{floor}(\Delta u_q), \tag{2.30}$$

$$b_q(\mathbf{s}_q) = \Delta v_q - \text{floor}(\Delta v_q). \tag{2.31}$$

Notice here that the relationships are non linear functions of $\mathbf{s}_q$ due to the trigonometric functions in Equations (2.28) and (2.29). Using bilinear interpolation, the warped image $\mathbf{C}(\mathbf{s}_q)\mathbf{x}$

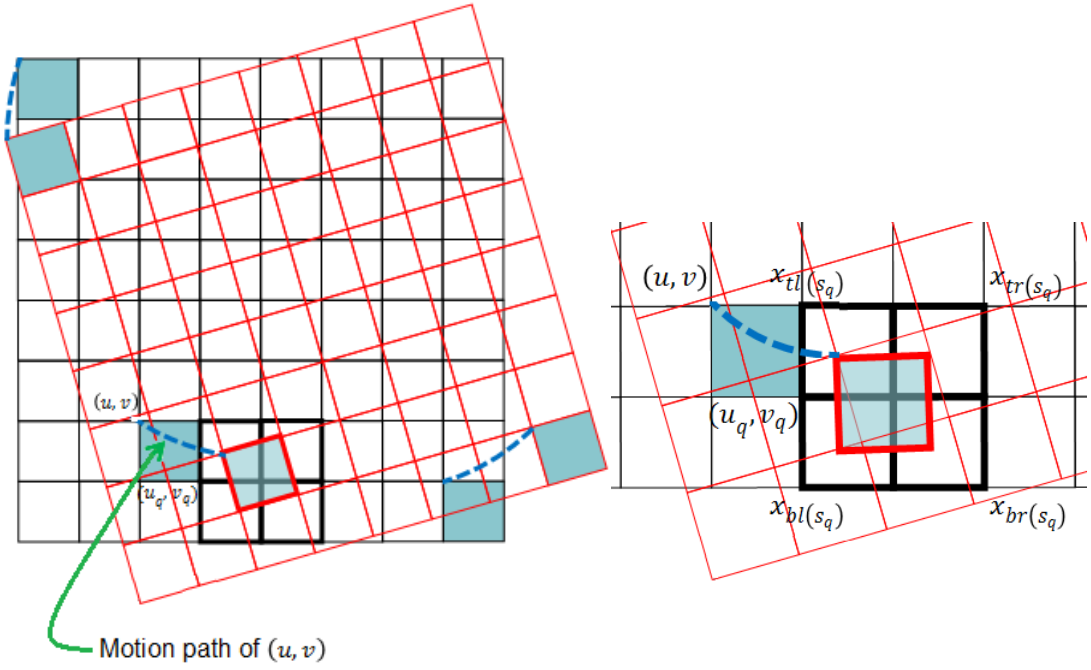

(a) (b)

Figure 2.1: q-th HR grid calculation. (a) HR grid (in black) and the q-th image grid (in red), (b) Detailed view of (a), with the pixel notation used for the bilinear interpolation of grid element (u_q, v_q)

can be approximated to obtain a linear transform matrix in $\mathbf{s}_q$ as (see [18, 30, 37]),

$$\begin{aligned}\mathbf{C}(\mathbf{s}_q)\mathbf{x} \approx \mathbf{D}_{b_q(\mathbf{s}_q)}(\mathbf{I}-\mathbf{D}_{a_q(\mathbf{s}_q)})\mathbf{L}_{\mathbf{bl}(\mathbf{s}_q)}\mathbf{x} + (\mathbf{I}-\mathbf{D}_{b_q(\mathbf{s}_q)})\mathbf{D}_{a_q(\mathbf{s}_q)}\mathbf{L}_{\mathbf{tr}(\mathbf{s}_q)}\mathbf{x} \\ + (\mathbf{I}-\mathbf{D}_{b_q(\mathbf{s}_q)})(\mathbf{I}-\mathbf{D}_{a_q(\mathbf{s}_q)})\mathbf{L}_{\mathbf{tl}(\mathbf{s}_q)}\mathbf{x} + \mathbf{D}_{b_q(\mathbf{s}_q)}\mathbf{D}_{a_q(\mathbf{s}_q)}\mathbf{L}_{\mathbf{br}(\mathbf{s}_q)}\mathbf{x},\end{aligned} \tag{2.32}$$

where $\mathbf{D}_{a_q(\mathbf{s}_q)}$ and $\mathbf{D}_{b_q(\mathbf{s}_q)}$ denote diagonal matrices with the vectors $a_q(\mathbf{s}_q)$ and $b_q(\mathbf{s}_q)$ in their diagonals, respectively. $\mathbf{I}$ is the identity matrix. Matrices $L_\mathbf{z}$ with $\mathbf{z} \in \{\mathbf{bl}(\mathbf{s}_q), \mathbf{br}(\mathbf{s}_q), \mathbf{tl}(\mathbf{s}_q), \mathbf{tr}(\mathbf{s}_q)\}$ are constructed in such a way that the product $L_\mathbf{z}\mathbf{x}$ produces pixels at the bottom-left, bottom-right, top-left, and top-right, locations of (u_q, v_q), respectively. This approximated explicit form presented in Equation (2.32) can be used when we are given the motion vectors of the input LR CS observations.

The noise matrix $(\mathbf{n}_q)$ we used in all experiments is assumed to be white Gaussian noise of zero mean, added to the CS observations. This noise arises during acquisition due to poor illumination, high temperature and electronic circuit noise, see [75].

Let us now show an example to clarify visually the presented warping model. Figure 2.2(a) shows the original Shepp-Logan image $\mathbf{x}$. The original image is warped then blurred then down-sampled, following Equation (2.22) to get $\mathbf{B}_q(\mathbf{s}_q)\mathbf{x}$ for the case $Q = 4$. The warping uses

the following motion vectors

$$\mathbf{s}_1 = \begin{bmatrix} 0 \\ 0 \\ 0 \end{bmatrix}, \mathbf{s}_2 = \begin{bmatrix} 0.0524 \\ 2 \\ -3 \end{bmatrix}, \mathbf{s}_3 = \begin{bmatrix} -0.0698 \\ -1 \\ -2 \end{bmatrix}, \text{and } \mathbf{s}_4 = \begin{bmatrix} -0.0349 \\ 3 \\ -1 \end{bmatrix}. \tag{2.33}$$

To blur the warped image we used a Gaussian blur with variance 5, the down-sampling used a zooming factor P=2. The four generated LR images ($\mathbf{B}_q(\mathbf{s}_q)\mathbf{x}$) are shown in Figure 2.2(b). The simulated LR images then were compressed to get ($\mathbf{\Phi}\mathbf{B}_q(\mathbf{s}_q)\mathbf{x}$), as in Equation (2.23). Firstly the image is compressed using a compression ratio R=0.6 then noised by an additive white noise of SNR=30dB. The four noised CS observations are shown in Figure 2.2(c). Figures 2.2(d,e,f) show the results obtained for the Lena image following the same procedure.

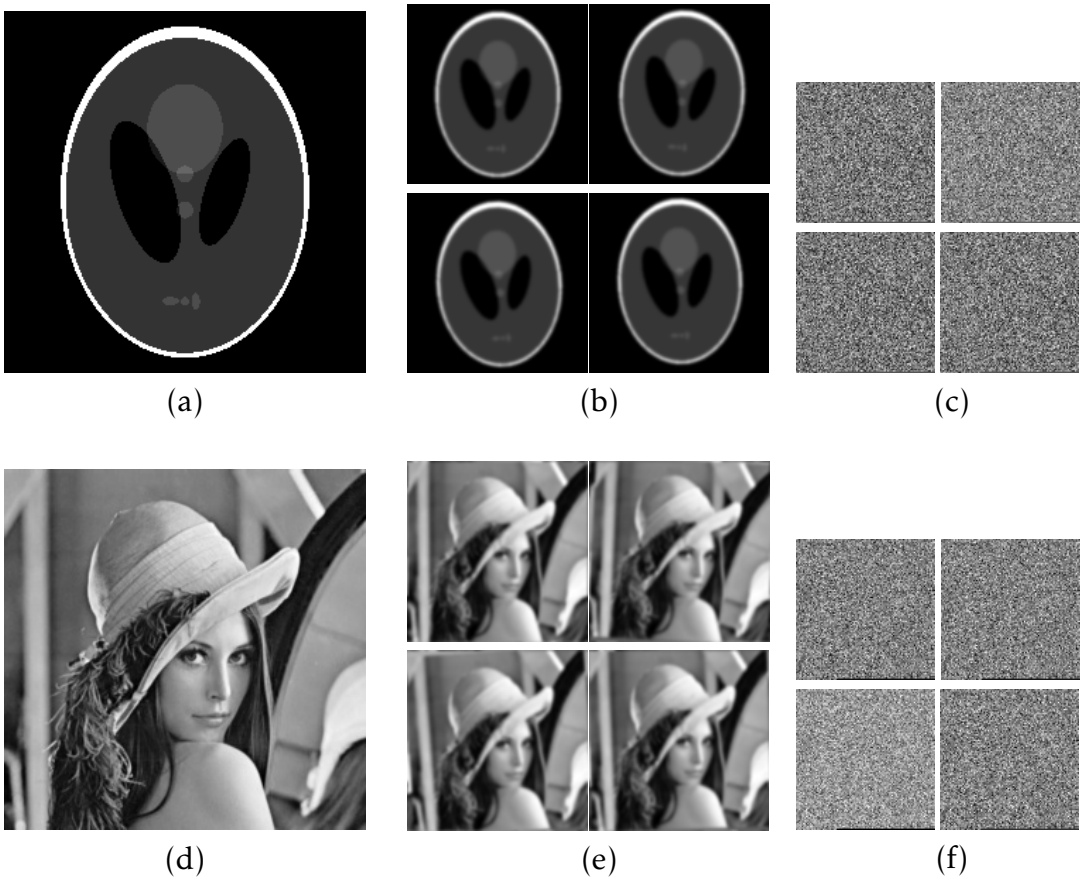

Figure 2.2: Simulation process. Warped with motion vectors $(0,0,0)^t$, $(.0524,2,-3)^t$, $(-.0698,-1,-2)^t$, $(-.0349,3,-1)^t$, Gaussian blur of variance 5, zooming factor 2, compression ratio R=0.6, SNR of added noise 30dB (a) Original Shepp-Logan image, (b) Four simulated LR images., (c) Four CS observations, (d) Original Lena image, (e) Four simulated LR images, (f) Four CS observations.

CSSR aims at finding an estimate for the HR image in Figure 2.2(a) given some noised

CS observations, like those in Figure 2.2(c). Next we formulate the minimization problem we propose to do so.

Since $\mathbf{z}_q$ in Equation (2.22) represents translated and rotated LR versions of the original image $\mathbf{x}$, which are assumed to be compressible in a transformed domain, we can estimate the original HR image by first recovering the LR images using CS techniques and then recover the HR image using standard SR techniques on the recovered LR images. To be precise, if we assume that the LR images are sparse in a transformed domain with $\mathbf{z}_q$=$\mathbf{W}\mathbf{a}_q$, where $\mathbf{W}$ is a sparse promoting transformation of size $D\times D$ and $\mathbf{a}_q$ is the q–th transformed coefficient vector, we want to recover all $\mathbf{z}_q$ using a CS reconstruction technique.

The CS recovery methods available usually utilize the $\ell 1$ minimization, or Greedy methods. Examples on Greedy methods are Matching Pursuit (MP), Orthogonal MP (OMP), Subspace Pursuit (SP), regularized OMP (ROMP), Iterative Hard Shareholding (IHT) algorithm, see [76–80] for details. In this dissertation we use $\ell 1$ minimization to solve the CS problem. Next we introduce and justify its use.

Actually what is required in a CS recovery is to solve this equation

$$\hat{\mathbf{a}} = \arg\min_{\mathbf{a}} \| \mathbf{a} \|_0 \quad \text{subject to} \quad \mathbf{a} : \| \mathbf{\Phi W a} - \mathbf{y} \|^2 \leq \epsilon \,, \tag{2.34}$$

where the l_0 norm $\| \mathbf{a} \|_0$ counts the number of nonzero entries in a vector $\mathbf{a}$, $\| \, . \, \|$ is the Euclidean norm, and ϵ is a small value that determines the accuracy of the estimation process. While the Euclidean norm is convex, the zero norm is non convex, that makes the problem very difficult to solve. A way to make the problem more tractable is to replace the zero norm with its convex approximation $\| \, . \, \|_1$, that is the $\ell 1$ norm. Hence the problem becomes,

$$\hat{\mathbf{a}} = \arg\min_{\mathbf{a}} \| \mathbf{a} \|_1 \quad \text{subject to} \quad \mathbf{a} : \| \mathbf{\Phi W a} - \mathbf{y} \|^2 \leq \epsilon \,, \tag{2.35}$$

All constituting terms are convex now, hence the minimization problem is computationally feasible. Moreover, there are a variety of reasons which justify the use of $\ell 1$-minimization for sparse signal recovery, see [81]. Converting the constrained optimization to a none constrained one gives,

$$\hat{\mathbf{a}} = \arg\min_{\mathbf{a}} \frac{\eta}{2} \| \mathbf{\Phi W a} - \mathbf{y} \|^2 + \tau \| \mathbf{a} \|_1, \tag{2.36}$$

where η, τ are positive parameters. This is the minimization problem we use in our dissertation, which has been also utilized in [15, 17, 82]. Therefore, we can recover the $\mathbf{z}_q$ in Equation (2.22) from the model in Equation (2.21) by solving

$$\hat{\mathbf{a}}_q = \arg\min_{\mathbf{a}_q} \frac{\eta}{2} \| \mathbf{\Phi W a}_q - \mathbf{y}_q \|^2 + \tau \| \mathbf{a}_q \|_1 \,. \tag{2.37}$$

Then defining $\hat{\mathbf{z}}_q = \mathbf{W}\hat{\mathbf{a}}_q$ and $\mathbf{s} = (\mathbf{s}_1, \ldots, \mathbf{s}_Q)$ and using the degradation model in Equation (2.22), we can estimate the original image by solving

$$\hat{\mathbf{x}}, \hat{\mathbf{s}} = \arg\min_{\mathbf{x},\mathbf{s}} \frac{\beta}{2} \sum_q \| \mathbf{B}_q(\mathbf{s}_q)\mathbf{x} - \hat{\mathbf{z}}_q \|^2 + \alpha \, Q(\mathbf{x}), \tag{2.38}$$

where α and β are non-negative parameters, and the term $Q(\mathbf{x})$ is described next. In [18] the following regularization term was used for the image

$$Q(\mathbf{x}) = \sum_{d\in\Delta}\sum_{i=1}^{N} \log(|\omega_d^{\mathbf{x}}(i)|), \tag{2.39}$$

where $\omega_d^{\mathbf{x}}(i)$ is the i-th pixel of the filtered image, and

$$\boldsymbol{\omega}_d^{\mathbf{x}} = \mathbf{F}_d\mathbf{x}, \tag{2.40}$$

where $\mathbf{F}_d$ is a high-pass filter operator, and the index $d \in \Delta$ identifies one of the members of the used filter set. In this paper we have used a filter set with elements $\Delta = \{h, v, hv, vh, hh, vv\}$, where h, v represent the first order horizontal and vertical difference filters, hv and vh represent first order differences along diagonals, and hh and vv the horizontal and vertical second order differences. The regularization term favors sparsity of the high-pass filtered images $\mathbf{F}_d\mathbf{x}$, and corresponds to the Super-Gaussian log prior used in blind deconvolution [83].

Since the log function can not be differentiated at zero, we consider in this work the following robust version of the log regularizer

$$\log_\epsilon(|s|) = \begin{cases} \log(|s|) & \text{for } |s| \geq \epsilon \\ \frac{s^2}{2\epsilon^2} - (\frac{1}{2} - \log(\epsilon)) & \text{for } 0 \leq |s| \leq \epsilon \end{cases} \tag{2.41}$$

and replace $Q(\mathbf{x})$ in Equation (2.39) by

$$Q(\mathbf{x}) = \sum_{d\in\Delta}\sum_{i=1}^{N} \log_\epsilon(|\omega_d^{\mathbf{x}}(i)|), \tag{2.42}$$

where we have removed the dependency of $Q(\cdot)$ on ϵ for simplicity.

We have two approaches to solve the CSSR problem: the sequential approach and the alternate approach (see [6]). The latter approach alternates between compressive sensing reconstruction, registration parameter estimation, and reconstruction of the HR image. The former approach estimates the unknowns sequentially, one after the other, as follows. Firstly, the LR images are reconstructed using Equation (2.37), then motion parameters are estimated and finally the HR image is estimated using Equation (2.38). Notice here that after an unknown is estimated, the sequential approach does not return back to it again, and every unknown is estimated only once.

As we will show in the experimental part, combining the two optimization problems in Equations (2.37) and (2.38) above into a simultaneous one leads to an improved performance, as this enables better exploitation of the compressibility of the LR observations using the additional information obtained from the estimated HR image, and the updated registration parameters. Hence, in the following, this alternate approach has been adopted. According to it, let $\mathbf{a} = (\mathbf{a}_1, \ldots, \mathbf{a}_Q)$ and define

$$L(\mathbf{x}, \mathbf{a}) = \frac{\eta}{2}\sum_{q=1}^{Q} \| \boldsymbol{\Phi}\mathbf{W}\mathbf{a}_q - \mathbf{y}_q \|^2 + \tau \sum_{q=1}^{Q} \| \mathbf{a}_q \|_1 + \alpha\, Q(\mathbf{x}) \tag{2.43}$$

Then we approach the Compressed-Sensing Super Resolution (CSSR) problem by solving the following constrained optimization problem

$$\begin{aligned} &\min L(\mathbf{x},\mathbf{a}) \\ &\text{s.t.} \quad \mathbf{B}_q(\mathbf{s}_q)\mathbf{x} = \mathbf{W}\mathbf{a}_q, \text{for } q = 1,\ldots,Q. \end{aligned} \tag{2.44}$$

This is the approach we will describe and use in Chapter 3. Notice that in Equation (2.43) we could have also introduced a regularizer on the motion vector $\mathbf{s} = (\mathbf{s}_1,\ldots,\mathbf{s}_Q)$, similar to [20, 30]. However, we have experimentally found that it is not necessary to use regularization on the motion vectors.

Still we did not describe the transform basis ($\mathbf{W}$) that serves well in the CS reconstruction. Suitable transformed domains for CS are Discrete Cosine Transform (DCT), Discrete Wavelet Transform (DWT) and Discrete Fourier Transform (DFT). DWT is usually preferred over DCT because it better enables the removal of blocking artifacts [84]. In this dissertation we adapted interchangeably the DCT, and the DWT. Both are described next.

DCT attempts to make use of correlated data in the $\mathbf{z}_q$ image. In the one-dimensional (1D) DCT, the signal is converted into a sum of cosine functions oscillating at different frequencies. It can be expressed as follows

$$\mathbf{a}_q(k) = \omega(k)\sum_{i=1}^{D}\mathbf{z}_q(i)\cos\left[\frac{\pi}{2D}(2i-1)(k-1)\right], \quad k = 1,\cdots,D, \tag{2.45}$$

where $\mathbf{z}_q$ is expressed in the vector form, and

$$\omega(k) = \begin{cases} \frac{1}{\sqrt{D}}, & k = 1 \\ \sqrt{\frac{2}{D}}, & 2 \le k \le D \end{cases} \tag{2.46}$$

where D is the number of pixels in $\mathbf{z}_q$. The inverse 1D-DCT reconstructs a sequence from its transform coefficients by

$$\mathbf{z}_q(i) = \sum_{k=1}^{D}\omega(k)\mathbf{a}_q(k)\cos\left[\frac{\pi}{2D}(2i-1)(k-1)\right], \quad i = 1,\cdots,D, \tag{2.47}$$

DWT invokes two types of filters; the wavelet filter and the scaling vector. The wavelet filter is a high pass filter, and the scaling vector is a low pass filter. After applying a 1-level Haar DWT on an image $\mathbf{z}_q$ in the matrix form, we decompose it into four frequency bands, namely the approximation (LL_1), horizontal (LH_1), vertical (HL_1), and diagonal (HH_1) sub-bands. This DWT decomposition at the 1-level is shown in Figure 2.3 for Barbara image to represent the LR image $\mathbf{z}_q$. The original image is shown in Figure 2.3(a), while Figure 2.3(b) shows the four down-sampled sub-bands: approximation, horizontal, vertical and diagonal bands. Notice that if we append the four bands together in one vector we obtain the 1-level coefficient vector which has the same size as $\mathbf{z}_q$.

If the 1-level DWT is applied again to the approximation sub-band LL_1, then we obtain the 2-level DWT, and hence we will have the new sub-bands LL_2, LH_2, HL_2, and HH_2. Applying DWT again to the resulting approximation sub-band LL_2, then we will have the 3-level DWT,

(a) (b)

Figure 2.3: 1-level discrete wavelet transform. (a) Barbara image (b) DWT decomposition

with the new added bands LL_3, LH_3, HL_3 and HH_3. An illustration of the process is shown in Figure 2.4.

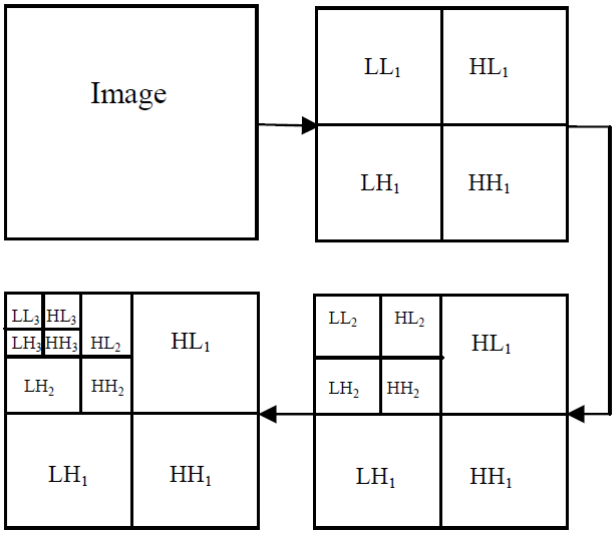

Figure 2.4: 3-level discrete wavelet transform decomposition.

Inverse Haar DWT firstly computes a reconstructed approximation coefficient matrix $\widehat{LL_2}$

from LL_3, LH_3, HL_3, and HH_3. Notice that the size of $\widehat{LL}_2$ will be equal to the sum of the four smaller sub-bands. Then using $\widehat{LL}_2$, LH_2, HL_2 and HH_2, the first level approximation $\widehat{LL}_1$ is computed. Finally, the reconstructed approximation of $\hat{\mathbf{z}}_q$ is computed by taking the inverse Haar transform of the bands $\widehat{LL}_1$, LH_1, HL_1 and HH_1.

In this dissertation we used 3-level Haar DWT as the wavelet transform domain.

Chapter 3

Compressive Sensing Super Resolution Algorithm

Once the CSSR problem has been formulated in the previous chapter, this chapter presents our CSSR approach to solve it. All the processing steps are investigated to describe their specific merits. Then the algorithm is stated. The CSSR method can also be applied to Color CS images through our second proposed algorithm, CCSSR, which is presented in this chapter.

The CSSR problem has a large number of unknowns: the HR image $\mathbf{x}$, the sparse coefficients $\mathbf{a}$ corresponding to each LR image, the motion vectors $\mathbf{s}$, and the parameters η, τ, α that affect the solution inherently. In such a case, one should design a smart strategy to tackle the problem efficiently, and to try many possible solutions, sometimes trials may fail, others may succeed.

Hence, before continuing in describing the resulting approach, it is worthwhile to give a historical background to describe the road map followed in the preparation of this work, and to discuss not only those adopted techniques, but also those which have not been adopted in the last format of our solution to the CSSR problem.

3.1 Preliminary Work

To simplify matters, in the problem we started with there were two simulated CS observations corresponding to the LR images. Given the motion vectors and the blur, the observations were degraded as in Equation (2.1). The image was warped, then degraded by a Gaussian blur and down-sampled, with a zooming factor P=2. The observation was then compressed using a circulant Gaussian Toeplitz measurement matrix and finally White Gaussian noise, with SNR=40dB, was added to the compressed observations.

From the CS observations the sparse coefficient vectors can be estimated using the following

l_1 minimization problem

$$\hat{\mathbf{a}}_q = \arg\min_{\mathbf{a}_q} \frac{\alpha}{2} \| \mathbf{\Phi W a}_q - \mathbf{y}_q \|^2 + \tau \| \mathbf{a}_q \|_1, \quad \text{for } q = 1, \cdots, Q. \tag{3.1}$$

Notice that the sparse coefficients can be estimated using the algorithm in [82]. We used the 3-level Haar wavelet transform as a transform basis. The estimation process is performed for each observation separately. Then the estimated LR images $\mathbf{W}\hat{\mathbf{a}}_q$ can be super resolved to estimate an HR image using

$$\hat{\mathbf{x}} = \arg\min_{\mathbf{x}} \frac{\beta}{2} \sum_q \| \mathbf{A H}_q \mathbf{C}(\mathbf{s}_q)\mathbf{x} - \mathbf{W}\hat{\mathbf{a}}_q \|^2 + \alpha\, Q(\mathbf{x}), \tag{3.2}$$

where we used the explicit form of $\mathbf{C}(\mathbf{s}_q)$ as in Equation (2.32), assuming known motion vectors. We used an l_p quasi-norm with $0 < p < 1$ to serve as the regularization term $Q(\mathbf{x})$. This prior has been used in compressive image deconvolution [5]. It can be expressed as

$$Q(\mathbf{x}) = \sum_d 2^{1-o(d)} \sum_i | \Delta_i^d(\mathbf{x}) |^p, \tag{3.3}$$

where $o(d) \in \{1, 2\}$ denotes the order of the difference operator $\Delta_i^d(\mathbf{x})$ at pixel i, $d \in \{h, v, hh, vv\}$, h, v denote horizontal, vertical first order differences, hh, vv denote horizontal, vertical second order differences, and $0 < p < 1$. This $Q(\mathbf{x})$ regularizer can be bounded by a tractable functional $R(\mathbf{x},\mathbf{V})$ such that

$$Q(\mathbf{x}) \leq R(\mathbf{x},\mathbf{V}). \tag{3.4}$$

In Equation (3.4) $R(\mathbf{x},\mathbf{V})$ is defined as

$$R(\mathbf{x},\mathbf{V}) = \frac{p}{2} \sum_d 2^{1-o(d)} \sum_i \frac{[\Delta_i^d(\mathbf{x})]^2 + \frac{2-p}{p} v_{d,i}}{v_{d,i}^{1-p/2}}, \tag{3.5}$$

where $\mathbf{V}$ is a diagonal matrix with elements $v_{d,i} > 0$, and

$$v_{d,i} = [\Delta_i^d(\mathbf{x}_0)]^2, \tag{3.6}$$

where $\mathbf{x}_0$ is an initial estimate of $\mathbf{x}$ calculated by adding the up-sampled LR reconstructed images, $\mathbf{W}\hat{\mathbf{a}}_q$. The derivation for the bound in Equation (3.5) is presented in [85]. The minimization problem in Equation (3.2) gives the following equation for estimating $\mathbf{x}$,

$$\mathbf{x} = \left[\beta \sum_{q=1}^{Q} \mathbf{B}_q^t(\mathbf{s}_q)\mathbf{B}_q(\mathbf{s}_q) + \alpha p \sum_d 2^{1-o(d)} \Delta^{d^t} \mathbf{\Lambda}_d \Delta^d \right]^{-1} \beta \sum_{q=1}^{Q} \mathbf{B}_q^t(\mathbf{s}_q)\mathbf{W}\hat{\mathbf{a}}_q \tag{3.7}$$

where $\mathbf{\Lambda}_d$ is a diagonal matrix with elements $v_{d,i}^{p/2-1}$ in the diagonal, and Δ^d is the convolution matrix of the difference operator $\Delta_i^d(\cdot)$.

As an example, we degraded the Barbara image to simulate two CS LR images. The reconstructed LR images are shown in Figure 3.1(a). Figure 3.1(b) shows the HR initial image of

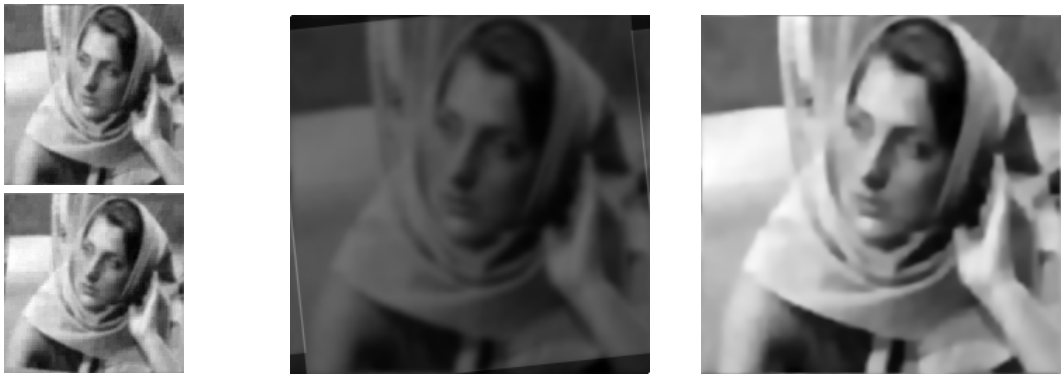

(a) (b) (c)

Figure 3.1: Sequential estimation process. Observations have been simulated using Gaussian Blur of variance 3, zooming factor P=2, Gaussian circulant Toeplitz measurement matrix with compression ratio R=0.8 and additive noise of SNR=40dB. (a) LR reconstructed observations, (b) initial estimate of HR image, PSNR=9.8 dB, (c) estimated HR image, PSNR=23.2 dB

PSNR=9.8 dB, and the reconstructed image is shown in Figure 3.1(c), with PSNR=23.2 dB. We used $p = 0.8$ in this and the following experiments.

Notice that the unknowns were estimated sequentially, not iteratively. Actually, this was the simplest initial approach to the problem, and the successful reconstruction proved the feasibility of our study. This encouraged us to go further in the solution, to jointly estimate the unknowns using the constrained optimization in Equation (2.44), repeated again here,

$$\begin{aligned} \min & \left\{ \frac{\eta}{2} \sum_{q=1}^{Q} \| \mathbf{\Phi W a}_q - \mathbf{y}_q \|^2 + \tau \sum_{q=1}^{Q} \| \mathbf{a}_q \|_1 + \alpha\, Q(\mathbf{x}) \right\} \\ & \text{s.t.} \quad \mathbf{B}_q(\mathbf{s}_q)\mathbf{x} = \mathbf{W a}_q, \text{ for } q = 1, \ldots, Q, \end{aligned} \tag{3.8}$$

where $\mathbf{\Phi}$ is the CS measurement matrix, $\mathbf{W}$ is the transformation matrix, $\mathbf{a}_q$ is the transformed coefficient vector corresponding to the $q-$th CS observation $\mathbf{y}_q$, $\mathbf{Q}(\mathbf{x})$ is the regularization term being, at that time, the l_p quasi norm defined in Equation (3.3) for which the upper bound defined in Equation (3.5) was used, $\mathbf{B}_q(\mathbf{s}_q) = \mathbf{A}\mathbf{H}_q\mathbf{C}(\mathbf{s}_q)$ is the modeling matrix, the motion vectors $\mathbf{s}_q$ are assumed to be known, and η, τ, α are positive parameters.

This constrained optimization problem can be converted into an unconstrained optimization one, using the Alternate Direction Method of Multipliers (ADMM) [86, 87]. We define the following augmented Lagrangian functional

$$L(\mathbf{x},\mathbf{a},\boldsymbol{\lambda}) = \frac{\eta}{2}\sum_{q=1}^{Q} \| \boldsymbol{\Phi}\mathbf{W}\mathbf{a}_q - \mathbf{y}_q \|^2 + \tau \sum_{q=1}^{Q} \| \mathbf{a}_q \|_1 + \alpha\, Q(\mathbf{x}) + \sum_{q=1}^{Q} \boldsymbol{\lambda}_q^t(\mathbf{B}_q(\mathbf{s}_q)\mathbf{x} - \mathbf{W}\mathbf{a}_q) + \frac{\beta}{2}\sum_{q=1}^{Q} \| \mathbf{B}_q(\mathbf{s}_q)\mathbf{x} - \mathbf{W}\mathbf{a}_q \|^2, \tag{3.9}$$

where $\mathbf{a} = (\mathbf{a}_1,\ldots,\mathbf{a}_Q)$, $\boldsymbol{\lambda}_q$ are $D\times 1$ Lagrangian multiplier vectors with $\boldsymbol{\lambda} = (\boldsymbol{\lambda}_1,\ldots,\boldsymbol{\lambda}_Q)$, and β is a non-negative parameter. The ADMM leads to the following sequence of iterative unconstrained problems,

$$\mathbf{x}^{k+1} = \arg\min_{\mathbf{x}} L(\mathbf{x},\mathbf{a}^k,\boldsymbol{\lambda}^k), \tag{3.10}$$

$$\mathbf{a}^{k+1} = \arg\min_{\mathbf{a}} L(\mathbf{x}^{k+1},\mathbf{a},\boldsymbol{\lambda}^k) \tag{3.11}$$

$$\boldsymbol{\lambda}_q^{k+1} = \boldsymbol{\lambda}_q^k - \beta[\mathbf{B}_q(\mathbf{s}_q)\mathbf{x}^{k+1} - \mathbf{W}\mathbf{a}_q^{k+1}],\quad q = 1,\ldots,Q, \tag{3.12}$$

where k is the iteration number. Let us now describe the estimation process. The calculation of each $\boldsymbol{\lambda}_q^{k+1}$ is straightforward. The image $\mathbf{x}$ can be estimated by solving the following minimization problem

$$\mathbf{x}^{k+1} = \arg\min_{\mathbf{x}} \left\{ \frac{\beta}{2}\sum_{q} \| \mathbf{B}_q(\mathbf{s}_q)\mathbf{x} - \mathbf{W}\mathbf{a}_q \|^2 + \alpha R(\mathbf{x},\mathbf{V}) + \sum_{q} \boldsymbol{\lambda}_q^{k\,t}(\mathbf{B}_q(\mathbf{s}_q)\mathbf{x} - \mathbf{W}\mathbf{a}_q^k) \right\}. \tag{3.13}$$

This and the optimization step in Equation (3.10) produce the following linear equation for $\mathbf{x}^{k+1}$

$$\mathbf{x}^{k+1} = \left[\beta \sum_{q} \mathbf{B}_q^t(\mathbf{s}_q)\mathbf{B}_q(\mathbf{s}_q) + \alpha p \sum_{d} 2^{1-o(d)}\Delta^{d^t}\boldsymbol{\Lambda}_d^k\Delta^d \right]^{-1} \sum_{q} \mathbf{B}_q(\mathbf{s}_q)^t \left[\beta\mathbf{W}\mathbf{a}_q^k - \lambda_q^k \right] \tag{3.14}$$

We solved Equation (3.14) using the conjugate gradient algorithm. The estimation of the sparse coefficients is described in Section 3.2.

This estimation process has been performed for the Barbara image, and the obtained HR images are shown in Figure 3.2. In Figure 3.2(a) it is shown the first iteration estimate (PSNR=22.8 dB), and in Figure 3.2(b) the last estimate (PSNR=23.9 dB) is shown. The maximum number of iterations was 20. The result obtained at the last iteration is better than the obtained at the first one and this denotes a better performance for the CSSR joint estimation approach than for the sequential one.

The next stage was to adapt a realistic measurement matrix that can be physically synthesized, so we used a Bernoulli measurement matrix. Figure 3.3 shows the results obtained using this new $\boldsymbol{\Phi}$, with a PSNR of 22.7 dB for the first iteration and of 23.9 dB for the last one.

At these stages the motion vectors $\mathbf{s}_q$ were assumed to be known. At the next stage the motion vectors began to be considered unknowns, to be estimated. The quality of the estimated

(a) (b)

Figure 3.2: Joint estimation process. Observations have been simulated using Gaussian Blur of variance 3, zooming factor P=2, Gaussian circulant Toeplitz measurement matrix with compression ratio R=0.8, and additive noise of SNR=40dB. (a) First iteration estimate with PSNR=22.8 dB, (b) last iteration estimate with PSNR=23.9 dB

motion vectors is critical for the HR estimation quality, and many experiments and trials were made to obtain more accurate results. While the trivial update of registration parameters can be obtained by solving

$$\mathbf{s}_q^{k+1} = \arg\min_{\mathbf{s}_q} \| \mathbf{B}_q(\mathbf{s}_q)\mathbf{x}^{k+1} - \mathbf{W}\mathbf{a}_q^{k+1} \|^2 \tag{3.15}$$

However, at that stage, we observed experimentally that a fast and reliable estimation of the registration parameters can be obtained by registering the reconstructed LR images estimated in the previous step with respect to the reference LR observation, rather than registering the previously obtained HR image, see [19]. Thus minimizing

$$\mathbf{s}_q^{k+1} = \arg\min_{\mathbf{s}_q} \| \mathbf{C}(\mathbf{s}_q)[\mathbf{A}\mathbf{H}_r]^t \mathbf{W}\mathbf{a}_r^{k+1} - \left[\mathbf{A}\mathbf{H}_q\right]^t \mathbf{W}\mathbf{a}_q^{k+1} \|^2 \tag{3.16}$$

where r denotes the reference image, usually to be the first one of the LR image sequence.

The next trial was to estimate the warping parameters by registering the up-sampled LR images obtained in the previous step with respect to the obtained HR image, see [20].

$$\mathbf{s}_q^{k+1} = \arg\min_{\mathbf{s}_q} \left[\frac{\beta}{2} \| \mathbf{C}(\mathbf{s}_q)\mathbf{x}^{k+1} - [\mathbf{A}\mathbf{H}_q]^t \mathbf{W}\mathbf{a}_q^{k+1} \|^2 + (\mathbf{s}_q - \mathbf{s}_q^k)^t \boldsymbol{\Xi}_q (\mathbf{s}_q - \mathbf{s}_q^k) \right], \tag{3.17}$$

where $\boldsymbol{\Xi}_q$ is a 3×3 known matrix of regularization parameters. Figure 3.4(a) shows the estimated Barbara image obtained using Equation (3.16), while Figure 3.4(b) shows the result obtained using Equation (3.17). This trial showed that the minimization in Equation (3.16) gives a better performance. In the next section, it will be shown that registration could be performed interchangeably from the estimated HR image or from the estimated LR reference image, in an efficient and accurate manner.

(a) (b)

Figure 3.3: Joint estimation process. Observations have been simulated using Gaussian Blur of variance 3, zooming factor P=2, Bernoulli circulant Toeplitz measurement matrix with compression ratio R=0.8 and additive noise of SNR=40dB. (a) First iteration estimate with PSNR=22.7 dB, (b) last iteration estimate with PSNR=23.9 dB

(a) (b)

Figure 3.4: Joint estimation process with motion estimation . Observations have been simulated using Gaussian Blur of variance 3, zooming factor P=2, Bernoulli circulant Toeplitz measurement matrix with compression ratio R=0.8 and additive noise of SNR=40dB. (a) Estimated image using the minimization in Equation (3.16), (b) estimated image using minimization in Equation (3.17)

The regularization term utilized for HR image estimation took a special importance, and many regularizers have been tested with the proposed framework. The best performance of CSSR was obtained using the robust log-based regularizer introduced in the next section, which we finally used in all the experiments.

3.2 The Proposed CSSR Approach

The constrained optimization in Equation (3.8) can be changed into the following unconstrained optimization using ADMM. The new augmented Lagrangian functional is defined as follows

$$L(\mathbf{x},\mathbf{a},\mathbf{s},\boldsymbol{\lambda}) = \frac{\eta}{2}\sum_{q=1}^{Q} \| \boldsymbol{\Phi}\mathbf{W}\mathbf{a}_q - \mathbf{y}_q \|^2 + \tau \sum_{q=1}^{Q} \| \mathbf{a}_q \|_1 + \alpha\, Q(\mathbf{x}) + \sum_{q=1}^{Q} \boldsymbol{\lambda}_q^t(\mathbf{B}_q(\mathbf{s}_q)\mathbf{x} - \mathbf{W}\mathbf{a}_q) + \frac{\beta}{2}\sum_{q=1}^{Q} \| \mathbf{B}_q(\mathbf{s}_q)\mathbf{x} - \mathbf{W}\mathbf{a}_q \|^2, \tag{3.18}$$

where $\mathbf{s} = (\mathbf{s}_1, \ldots, \mathbf{s}_Q)$ denotes the motion vector set. The HR regularization term $Q(\mathbf{x})$ utilized in this final version of the proposed CSSR algorithm is described next,

$$Q(\mathbf{x}) = \sum_{d\in\Delta}\sum_{i=1}^{N} \log(|\omega_d^{\mathbf{x}}(i)|), \tag{3.19}$$

where $\omega_d^{\mathbf{x}}(i)$ is the i-th pixel of the filtered ω_d^x image and

$$\boldsymbol{\omega}_d^{\mathbf{x}} = \mathbf{F}_d\mathbf{x}, \tag{3.20}$$

where $\mathbf{F}_d$ is a high-pass filter operator, and the index $d \in \Delta$ identifies one of the members of the used filter set. In this work we have used a filter set with elements $\Delta = \{h, v, hv, vh, hh, vv\}$, where h, v represent the first order horizontal and vertical difference filters, hv and vh represent first order differences along diagonals, and hh and vv the horizontal and vertical second order differences. This regularization term favors sparsity of the high-pass filtered images ω_d^x, and corresponds to the Super-Gaussian log prior used in Bayesian blind deconvolution [83].

Since the log function can not be differentiated at zero, we consider in this work the following robust version of the log regularizer

$$\log_\epsilon(|s|) = \begin{cases} \log(|s|) & \text{for } |s| \geq \epsilon \\ \frac{s^2}{2\epsilon^2} - (\frac{1}{2} - \log(\epsilon)) & \text{for } 0 \leq |s| \leq \epsilon \end{cases} \tag{3.21}$$

and replace $Q(\mathbf{x})$ in Equation (3.19) by

$$Q(\mathbf{x}) = \sum_{d\in\Delta}\sum_{i=1}^{N} \log_\epsilon(|\omega_d^{\mathbf{x}}(i)|), \tag{3.22}$$

where we have removed the dependency of $Q(\cdot)$ on ϵ for simplicity.

The augmented Lagrangian functional in Equation (3.18) leads to the following iterative unconstrained sub-problems;

$$\mathbf{x}^{k+1} = \arg\min_{\mathbf{x}} L(\mathbf{x}, \mathbf{a}^k, \mathbf{s}^k, \boldsymbol{\lambda}^k), \tag{3.23}$$

$$\mathbf{a}^{k+1} = \arg\min_{\mathbf{a}} L(\mathbf{x}^{k+1}, \mathbf{a}, \mathbf{s}^k, \boldsymbol{\lambda}^k) \tag{3.24}$$

$$\mathbf{s}^{k+1} = \arg\min_{\mathbf{s}} L(\mathbf{x}^{k+1}, \mathbf{a}^{k+1}, \mathbf{s}, \boldsymbol{\lambda}^k) \tag{3.25}$$

$$\boldsymbol{\lambda}_q^{k+1} = \boldsymbol{\lambda}_q^k - \beta[\mathbf{B}_q(\mathbf{s}_q^{k+1})\mathbf{x}^{k+1} - \mathbf{W}\mathbf{a}_q^{k+1}], \quad q = 1, \ldots, Q, \tag{3.26}$$

where k is the iteration number. Notice that according to the ADMM approach $\mathbf{B}_q(\mathbf{s}_q)$ in Equation (3.18) should not depend on the iteration index, as it is not the case here. However, we have not encountered any convergence problems applying this iterative procedure.

The calculation of the $\boldsymbol{\lambda}_q^{k+1}$ is straightforward again. The estimation process of the other unknowns is described in the coming subsections.

3.2.1 HR Image Estimation

The function $\rho_\epsilon(s) = \log_\epsilon(|s|)$ in Equation (3.22) is symmetric around 0, and $\rho(\sqrt{s})$ is concave and increasing for $s \in [0, \infty)$ [83]. So, it can be represented as (see [88])

$$\rho_\epsilon(s) = \inf_{\xi > 0} \frac{1}{2}\xi s^2 - \rho_\epsilon^*(\frac{1}{2}\xi), \tag{3.27}$$

where $\rho_\epsilon^*(\frac{1}{2}\xi)$ is the concave conjugate function

$$\rho_\epsilon^*(\frac{1}{2}\xi) = \inf_{s > 0} \frac{1}{2}\xi s^2 - \rho_\epsilon(s). \tag{3.28}$$

It is shown in [83] that the infimum in Equation (3.27) is achieved when $\xi = \rho_\epsilon'(s)/s$. Consequently, for the regularization term $Q(\mathbf{x})$ in Equation (3.18), we can write

$$Q(\mathbf{x}) \leq R(\mathbf{x}, \boldsymbol{\xi}) = \frac{1}{2}\sum_{d \in \Delta} \mathbf{x}^t \mathbf{F}_d^t \boldsymbol{\Omega}_d \mathbf{F}_d \mathbf{x} - \sum_{d \in \Delta} \sum_{i=1}^{N} \rho_\epsilon^*(\frac{1}{2}\xi_d(i)) \tag{3.29}$$

where $\boldsymbol{\xi} = (\boldsymbol{\xi}_1, \ldots, \boldsymbol{\xi}_Q)$, $\boldsymbol{\xi}_q = (\xi_q(1), \ldots, \xi_q(N))$ for $q = 1, \ldots, Q$, with all its components positive, and $\boldsymbol{\Omega}_d$ is a diagonal matrix with entries

$$\Omega_d(i, i) = \xi_d(i). \tag{3.30}$$

For a given $\mathbf{x}$, the inequality in Equation (3.29) becomes an equality if (see [83] for details),

$$\xi_d^{\mathbf{x}}(i) = \min(1/|\omega_d^{\mathbf{x}}(i)|^2, 1/\epsilon^2) = \begin{cases} \frac{1}{|\omega_d^{\mathbf{x}}(i)|^2} & \text{for } |\omega_d^{\mathbf{x}}(i)| \geq \epsilon \\ \frac{1}{\epsilon^2} & \text{for } 0 \leq |\omega_d^{\mathbf{x}}(i)| \leq \epsilon \end{cases} \tag{3.31}$$

where $\omega_d^{\mathbf{x}}(i)$ is defined from $\mathbf{x}$ in Equation (3.20). Then we can apply standard Majorization-Minimization methods [89]. Given $\mathbf{x}^k, \mathbf{a}^k, \mathbf{s}^k$ and defining

$$L^k(\mathbf{x}) = \frac{\beta}{2}\sum_q \| \mathbf{B}_q(\mathbf{s}_q^k)\mathbf{x} - \mathbf{W}\mathbf{a}_q^k \|^2 + \sum_q \boldsymbol{\lambda}_q^{k\,t}(\mathbf{B}_q(\mathbf{s}_q^k)\mathbf{x} - \mathbf{W}\mathbf{a}_q^k) \tag{3.32}$$

it can be easily shown that

$$L^k(\mathbf{x}^k) + \alpha Q(\mathbf{x}^k) \geq L^k(\mathbf{x}^{k+1}) + \alpha Q(\mathbf{x}^{k+1}) \tag{3.33}$$

where

$$\mathbf{x}^{k+1} = \arg\min_{\mathbf{x}} \left\{ \frac{\beta}{2} \sum_q \| \mathbf{B}_q(\mathbf{s}_q^k)\mathbf{x} - \mathbf{W}\mathbf{a}_q \|^2 + \alpha R(\mathbf{x}, \xi^{\mathbf{x}^k}) + \sum_q \boldsymbol{\lambda}_q^{k\,t} (\mathbf{B}_q(\mathbf{s}_q^k)\mathbf{x} - \mathbf{W}\mathbf{a}_q^k) \right\}. \tag{3.34}$$

From Equation (3.34), the optimization step in Equation (3.23) produces the following linear equation for $\mathbf{x}^{k+1}$

$$\mathbf{x}^{k+1} = \left[\beta \sum_q \mathbf{B}^{k\,t}{}_q(\mathbf{s}_q^k)\mathbf{B}_q^k(\mathbf{s}_q^k) + \alpha \sum_{d \in \Delta} \mathbf{F}_d^t \boldsymbol{\Omega}_d^k \mathbf{F}_d \right]^{-1} \sum_q \mathbf{B}_q^k(\mathbf{s}_q^k)^t \left[\beta \mathbf{W}\mathbf{a}_q^k - \lambda_q^k \right] \tag{3.35}$$

where

$$\Omega_d^k(i,i) = \min(1/|\omega_d^{\mathbf{x}^k}(i)|^2, 1/\epsilon^2). \tag{3.36}$$

3.2.2 Transformed Coefficient Estimation

The optimization step in Equation (3.24) for each $\mathbf{a}_q$ produces

$$\begin{aligned} \mathbf{a}_q^{k+1} \quad &= \arg\min_{\mathbf{a}_q} \left\{ \frac{\eta}{2} \| \boldsymbol{\Phi}\mathbf{W}\mathbf{a}_q - \mathbf{y}_q \|^2 + \tau \| \mathbf{a}_q \|_1 \right. \\ &\quad \left. + \frac{\beta}{2} \| \mathbf{B}_q^k(\mathbf{s}_q^k)\mathbf{x}^{k+1} - \mathbf{W}\mathbf{a}_q \|^2 - \boldsymbol{\lambda}_q^{k\,t} (\mathbf{B}_q^k(\mathbf{s}_q^k)\mathbf{x}^{k+1} - \mathbf{W}\mathbf{a}_q) \right\} \end{aligned} \tag{3.37}$$

which is equivalent to

$$\mathbf{a}_q^{k+1} = \arg\min_{\mathbf{a}_q} \left\{ \frac{\eta}{2} \| \boldsymbol{\Phi}\mathbf{W}\mathbf{a}_q - \mathbf{y}_q \|^2 + \frac{\beta}{2} \| \mathbf{B}_q^k(\mathbf{s}_q^k)\mathbf{x}^{k+1} - \lambda_q^k - \mathbf{W}\mathbf{a}_q \|^2 + \tau \| \mathbf{a}_q \|_1 \right\}. \tag{3.38}$$

The above equation can be rewritten as

$$\mathbf{a}_q^{k+1} = \arg\min_{\mathbf{a}_q} \| \boldsymbol{\Phi}'\mathbf{W}\mathbf{a}_q - \mathbf{J}' \|^2 + \tau \| \mathbf{a}_q \|_1, \tag{3.39}$$

where

$$\mathbf{J}' = \begin{bmatrix} \sqrt{\frac{\eta}{2}}\mathbf{y}_q \\ \sqrt{\frac{\beta}{2}}(\mathbf{B}_q^k(\mathbf{s}_q^k)\mathbf{x}^{k+1} - \lambda_q^k) \end{bmatrix} \text{ and } \boldsymbol{\Phi}' = \begin{bmatrix} \sqrt{\frac{\eta}{2}}\boldsymbol{\Phi} \\ \sqrt{\frac{\beta}{2}}\mathbf{I} \end{bmatrix} \tag{3.40}$$

with $\mathbf{I}$ the $D \times D$ identity matrix. The optimization problem in Equation 3.39 can be solved using the algorithm in [82].

3.2.3 Registration from Estimated HR Image

To estimate the registration parameters in Equation (3.25), we solve

$$\mathbf{s}_q^{k+1} = \arg\min_{\mathbf{s}_q} \frac{\beta'}{2} \parallel \mathbf{B}_q(\mathbf{s}_q)\mathbf{x}^{k+1} - \mathbf{W}\mathbf{a}_q^{k+1} \parallel^2, \tag{3.41}$$

where β' is a positive parameter. Notice that we could use regularization on the parameters to be estimated as we did in [20]. However, we have observed that regularization was not needed for the performed experiments. $\mathbf{B}_q(\mathbf{s}_q)\mathbf{x}$, can be approximated by expanding it into its first-order Taylor series around the previous value $\mathbf{s}_q^k$. Hence obtaining (see [30, 37])

$$\begin{aligned}\mathbf{B}_q(\mathbf{s}_q)\mathbf{x}^{k+1} \approx\ & \mathbf{B}_q(\mathbf{s}_q^k)\mathbf{x}^{k+1} \\ & + \left[\mathbf{O}_{q1}(\mathbf{s}_q^k)\mathbf{x}^{k+1}, \mathbf{O}_{q2}(\mathbf{s}_q^k)\mathbf{x}^{k+1}, \mathbf{O}_{q3}(\mathbf{s}_q^k)\mathbf{x}^{k+1}\right](\mathbf{s}_q - \mathbf{s}_q^k),\end{aligned} \tag{3.42}$$

where $\mathbf{O}_{qi}(\mathbf{s}_q^k)\mathbf{x}^{k+1} = \mathbf{A}\mathbf{H}_q\mathbf{N}_i(\mathbf{s}_q^k)\mathbf{x}^{k+1}$, and $\mathbf{N}_i(\mathbf{s}_q^k)\mathbf{x}^{k+1}$ is defined as

$$\begin{aligned}&\left[\mathbf{N}_1(\mathbf{s}_q^k)\mathbf{x}^{k+1}, \mathbf{N}_2(\mathbf{s}_q^k)\mathbf{x}^{k+1}, \mathbf{N}_3(\mathbf{s}_q^k)\mathbf{x}^{k+1}\right] = \\ &\left[(\mathbf{P}_1(\mathbf{s}_q^k)\mathbf{M}_1(\mathbf{s}_q^k) + \mathbf{P}_2(\mathbf{s}_q^k)\mathbf{M}_2(\mathbf{s}_q^k), \mathbf{M}_1(\mathbf{s}_q^k), \mathbf{M}_2(\mathbf{s}_q^k)\right].\end{aligned} \tag{3.43}$$

In Equation (3.43)

$$\mathbf{M}_1(\mathbf{s}_q^k) = (\mathbf{I} - \mathbf{D}_{\mathbf{b}_q(\mathbf{s}_q)})(\mathbf{L}_{tr(\mathbf{s}_q)} - \mathbf{L}_{tl(\mathbf{s}_q)}) + \mathbf{D}_{\mathbf{b}_q(\mathbf{s}_q)}(\mathbf{L}_{br(\mathbf{s}_q)} - \mathbf{L}_{bl(\mathbf{s}_q)}) \tag{3.44}$$

$$\mathbf{M}_2(\mathbf{s}_q^k) = (\mathbf{I} - \mathbf{D}_{\mathbf{a}_q(\mathbf{s}_q)})(\mathbf{L}_{bl(\mathbf{s}_q)} - \mathbf{L}_{tl(\mathbf{s}_q)}) + \mathbf{D}_{\mathbf{a}_q(\mathbf{s}_q)}(\mathbf{L}_{br(\mathbf{s}_q)} - \mathbf{L}_{tr(\mathbf{s}_q)}) \tag{3.45}$$

$$\mathbf{P}_1(\mathbf{s}_q^k) = -[\mathbf{D}_{\mathbf{u}}\sin(\theta_q^k) + \mathbf{D}_{\mathbf{v}}\cos(\theta_q^k)] \tag{3.46}$$

$$\mathbf{P}_2(\mathbf{s}_q^k) = [\mathbf{D}_{\mathbf{u}}\cos(\theta_q^k) - \mathbf{D}_{\mathbf{v}}\sin(\theta_q^k)]. \tag{3.47}$$

and $\mathbf{D}_{\mathbf{u}}$ and $\mathbf{D}_{\mathbf{v}}$ are diagonal matrices whose diagonals respectively are the vectors $\mathbf{u}$ and $\mathbf{v}$, representing pixel coordinates in $\mathbf{x}$. Substituting Equation (3.42) into Equation (3.41), we obtain the following update equation

$$\mathbf{s}_q^{k+1} = \left[\mathbf{\Lambda}_q^k\right]^{-1}(\mathbf{\Upsilon}_q^k + \mathbf{\Lambda}_q^k\mathbf{s}_q^k) = \mathbf{s}_q^k + \left[\mathbf{\Lambda}_q^k\right]^{-1}\mathbf{\Upsilon}_q^k, \tag{3.48}$$

where $\mathbf{\Lambda}_q^k$ and $\mathbf{\Upsilon}_q^k$ correspond to the $q-$th observation at the $k-$th iteration with respectively $(i,j) \in \{1,2,3\}$ element and $i \in \{1,2,3\}$ element given by

$$\mathbf{\Lambda}_{qij}^k = \left[\mathbf{A}\mathbf{H}_q\mathbf{N}_i(\mathbf{s}_q^k)\mathbf{x}^{k+1}\right]^t \mathbf{A}\mathbf{H}_q\mathbf{N}_j(\mathbf{s}_q^k)\mathbf{x}^{k+1}, \tag{3.49}$$

$$\mathbf{\Upsilon}_{qi}^k = \left[\mathbf{A}\mathbf{H}_q\mathbf{N}_i(\mathbf{s}_q^k)\mathbf{x}^{k+1}\right]^t (\mathbf{W}\mathbf{a}_q^{k+1} - \mathbf{A}\mathbf{H}_q\mathbf{N}_i(\mathbf{s}_q^k)\mathbf{x}^{k+1}). \tag{3.50}$$

where $\mathbf{N}_i$ were defined in Equation (3.43).

Utilizing the estimated $\mathbf{s}_q^{k+1}$, the warping matrix can be calculated by the explicit form presented in Equation (2.32)

3.2.4 Registration from Estimated LR Reference Image

In Chapter 4 the registration estimation procedure using Equation (3.41) will be compared with registration using the following equation,

$$\mathbf{s}_{Lq}^{k+1} = \arg\min_{\mathbf{s}_{Lq}} \frac{\beta'}{2} \parallel \mathbf{C}'(\mathbf{s}_{Lq})\mathbf{z}_r^{k+1} - \mathbf{z}_q^{k+1} \parallel^2 . \tag{3.51}$$

where $\mathbf{C}'(\mathbf{s}_{Lq})$ is a $D \times D$ warping matrix, $\mathbf{z}_r^{k+1} = \mathbf{W}\mathbf{a}_r^{k+1}$ is the LR image used for registration (reference image), and $\mathbf{z}_q^{k+1} = \mathbf{W}\mathbf{a}_q^{k+1}$ is the q–th LR observation, obtained in the previous step of the iterative process.

Notice that the warped LR observation $\mathbf{C}'(\mathbf{s}_{Lq})\mathbf{z}_r$ is equivalent to the LR version of $\mathbf{C}_q(\mathbf{s}_q)\mathbf{x}$. $\mathbf{C}'(\mathbf{s}_{Lq})$ can be approximated by expanding it into its first-order Taylor series around the previous value $\mathbf{s}_{Lq}^k$, hence obtaining (see [18, 30, 37])

$$\begin{aligned}\mathbf{C}'(\mathbf{s}_{Lq})\mathbf{z}_r^{k+1} \approx\ & \mathbf{C}'(\mathbf{s}_{Lq}^k)\mathbf{z}_r^{k+1} \\ & + \left[\mathbf{N}_{q1}(\mathbf{s}_{Lq}^k)\mathbf{z}_r^{k+1}, \mathbf{N}_{q2}(\mathbf{s}_{Lq}^k)\mathbf{z}_r^{k+1}, \mathbf{N}_{q3}(\mathbf{s}_{Lq}^k)\mathbf{z}_r^{k+1}\right](\mathbf{s}_{Lq} - \mathbf{s}_{Lq}^k),\end{aligned} \tag{3.52}$$

where $\mathbf{N}_i(\mathbf{s}_{Lq}^k)\mathbf{z}_r^{k+1}$ is defined as

$$\begin{aligned}&\left[\mathbf{N}_1(\mathbf{s}_{Lq}^k)\mathbf{z}_r^{k+1}, \mathbf{N}_2(\mathbf{s}_{Lq}^k)\mathbf{z}_r^{k+1}, \mathbf{N}_3(\mathbf{s}_{Lq}^k)\mathbf{z}_r^{k+1}\right] \\ &\quad = \left[(\mathbf{P}_1(\mathbf{s}_{Lq}^k)\mathbf{M}_1(\mathbf{s}_{Lq}^k) + \mathbf{P}_2(\mathbf{s}_{Lq}^k)\mathbf{M}_2(\mathbf{s}_{Lq}^k), \mathbf{M}_1(\mathbf{s}_{Lq}^k), \mathbf{M}_2(\mathbf{s}_{Lq}^k)\right],\end{aligned} \tag{3.53}$$

with

$$\mathbf{M}_1(\mathbf{s}_{Lq}^k) = (\mathbf{I} - \mathbf{D}_{\mathbf{b}_q(\mathbf{s}_{Lq})})(\mathbf{L}_{tr(\mathbf{s}_{Lq})} - \mathbf{L}_{tl(\mathbf{s}_{Lq})}) + \mathbf{D}_{\mathbf{b}_q(\mathbf{s}_{Lq})}(\mathbf{L}_{br(\mathbf{s}_{Lq})} - \mathbf{L}_{bl(\mathbf{s}_{Lq})}) \tag{3.54}$$

$$\mathbf{M}_2(\mathbf{s}_{Lq}^k) = (\mathbf{I} - \mathbf{D}_{\mathbf{a}_q(\mathbf{s}_{Lq})})(\mathbf{L}_{bl(\mathbf{s}_{Lq})} - \mathbf{L}_{tl(\mathbf{s}_{Lq})}) + \mathbf{D}_{\mathbf{a}_q(\mathbf{s}_{Lq})}(\mathbf{L}_{br(\mathbf{s}_{Lq})} - \mathbf{L}_{tr(\mathbf{s}_{Lq})}) \tag{3.55}$$

$$\mathbf{P}_1(\mathbf{s}_{Lq}^k) = -[\mathbf{D}_{\mathbf{u}} \sin(\theta_q^k) + \mathbf{D}_{\mathbf{v}} \cos(\theta_q^k)] \tag{3.56}$$

$$\mathbf{P}_2(\mathbf{s}_{Lq}^k) = [\mathbf{D}_{\mathbf{u}} \cos(\theta_q^k) - \mathbf{D}_{\mathbf{v}} \sin(\theta_q^k), \tag{3.57}$$

where $\mathbf{D}_{\mathbf{u}}$ and $\mathbf{D}_{\mathbf{v}}$ are diagonal matrices whose diagonals respectively are the vectors $\mathbf{u}$ and $\mathbf{v}$ representing pixel coordinates in $\mathbf{z}_r$. Matrices L_κ with $\kappa \in \{bl(\mathbf{s}_{Lq}), br(\mathbf{s}_{Lq}), tl(\mathbf{s}_{Lq}), tr(\mathbf{s}_{Lq})\}$ are constructed in such a way that the product $L_\kappa \mathbf{z}_r$ produces respectively pixels at the bottom-left, bottom-right, top-left, and top-right, pixel locations in $\mathbf{z}_r$. Substituting Equation (3.52) into Equation (3.51), we obtain the following final update equation

$$\mathbf{s}_{Lq}^{k+1} = \mathbf{s}_{Lq}^k + \left[\mathbf{\Lambda}_{Lq}^k\right]^{-1} \Upsilon_{Lq}^k, \tag{3.58}$$

where $\mathbf{\Lambda}_{Lq}^k$ and Υ_{Lq}^k correspond to the q–th observation at the k–th iteration with respectively $(i, j) \in \{1, 2, 3\}$ element and $i \in \{1, 2, 3\}$ element given by

$$\Lambda_{Lqij}^k = \left[\mathbf{N}_i(\mathbf{s}_{Lq}^k)\mathbf{z}_r^{k+1}\right]^t \mathbf{N}_j(\mathbf{s}_{Lq}^k)\mathbf{z}_r^{k+1}, \tag{3.59}$$

$$\Upsilon_{Lqi}^k = \left[\mathbf{N}_i(\mathbf{s}_{Lq}^k)\mathbf{z}_r^{k+1}\right]^t (\mathbf{z}_q^{k+1} - \mathbf{N}_i(\mathbf{s}_{Lq}^k)\mathbf{z}_r^{k+1}). \tag{3.60}$$

Algorithm 1 Compressive Sensing Super Resolution (CSSR) Algorithm

Require: Values α, β, τ, η
Initialize $\mathbf{a}^0$, $\mathbf{s}^0$, $\boldsymbol{\lambda}^0$, $\boldsymbol{\Omega}^0 = \{\boldsymbol{\Omega}_d^0, d \in \Delta\}$
$k = 0$
while convergence criterion is not met **do**
1. Calculate $\mathbf{x}^{k+1}$ by solving Equation (3.35)
2. For $d \in \Delta$, calculate $\boldsymbol{\Omega}_d^{k+1}$ using Equation (3.36)
3. For $q = 1, \ldots, Q$, calculate $\mathbf{a}_q^{k+1}$ using Equation (3.39)
4. For $q = 1, \ldots, Q$, calculate $\mathbf{s}_q^{k+1}$ using one of Equations (3.48) or (3.61)
5. For $q = 1, \ldots, Q$, update $\boldsymbol{\lambda}_q^{k+1}$ using Equation (3.26)
6. Set $k = k + 1$
end while
return $\mathbf{x} = \mathbf{x}^k$

If $\mathbf{s}_{Lq}^{k+1} = [\theta_{Lq}, c_{Lq}, d_{Lq}]^t$ then the HR motion vector is

$$\mathbf{s}_q^{k+1} = [\theta_{Lq}, P \cdot c_{Lq}, P \cdot d_{Lq}]^t. \tag{3.61}$$

After estimating $\mathbf{s}_q^{k+1}$, then the warping matrix can be obtained as in Equation (2.32).

3.2.5 CSSR Algorithm Statement

The complete CSSR algorithm is presented in Algorithm 1. Notice here the two possible registration procedures from the HR image using Equation (3.48) and from the LR reference image using Equation (3.61).

3.3 Proposed Color CSSR (CCSSR)

In this section we propose a Color Compressed Sensing Super Resolution (CCSSR) algorithm. Firstly we present the modeling and problem formulation and finally the proposed algorithm.

3.3.1 Modeling and Problem Formulation

Let us assume that we have access to a set of Q CS LR RGB color images of the form

$$\mathbf{y}_{cq} = \boldsymbol{\Phi}_c \mathbf{A} \mathbf{H}_q \mathbf{C}(\mathbf{s}_q) \mathbf{x}_c + \mathbf{n}_{cq} = \boldsymbol{\Phi}_c \mathbf{B}_q(\mathbf{s}_q) \mathbf{x}_c + \mathbf{n}_{cq}, \text{ for } q = 1, \ldots, Q, \tag{3.62}$$

where $c \in \{R, G, B\}$ denotes one of the three channels, $\mathbf{y}_{cq}$ is an $M \times 1$ vector representing the c channel of the q-th CS-LR observation, $\boldsymbol{\Phi}_c$ is the CS $M \times D$ measurement matrix corresponding to the c channel. The down-sampling matrix $\mathbf{A}$ is a $D \times N$ matrix, $D \leq N$, where $N = \mathrm{P}^2 D$ and $\mathrm{P} \geq 1$ is the zooming factor, in each dimension of the image. $\mathbf{H}_q$ is an $N \times N$ blurring matrix, which is assumed to be known. $\mathbf{C}(\mathbf{s}_q)$ is the $N \times N$ warping matrix for motion vector

$\mathbf{s}_q = [\theta_q, c_q, d_q]^t$, where θ_q is the rotation angle, and c_q and d_q are, respectively, the horizontal and vertical translations of the q-th LR image with respect to the reference frame, $\mathbf{x}_c$ is an $N \times 1$ vector representing the c HR channel we want to estimate, and $\mathbf{n}_{cq}$ models the noise associated with the corresponding observation. We write $\mathbf{B}_q(\mathbf{s}_q) = \mathbf{A}\mathbf{H}_q\mathbf{C}(\mathbf{s}_q)$ for simplicity. We denote by R the compression factor of the measurement system, that is R= M/D, R≤ 1.

We assume in this work that the LR images are sparse in a transformed domain. That is, $\mathbf{A}\mathbf{H}_q\mathbf{C}(\mathbf{s}_q)\mathbf{x}_c = \mathbf{W}\mathbf{a}_{cq}$, where $\mathbf{W}$ is a $D \times D$ transformation (wavelet) matrix, $\mathbf{a}_{cq}$ is the $D \times 1$ LR transformed coefficient vector corresponding to the c channel of the $q-$th observation. We assume that the $\mathbf{a}_{cq}$ vectors are sparse and then (see [18]) we can recover them by solving

$$\begin{aligned} &\min \sum_{c\in\{R,G,B\}} L(\mathbf{x}_c, \mathbf{a}_c) \\ &\text{s.t.} \quad \mathbf{B}_q(\mathbf{s}_q)\mathbf{x}_c = \mathbf{W}\mathbf{a}_{cq}, \text{ for } q = 1,\ldots,Q \text{ and } c \in \{R,G,B\}, \end{aligned} \tag{3.63}$$

where

$$L(\mathbf{x}_c, \mathbf{a}_c) = \frac{\eta}{2}\sum_{q=1}^{Q} \| \mathbf{\Phi}\mathbf{W}\mathbf{a}_c - \mathbf{y}_{cq} \|^2 + \tau \sum_{q=1}^{Q} \| \mathbf{a}_{cq} \|_1 + \alpha\, \mathbf{Q}(\mathbf{x}_c), \tag{3.64}$$

with $\mathbf{a}_c = (\mathbf{a}_{c1},\ldots,\mathbf{a}_{cQ})$, η, τ and α positive parameters, $\mathbf{Q}(\mathbf{x}_c)$ a regularization term which will be described soon, $\| . \|$ the Euclidean norm, and $\| . \|_1$ the $\ell 1$ norm.

3.3.2 CCSSR Optimization Approach

Next we describe the optimization approach to the CCSSR problem. To convert the constrained optimization problem in Equation (3.63) into an unconstrained one utilizing ADMM, we define the following augmented Lagrangian functionals

$$L(\mathbf{x}, \mathbf{a}, \mathbf{s}, \boldsymbol{\lambda}) = \sum_{c\in\{R,G,B\}} L_c(\mathbf{x}_c, \mathbf{a}_c, \mathbf{s}, \boldsymbol{\lambda}_c), \tag{3.65}$$

where

$$\begin{aligned} L_c(\mathbf{x}_c, \mathbf{a}_c, \mathbf{s}, \boldsymbol{\lambda}_c) = L(\mathbf{x}_c, \mathbf{a}_c) &+ \sum_{q=1}^{Q} \boldsymbol{\lambda}_{cq}^t(\mathbf{B}_q(\mathbf{s}_q)\mathbf{x}_c - \mathbf{W}\mathbf{a}_{cq}) \\ &+ \frac{\beta}{2}\sum_{q=1}^{Q} \| \mathbf{B}_q(\mathbf{s}_q)\mathbf{x}_c - \mathbf{W}\mathbf{a}_{cq} \|^2, \end{aligned} \tag{3.66}$$

and $L(\mathbf{x}_c, \mathbf{a}_c)$ has been defined in Equation (3.64), $\mathbf{s} = (\mathbf{s}_1,\ldots,\mathbf{s}_Q)$ is the set of motion vectors, $\boldsymbol{\lambda}_c = (\boldsymbol{\lambda}_{c1},\ldots,\boldsymbol{\lambda}_{cQ})$ is the set of $D \times 1$ Lagrangian multiplier vectors $\boldsymbol{\lambda}_{cq}$, and β is a positive parameter. The ADMM leads to the following sequence of iterative unconstrained problems,

$$\mathbf{x}_c^{k+1} = \arg\min_{\mathbf{x}_c} L_c(\mathbf{x}_c, \mathbf{a}_c^k, \mathbf{s}^k, \boldsymbol{\lambda}_c^k), \tag{3.67}$$

$$\mathbf{a}_c^{k+1} = \arg\min_{\mathbf{a}_c} L_c(\mathbf{x}_c^{k+1}, \mathbf{a}_c, \mathbf{s}^k, \boldsymbol{\lambda}_c^k) \tag{3.68}$$

$$\mathbf{s}^{k+1} = \arg\min_{\mathbf{s}} \sum_{c\in\{R,G,B\}} L_c(\mathbf{x}_c^{k+1}, \mathbf{a}_c^{k+1}, \mathbf{s}, \boldsymbol{\lambda}_c^k) \tag{3.69}$$

$$\boldsymbol{\lambda}_{cq}^{k+1} = \boldsymbol{\lambda}_{cq}^k - \beta[\mathbf{B}_q(\mathbf{s}_q^{k+1})\mathbf{x}_c^{k+1} - \mathbf{W}\mathbf{a}_{cq}^{k+1}], \quad q = 1,\ldots,Q, \tag{3.70}$$

where k is the iteration index. Notice that according to the ADMM formulation, $\mathbf{B}_q(\mathbf{s}_q)$ in Equation (3.63) should not depend on the iteration index, as is not the case here. However, we have not encountered any convergence issues with this iterative procedure.

The regularization term $\mathbf{Q}(\mathbf{x}_c)$ is given by

$$\mathbf{Q}(\mathbf{x}_c) = \sum_{d\in\Delta}\sum_{i=1}^{N} \log_\epsilon(|\omega_d^{\mathbf{x}_c}(i)|), \tag{3.71}$$

which replaces $\log|\omega_d^{\mathbf{x}_c}(i)|$ by its robust version

$$\log_\epsilon(|\omega_d^{\mathbf{x}_c}(i)|) = \begin{cases} \log(|\omega_d^{\mathbf{x}_c}(i)|), & \text{for } |\omega_d^{\mathbf{x}_c}(i)| \geq \epsilon \\ \frac{|\omega_d^{\mathbf{x}_c}(i)|^2}{2\epsilon^2} - (\frac{1}{2} - \log(\epsilon)), & \text{for } 0 \leq |\omega_d^{\mathbf{x}_c}(i)| \leq \epsilon \end{cases} \tag{3.72}$$

to avoid the singularity at zero. $\omega_d^{\mathbf{x}_c}(i)$ is the i-th pixel of the filtered channel, that is,

$$\boldsymbol{\omega}_d^{\mathbf{x}_c} = \mathbf{F}_d\mathbf{x}_c\,, \tag{3.73}$$

where $\mathbf{F}_d$ is a high-pass filter operator, and the index $d \in \Delta$ denotes one of the filters in Δ. In this dissertation we have used $\Delta = \{h, v, hv, vh, hh, vv\}$, where h, v represent the first order horizontal and vertical difference filters, hv and vh the first order differences along diagonals, and hh and vv the horizontal and vertical second order differences.

For the regularization term $\mathbf{Q}(\mathbf{x}_c)$ in Equation (3.71), we can write

$$\mathbf{Q}(\mathbf{x}_c) \leq R(\mathbf{x}_c, \boldsymbol{\xi}_c) = \frac{1}{2}\sum_{d\in\Delta} \mathbf{x}_c^t\mathbf{F}_d^t\boldsymbol{\Omega}_d\mathbf{F}_d\mathbf{x}_c - \sum_{d\in\Delta}\sum_{i=1}^{N} \rho_\epsilon^*(\frac{1}{2}\xi_{cd}(i)) \tag{3.74}$$

where $\boldsymbol{\xi} = (\boldsymbol{\xi}_{c1}, \ldots, \boldsymbol{\xi}_{cQ})$, $\boldsymbol{\xi}_{cq} = (\xi_{cq}(1), \ldots, \xi_{cq}(N))$ for $q = 1, \ldots, Q$, with all its components positive, $\boldsymbol{\Omega}_d$ is a diagonal matrix with entries

$$\Omega_{cd}(i,i) = \xi_{cd}(i). \tag{3.75}$$

For a given $\mathbf{x}_c$, the inequality in Equation (3.74) becomes an equality if $\rho_\epsilon^*(\frac{1}{2}\xi_{cd}(i))$ is defined by(see [83] for details),

$$\xi_{cd}^{\mathbf{x}_c}(i) = \min(\frac{1}{|\omega_d^{\mathbf{x}_c}(i)|^2}, \frac{1}{\epsilon^2}) = \begin{cases} \frac{1}{|\omega_d^{\mathbf{x}_c}(i)|^2}, & \text{for } |\omega_d^{\mathbf{x}_c}(i)| \geq \epsilon \\ \frac{1}{\epsilon^2}, & \text{for } 0 \leq |\omega_d^{\mathbf{x}_c}(i)| \leq \epsilon \end{cases} \tag{3.76}$$

where $\omega_d^{\mathbf{x}_c}(i)$ is defined from $\mathbf{x}_c$ in Equation (3.73). Then we can apply a standard Majorization-Minimization method [89]. Given $\mathbf{x}_c^k, \mathbf{a}_c^k, \mathbf{s}^k$ and defining

$$L_c^k(\mathbf{x}_c) = \frac{\beta}{2}\sum_q \| \mathbf{B}_q(\mathbf{s}_q^k)\mathbf{x}_c - \mathbf{W}\mathbf{a}_{cq}^k \|^2 + \sum_q \boldsymbol{\lambda}_{cq}^{k\,t}(\mathbf{B}_q(\mathbf{s}_q^k)\mathbf{x}_c - \mathbf{W}\mathbf{a}_{cq}^k) \tag{3.77}$$

it can be easily shown that

$$L_c^k(\mathbf{x}_c^k) + \alpha\mathbf{Q}(\mathbf{x}_c^k) \geq L_c^k(\mathbf{x}_c^{k+1}) + \alpha\mathbf{Q}(\mathbf{x}_c^{k+1}) \tag{3.78}$$

where

$$\mathbf{x}_c^{k+1} = \arg\min_{\mathbf{x}_c} \left\{ \frac{\beta}{2} \sum_q \| \mathbf{B}_q(\mathbf{s}_q^k)\mathbf{x}_c - \mathbf{W}\mathbf{a}_{cq} \|^2 + \alpha R(\mathbf{x}_c, \boldsymbol{\xi}_c^{\mathbf{x}_c^k}) + \sum_q \boldsymbol{\lambda}_{cq}^{k\ t}(\mathbf{B}_q(\mathbf{s}_q^k)\mathbf{x}_c - \mathbf{W}\mathbf{a}_{cq}^k) \right\}. \tag{3.79}$$

From Equation (3.79), the optimization step in Equation (3.67) produces the following solution for $\mathbf{x}_c^{k+1}$

$$\mathbf{x}_c^{k+1} = \left[\beta \sum_q \mathbf{B}^{k\,t}_q(\mathbf{s}_q^k)\mathbf{B}_q^k(\mathbf{s}_q^k) + \alpha \sum_{d\in\Delta} \mathbf{F}_d^t \boldsymbol{\Omega}_{cd}^k \mathbf{F}_d \right]^{-1} \times \sum_q \mathbf{B}_q^k(\mathbf{s}_q^k)^t \left[\beta \mathbf{W}\mathbf{a}_{cq}^k - \lambda_{cq}^k \right] \tag{3.80}$$

where

$$\Omega_{cd}^k(i,i) = \min(1/|\omega_d^{\mathbf{x}_c^k}(i)|^2, 1/\epsilon^2). \tag{3.81}$$

The optimization step in Equation (3.68) for each $\mathbf{a}_{cq}$ produces

$$\mathbf{a}_{cq}^{k+1} = \arg\min_{\mathbf{a}_{cq}} \left\{ \frac{\eta}{2} \| \boldsymbol{\Phi}\mathbf{W}\mathbf{a}_{cq} - \mathbf{y}_{cq} \|^2 + \tau \| \mathbf{a}_{cq} \|_1 + \frac{\beta}{2} \| \mathbf{B}_q^k(\mathbf{s}_q^k)\mathbf{x}_c^{k+1} - \mathbf{W}\mathbf{a}_{cq} \|^2 - \boldsymbol{\lambda}_{cq}^{k\ t}(\mathbf{B}_q^k(\mathbf{s}_q^k)\mathbf{x}_c - \mathbf{W}\mathbf{a}_{cq}) \right\} \tag{3.82}$$

which is equivalent to

$$\mathbf{a}_{cq}^{k+1} = \arg\min_{\mathbf{a}_{cq}} \left\{ \frac{\eta}{2} \| \boldsymbol{\Phi}\mathbf{W}\mathbf{a}_{cq} - \mathbf{y}_{cq} \|^2 + \frac{\beta}{2} \| \mathbf{B}_q^k(\mathbf{s}_q^k)\mathbf{x}_c^{k+1} - \boldsymbol{\lambda}_{cq}^k - \mathbf{W}\mathbf{a}_{cq} \|^2 + \tau \| \mathbf{a}_{cq} \|_1 \right\}. \tag{3.83}$$

The above equation can be rewritten as

$$\mathbf{a}_{cq}^{k+1} = \arg\min_{\mathbf{a}_{cq}} \| \boldsymbol{\Phi}_c'\mathbf{W}\mathbf{a}_{cq} - \mathbf{J}_c' \|^2 + \tau \| \mathbf{a}_{cq} \|_1, \tag{3.84}$$

where

$$\mathbf{J}_c' = \begin{bmatrix} \sqrt{\frac{\eta}{2}}\mathbf{y}_{cq} \\ \sqrt{\frac{\beta}{2}}(\mathbf{B}_q^k(\mathbf{s}_q^k)\mathbf{x}_c^{k+1} - \boldsymbol{\lambda}_{cq}^k) \end{bmatrix} \quad \text{and} \quad \boldsymbol{\Phi}_c' = \begin{bmatrix} \sqrt{\frac{\eta}{2}}\boldsymbol{\Phi}_c \\ \sqrt{\frac{\beta}{2}}\mathbf{I} \end{bmatrix} \tag{3.85}$$

with $\mathbf{I}$ the $D \times D$ identity matrix. The above optimization problem can be solved using the algorithm in [82].

To estimate the registration parameters from the estimated HR image, the following equation is solved

$$\mathbf{s}_q^{k+1} = \arg\min_{\mathbf{s}_q} \frac{\beta'}{2} \| \mathbf{B}_q(\mathbf{s}_q)\mathbf{Z}^{k+1} - \mathbf{z}_q^{k+1} \|^2. \tag{3.86}$$

where β' is a positive parameter, $\mathbf{Z} = Y(\mathbf{x})$ and $\mathbf{z}_q = Y(\mathbf{W}\mathbf{a}_q)$ represent respectively the HR and LR q-th images, and $Y(\mathbf{x})$ is calculated using

$$Y(\mathbf{x}) = 0.2989\,\mathbf{x}_R + 0.5870\,\mathbf{x}_G + 0.1140\,\mathbf{x}_B, \tag{3.87}$$

where $\mathbf{x}_R, \mathbf{x}_G$, and $\mathbf{x}_B$ are the R, G, and B channels of $\mathbf{x}$. Once $\mathbf{\Lambda}_q^k$ and Υ_q^k are calculated by analogy to Equations (3.49) and (3.50) and using $\mathbf{Z}$ instead of $\mathbf{x}$, the registration parameters can be calculated using Equation (3.48).

To estimate the registration parameters from the reference LR image, we solve the following minimzation

$$\mathbf{s}_{Lq}^{k+1} = \arg\min_{\mathbf{s}_{Lq}} \frac{\beta'}{2} \parallel \mathbf{C}'(\mathbf{s}_{Lq})\mathbf{z}_r^{k+1} - \mathbf{z}_q^{k+1} \parallel^2 . \tag{3.88}$$

where $\mathbf{C}'(\mathbf{s}_{Lq})$ is a $D \times D$ warping matrix, $\mathbf{z} = Y(\mathbf{W}\mathbf{a})$, and the index r represents the LR reference image. Once $\mathbf{\Lambda}_{Lq}^k$ and Υ_{Lq}^k are calculated, see Equations (3.59) and (3.60), the update equation is obtained using Equation (3.61).

3.3.3 CCSSR Algorithm Statement

The complete CCSSR algorithm is presented in Algorithm 2. Notice that the registration can be estimated either from the HR image or from the LR reference image.

Algorithm 2 CCSSR Algorithm Statement.

Require: Values α, β, τ, η
  Initialize $\mathbf{a}^0$, $\mathbf{s}^0$, $\boldsymbol{\lambda}^0$, $\mathbf{\Omega}^0 = \{\mathbf{\Omega}_d^0, d \in \Delta\}$
  $k = 0$
  while convergence criterion is not met **do**
    1. for $c \in \{R, G, B\}$
      i Calculate $\mathbf{x}_c^{k+1}$ by solving Equation (3.80)
      ii For $d \in \Delta$, calculate $\mathbf{\Omega}_{cd}^{k+1}$ using Equation (3.81)
      iii For $q = 1, \ldots, Q$, calculate $\mathbf{a}_{cq}^{k+1}$ using Equation (3.84)
      iv For $q = 1, \ldots, Q$, update $\boldsymbol{\lambda}_{cq}^{k+1}$ using Equation (3.70)
    2. For $q = 1, \ldots, Q$, calculate $\mathbf{s}_q^{k+1}$ by analogy to one of Equations (3.48) or (3.61)
    3. Set $k = k + 1$
  end while
  return $\mathbf{x} = \left[\mathbf{x}_R^k, \mathbf{x}_G^k, \mathbf{x}_B^k\right]$

Chapter 4

Experimental Results

This chapter analyzes the experimental results obtained for the proposed algorithms. Once the used assessment criteria are presented, an intra-process analysis is performed, i.e. a comparative study of internal techniques for the different CSSR algorithm steps proposed in the thesis is presented, and how they affect the overall performance is analyzed. Then, the proposed framework is compared with existing SR and CS ID algorithms, which can be considered as special cases of the general CSSR algorithm. This is followed by the analysis of the CSSR algorithm in its general case. Finally, two main applications of the CSSR algorithm are examined: PMMW and color images.

4.1 Quality Assessment

The CSSR reconstruction problem estimates one HR image of a scene. Usually, we do not have the original image to compare it with the estimated one. However, there are some measures that can help indicating the performance level of the estimation process.

The first assessment criterion is the human eye perception which to some limit can be adopted. However, it does not give a standard measure and it may depend on the person himself looking at the estimated image.

Another assessment criteria which may give a better judgment are machine vision techniques, where the estimated image is forwarded to another processing step to make a decision or to operate a device. The reliability and accuracy measures of the machine are known, then the merits of the estimated image, which is fed as the input to the machine, will affect the performance of the machine. The change in overall performance of the machine definitely gives an indication about how much efficient the estimation process was. As an example, let us consider a set of PMMW images, how to measure the performance of the super resolved image? The answer is that when the HR is fed to a threat detection algorithm, and this leads to higher reliability then this will be a consequence of the higher quality of the estimated image.

To simplify matters, usually input images can be simulated to approximate the real ones. If the original image is $\mathbf{x}$, then we can generate LR versions of it. Then, these simulated input images are fed to the algorithm, to find an estimate of the HR image $\hat{\mathbf{x}}$. Notice that by this we already have both the original image and the estimated image. In such a case, mathematical measures can be used to assess the performance of the proposed algorithm.

Many performance measures have been utilized in image processing, like the mean square error and peak signal to noise ratio, explained next.

Mean Squared Error (MSE). It is the average squared difference error between the estimated and original images. It is calculated by

$$MSE = \frac{1}{N} \| \mathbf{x} - \hat{\mathbf{x}} \|^2, \tag{4.1}$$

where $\mathbf{x}$ and $\hat{\mathbf{x}}$ are $N \times 1$ vectors, representing respectively the original and estimated images, and $\| . \|$ is the Euclidean norm.

Peak Signal to Noise Ratio (PSNR). It measures the ratio between the maximum possible power in the image to the power of the fidelity term, and it is expressed as

$$PSNR = 10 \log \frac{\max(\mathbf{x})^2}{MSE}, \tag{4.2}$$

where $\max(\mathbf{x})$ is the maximum possible value of the image $\mathbf{x}$. Notice here that $\max(\cdot)$ is not a function of the information in the image, instead it is a function of how the image is represented. If the image intensities are saved using 8-bit integer representation then the maximum possible value is 255. If the image is saved in a normalized format then the maximum value is 1.0.

We utilize both measures in the simulated experiments to indicate the quality of output image. To define a robust stopping criterion for the iterated process the following condition is used

$$\frac{\| \hat{\mathbf{x}}^k - \hat{\mathbf{x}}^{k-1} \|}{\| \hat{\mathbf{x}}^{k-1} \|} \leq 10^{-3}, \tag{4.3}$$

where $\hat{\mathbf{x}}^k$ and $\hat{\mathbf{x}}^{k-1}$ are the estimated images at iterations k and $k-1$, respectively.

4.2 Intra CSSR Analysis

The CSSR algorithm consists of a number of several internal processes. These are mainly the LR transform coefficient estimation, registration parameter estimation, and HR image estimation. To obtain good quality output images all intra processes should perform well, a failure in any step will definitely degrade the overall process. An experimental study of the first two processes is presented in the following two sub-sections.

4.2.1 CS Reconstruction

This section analyzes mainly the CS transformed coefficient vectors $\mathbf{a}_q$ and the effect of the iterative process on the reconstructed LR images $\mathbf{W}\mathbf{a}_q$ when compared to the first-iteration estimate. A better quality of $\mathbf{W}\mathbf{a}_q$ will definitely improve the overall CSSR performance.

Let us now illustrate how blurring affects image sparsity (see [5]). It was shown in [15] that images whose coefficients in a transformed domain follow a power decay law, when sorted by decreasing magnitude, are sparse in this domain. In this dissertation the 3-level Haar wavelet will be used as the transform basis. Let us see how blurring does affect the decay of the transformed coefficients for the standard Cameraman and Shepp-Logan images. Gaussian blur of variances 3 and 9 has been applied to those images and white Gaussian noise with Signal-to-Noise ratio SNR= 40 dB has been added. Figures 4.1(a,b) show the magnitude versus sorted indices of the wavelet coefficients. Similarly, Figures 4.1(c,d) show the results for the standard Shepp-Logan image for the two blur variances 3 and 9, respectively. More severe blur results in a faster magnitude decay, as it is clear in the figure.

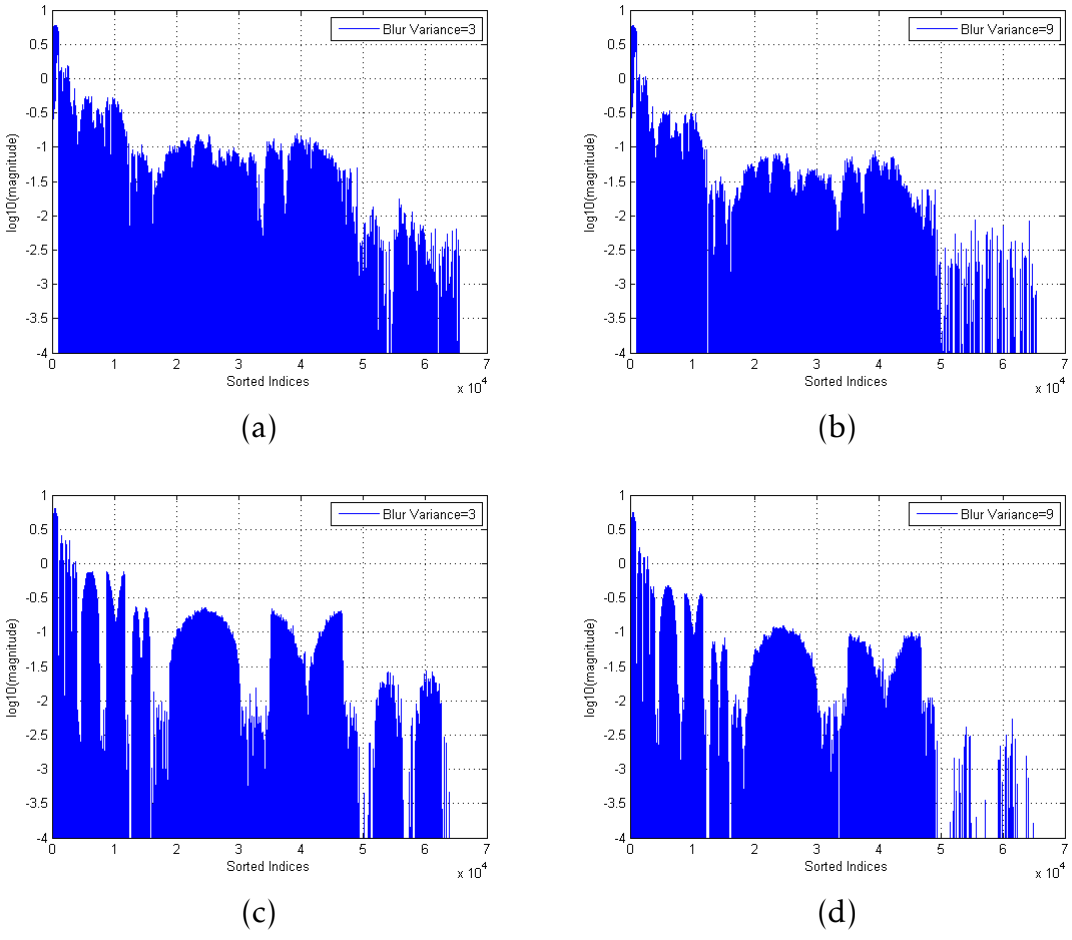

Figure 4.1: LR 3-level Haar wavelet coefficient decay, using simulated observations (SNR= 40 dB), (a,b) Cameraman image affected by Gaussian blur of variance 3 and 9, respectively. (c,d) Shepp-Logan image affected by blur of variance 3 and 9, respectively.

The next point to discuss here is the effect of the pruning of the coefficients on the estimated image. Figure 4.2(a) shows the reconstructed LR Cameraman image by including all the coefficients in the transformed vector $\mathbf{a}_q$. The experiment utilized R=0.8, P=1, blur Vari-

(a) (b) (c)

Figure 4.2: LR Cameraman image restoration using a simulated observation with blur variance 3, zooming factor P=1, R=0.8, noise SNR= 40 dB. (a) LR reconstructed observation using all elements of the coefficient vector $\mathbf{a}_q$ (PSNR=22.65 dB), (b) LR reconstructed observation using the first 60% of elements in $\mathbf{a}_q$ (PSNR=22.47 dB), (c) LR reconstructed observation using the first 20% of elements in $\mathbf{a}_q$ (PSNR=22.24 dB). Transform basis used is 3-level Haar wavelet transform.

ance=3, and noise SNR= 40 dB, and the resulting PSNR is 22.65 dB. Next, only the first 60% of the transformed coefficients in $\mathbf{a}_q$ were kept, while the others were pruned, then the resulting transformed vector is used to estimate the LR image shown in Figure 4.2(b), with PSNR=22.47 dB. Then, the LR image is estimated using only the first 20% of $\mathbf{a}_q$, the result is shown in Figure 4.2(c) with PSNR=22.24 dB.

The previous experiment has been repeated for the Shepp-Logan image, whose results are shown as follows: Figure 4.3(a) shows the estimated image with all $\mathbf{a}_q$ included (PSNR=21.35 dB), Figure 4.3(b) utilized only 60% of $\mathbf{a}_q$ (PSNR=21.18 dB), and finally, Figure 4.3(c) utilized only 20% of $\mathbf{a}_q$ (PSNR=20.68 dB).

Next we discuss the effect of the iterative process on the performance of the CS reconstruction. We use two simulated LR images of the standard Shepp-Logan image shown in Figure 4.4(a). To simulate two LR observations, the HR image of size 256×256 pixels, was warped using the following motion vectors: $[0, 0, 0]^t$, $[-0.1047, 2, -3]^t$, then blurred with a Gaussian blur of variance=3, then down-sampled by a zooming factor P=2. The two simulated LR images are shown in Figure 4.4(b,c). These simulated LR images are then compressed with a compression ratio R=0.8, and noise is added with SNR=30dB.

Let us examine the first iteration LR estimations using Equation (3.38), without the regularization term. The estimated images are shown in Figure 4.4(d,e), and the PSNR values of the reconstructed LR images are 40.22 dB and 40.16 dB, respectively. As the CSSR process advances, the inclusion of the registration term allows for a better extraction of the information in the compressed observations; the final estimated LR images are shown in Figure 4.4(f,g), with PSNR values being 42.88 dB and 42.77 dB, respectively. Notice in this experiment that the PSNR values were calculated with respect to the simulated LR observations, not to the original HR image.

For the Cameraman image shown in Figure 4.5(a), the down-sampled images are shown in

(a) (b) (c)

Figure 4.3: LR Shepp-Logan image restoration using a simulated observation with blur variance 3, zooming factor P=1, R=0.8, noise SNR=40dB. (a) LR reconstructed observation using all elements of the coefficient vector $\mathbf{a}_q$ (PSNR=21.35 dB), (b) LR reconstructed observation using the first 60% of elements in $\mathbf{a}_q$ (PSNR=21.18 dB), (c) LR reconstructed observation using the first 20% of elements in $\mathbf{a}_q$ (PSNR=20.68 dB). Transform basis used is 3-level Haar wavelet transform.

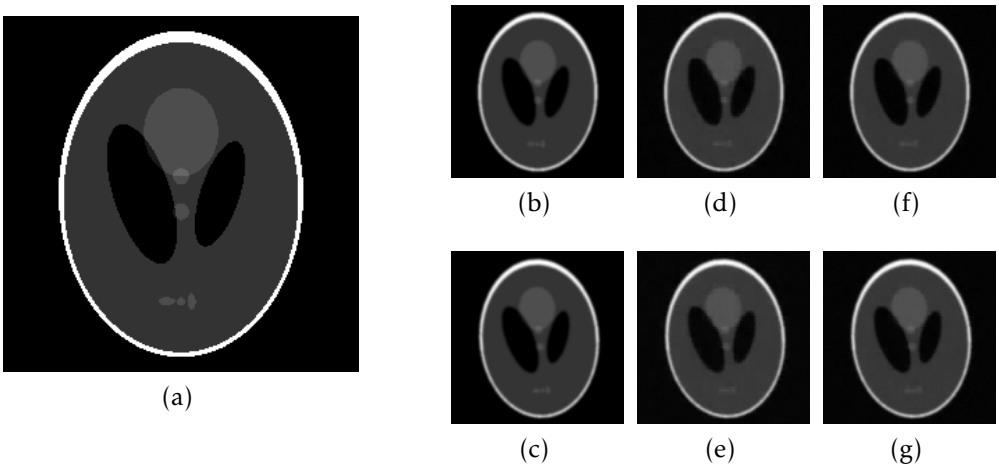

(a) (b) (d) (f) (c) (e) (g)

Figure 4.4: Reconstruction of LR images. (a) Original HR Shepp-Logan image, (b,c) Down-sampled images Q=2, P=2, Blur Var=3, R=0.8, SNR=30 dB, (d,e) First estimates of the LR images, PSNR= 40.22 dB and , 40.16 dB respectively, (f,g) Final estimates of the LR images, PSNR=42.88 dB and 42.77 dB respectively. PSNR values were calculated with respect to the simulated LR images.

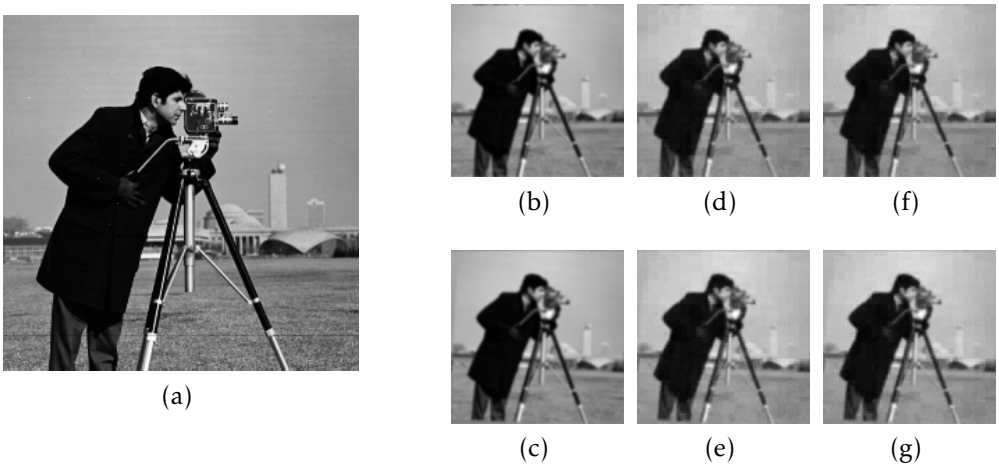

Figure 4.5: Reconstruction of LR images. (a) Cameraman original HR image, (b,c) Down-sampled images Q=2, P=2, Blur Var=3, R=0.8, SNR=30dB, (d,e) First estimates of the LR images, PSNR=35.52 dB and 35.29 dB, respectively, (f,g) Final estimates of the LR images, PSNR=35.55 dB and 35.34 dB, respectively. PSNR values were calculated with respect to the simulated LR images.

Figure 4.5(b,c), the initially estimated LR images are shown in Figure 4.5(d,e), with PSNR=35.52 dB and 35.29 dB, respectively. The final estimated LR images are shown in Figure 4.5(f,g), with PSNRs equal to 35.55 dB and 35.34 dB, respectively. In this experiment the PSNR values were calculated with respect to the simulated LR observations, not to the original HR image.

For the Lena image shown in Figure 4.6(a), the down-sampled images are shown in Figure 4.6(b,c), the initially estimated LR images are shown in Figure 4.6(d,e), with PSNR=32.45 dB and 32.28 dB, respectively. The final estimated LR images are shown in Figure 4.6(f,g), with PSNRs equal to 34.24 dB and 34.07 dB, respectively. In this experiment the PSNR values were calculated with respect to the simulated LR observations, not to the original HR image.

Notice that the inclusion of the regularization term in Equation (3.38) greatly contributes to the PSNR improvement when using the CSSR algorithm. This improvement will be very useful when super resolving the LR observations to estimate the HR image. Notice here also that the shown images are not the HR images but only the uncompressed versions of the LR images.

4.2.2 Registration Estimation

In this section we study the performance of various approaches to estimate the registration parameters as a step that greatly affects the overall HR image estimation. To do so, two experiments were carried out, for every approach, to establish the CSSR accuracy when estimating the registration parameters. The 256×256 pixel HR Shepp-Logan image, with Q=4, Blur variance=3, SNR=40dB, and R=0.8 were used. P=2 and 4, were chosen to conduct these two

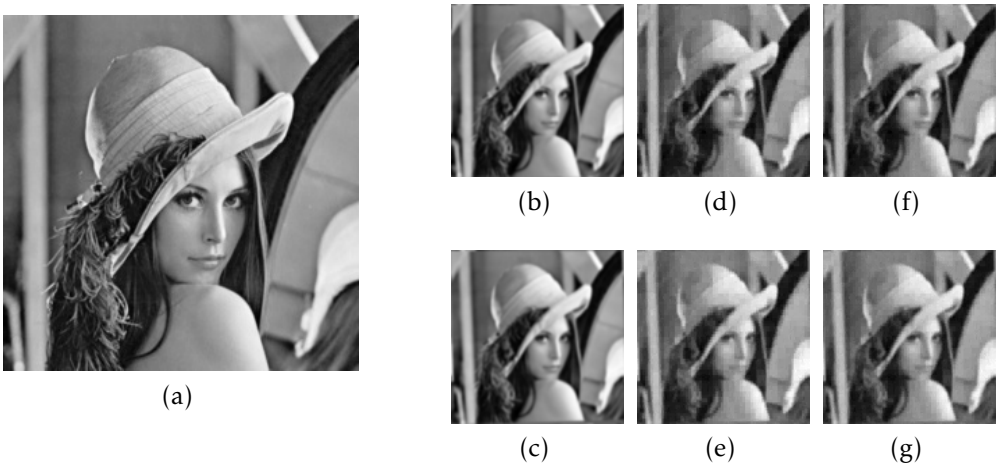

Figure 4.6: Reconstruction of LR images. (a) Lena original HR image, (b,c) Down-sampled images Q=2, P=2, Blur Var=3, R=0.8, SNR=30dB, (d,e) First estimates of the LR images, PSNR=40.22 dB and 40.16 dB, respectively, (f,g) Final estimates of the LR images, PSNR=42.88 dB and 42.77 dB, respectively. PSNR values were calculated with respect to the simulated LR images.

experiments, and the maximum number of iterations was 30.

Here are the approaches,

- App1, see also [19]. It estimates the parameters with respect to a reference LR image, at the HR level, following the optimization in Equation (3.16). The results for this approach are tabulated in Table 4.1(a) which shows the real and estimated registration parameters. It contains also the absolute errors. Notice that for the first observation, which is the reference observation, the motion vector is $[0,0,0]^t$, so the motion vectors were adjusted accordingly to this.

- App2, see also [20]. It estimates the parameters with respect to the estimated image, at the HR level, as in Equation (3.17). See Table 4.1(b) for results of this approach.

- App3, see also [18]. It estimates the parameters with respect to the estimated image, at the LR level, as in Equation (3.41). See Table 4.2(a) for results of this approach.

- App4. It estimates the parameters with respect to a reference LR image, at the LR level, as in Equation (3.51). See Table 4.2(b) for results of this approach.

Figure 4.7 shows a plot of the average absolute errors for each element in $\mathbf{s}_q, (q \in \{1,\cdots,4\})$, for the four approaches. The four approaches are suggested to be used with high accuracy. Later in Section 4.5.3 we will investigate more the effects of using App3 and App4 on the overall performance of the CSSR algorithm.

Table 4.1: Registration parameter estimation at the HR level for the Shepp-Logan image, Q=4, Blur var=3, SNR=40dB, R=0.8. (a) using App1, (b) using App2

Zooming Factor	Observation, q=2			
	Motion Vector	θ_q	c_q	d_q
2,4	True	.05236	2.00	-3.00
2	Estimated	.05233	1.83	-3.106
	Abs. Error	7.0e-5	1.7e-1	1.1e-1
4	Estimated	.0504	1.818	-3.114
	Abs. Error	2.0e-3	1.8e-1	1.1e-1
	Observation, q=3			
2,4	True	-.06981	-1.0	-2.0
2	Estimated	-.06978	-.8482	-2.069
	Abs. Error	2.0e-5	1.5e-1	6.9e-2
4	Estimated	-.06647	-.859	-2.089
	Abs. Error	3.3e-3	1.4e-1	8.9e-2
	Observation, q=4			
2,4	True	-.03491	3.0	-1.0
2	Estimated	-.03489	3.036	-.8885
	Abs. Error	1.0e-5	3.6e-2	1.1e-1
4	Estimated	-.03395	3.022	-.9236
	Abs. Error	9.5e-4	2.2e-2	7.6e-2

(a)

Zooming Factor	Observation, q=2			
	Motion Vector	θ_q	c_q	d_q
2,4	True	.05236	2.00	-3.00
2	Estimated	.04825	1.816	-3.385
	Abs. Error	4.2e-3	1.8e-1	3.9e-1
4	Estimated	.04809	1.958	-3.315
	Abs. Error	4.3e-3	4.2e-2	3.2e-1
	Observation, q=3			
2,4	True	-.06981	-1.0	-2.0
2	Estimated	-.07879	-.8134	-2.524
	Abs. Error	9.0e-3	1.9e-1	5.2e-1
4	Estimated	-.0722	-.6908	-2.19
	Abs. Error	2.4e-3	3.1e-1	1.9e-1
	Observation, q=4			
2,4	True	-.03491	3.0	-1.0
2	Estimated	-.0285	2.998	-.7152
	Abs. Error	6.4e-3	2.0e-3	2.8e-1
4	Estimated	-.03458	3.171	-.9075
	Abs. Error	3.2e-4	1.7e-1	9.3e-2

(b)

Table 4.2: Registration parameter estimation at the LR level for the Shepp-Logan image, Q=4, Blur var=3, SNR=40dB, R=0.8. (a) using App3 (b) using App4

Zooming Factor	Observation, q=2			
	Motion Vector	θ_q	c_q	d_q
2,4	True	.05236	2.00	-3.00
2	Estimated	.05229	1.999	-3.002
	Abs. Error	7.0e-5	1.0e-3	2.0e-3
4	Estimated	.05163	2.033	-3.057
	Abs. Error	7.3e-4	3.3e-2	5.7e-2
	Observation, q=3			
2,4	True	-.06981	-1.0	-2.0
2	Estimated	-.06916	-1.002	-2.005
	Abs. Error	6.5e-4	2.0e-3	5.0e-2
4	Estimated	-.06902	-1.012	-2.046
	Abs. Error	7.9e-4	1.2e-2	4.6e-2
	Observation, q=4			
2,4	True	-.03491	3.0	-1.0
2	Estimated	-.03478	3.00	-1.001
	Abs. Error	1.3e-4	1.0e-3	1.0e-3
4	Estimated	-.03351	2.999	-1.041
	Abs. Error	1.4e-3	1.0e-3	4.1e-2

(a)

Zooming Factor	Observation, q=2			
	Motion Vector	θ_q	c_q	d_q
2,4	True	.05236	2.00	-3.00
2	Estimated	.05255	1.999	-2.998
	Abs. Error	1.5e-4	1.0e-3	2.0e-3
4	Estimated	.05224	2.02	-3.058
	Abs. Error	1.6e-4	2.0e-2	5.8e-2
	Observation, q=3			
2,4	True	-.06981	-1.0	-2.0
2	Estimated	-.06984	-1.001	-2.
	Abs. Error	4.0e-5	1.0e-3	0.0e0
4	Estimated	-.06899	-1.014	-2.052
	Abs. Error	8.1e-4	1.4e-2	5.2e-2
	Observation, q=4			
2,4	True	-.03491	3.0	-1.0
2	Estimated	-.03497	2.999	-1.001
	Abs. Error	7.0e-5	1.0e-3	1.0e-3
4	Estimated	-.03388	2.967	-1.043
	Abs. Error	1.0e-3	3.3e-2	4.3e-2

(b)

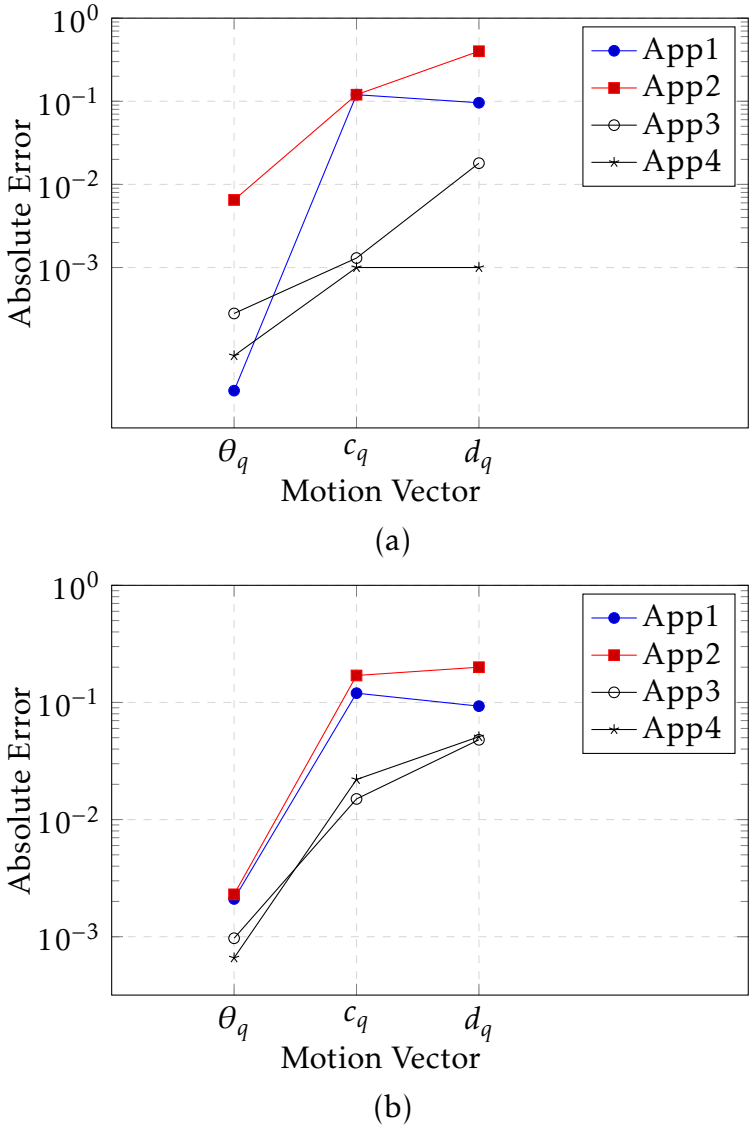

Figure 4.7: Absolute error comparison of the four registration approaches. R=0.8, Q=4, blur var=3, SNR=40dB. on (a) P=2, (b) P=4.

4.3 CSSR vs ID Works

In this section the performance of the proposed CSSR algorithm is compared with a set of existing image deconvolution CS algorithms, namely l1-ls [82], GPSR [68], NESTA [70], YALL1 [71], and CoSaMP [69], using their native codes. These algorithms estimate $\mathbf{x}$ from one CS blurred observation. Results were tabulated in Tables 4.3 to 4.5, CSSR used P=1 and Q=1.

Figure 4.8 shows plots of the performance measure, for all tested algorithms, vs compression ratio R, for the three test images, using Blur var=5 and SNR=30 dB. Figure 4.9 shows the plots for the case where Blur var=3 and SNR=40 dB. It is clear the quality level the CSSR offers in comparison to other works using one input CS observation. The performance of CSSR is expected to be better if multiple input images are used.

Next we test the performance as a function of the variance of the blur. To compare the performance for all algorithms, plots are shown for the case R=0.6 and SNR=30 dB in Figure 4.10, and for R=0.8, SNR=40 dB in Figure 4.11. As the plots show, the proposed CSSR algorithm estimates images of good quality, even when compared with CS image deconvolution works.

4.4 CSSR vs SR Works

This section compares the performance of the proposed CSSR algorithm with a set of existing SR algorithms, namely Bicubic Interpolation (BIC), SR using an l_1 prior [28] (L1S), SR using SAR priors [30] (SAS), a fast and robust SR [34] (FRSR), and a robust SR method [49] (RSR). Algorithms L1S [28] and SAS [30] estimate all their parameters. Since algorithms FRSR [34] and RSR [49] need some parameters to be set, we performed an exhaustive search to find the parameters resulting in the maximum PSNR values. We used the Cameraman, Shepp-Logan and Lena images. The number of observations was Q=4. For our CSSR, we used a unity compression ratio R=1.0 to compare with those SR algorithms which do not use CS observations. Notice that we still use CS but with 100% of the measurements which is equivalent to using $\mathbf{\Phi} = \mathbf{I}$. The results are tabulated in Tables 4.6 and 4.7.

The plots in Figures 4.12 and 4.13 compare the performance of SR algorithms as a function of the variance of the blur affecting the test images for two different noise SNR 40 dB and 30 dB, respectively. Both cases used Q=4 and P=4. Notice the relative improvement of the CSSR algorithm, when compared with SR algorithms that do not use compressed sensing, for the two cases.

Table 4.3: Performance comparison of state-of-the-art CS ID algorithms with proposed CSSR algorithm for the Cameraman image. For CSSR P=1 and Q=1. In bold blue are the highest PSNR values.

Image		Cameraman					
Blur Var		3		5		9	
SNR		40	30	40	30	40	30
Alg	R	PSNR, dB					
L1-LS	0.2	23.8	21.5	22.7	20.7	21.4	20.0
	0.4	24.2	22.3	23.0	21.1	21.5	20.5
	0.6	24.4	22.7	23.2	21.4	21.7	20.7
	0.8	24.6	22.9	23.3	21.5	21.7	20.8
	1.0	24.7	23.0	23.4	21.7	21.8	20.8
GPSR	0.2	22.9	19.4	**23.5**	20.3	**22.7**	**21.2**
	0.4	**25.2**	21.4	**24.1**	22.3	**22.9**	**22.2**
	0.6	**25.6**	22.9	24.3	23.2	22.9	22.6
	0.8	25.8	23.7	24.3	23.6	22.9	**22.7**
	1.0	25.8	24.3	24.3	23.8	23.0	22.8
CoSaMP	0.2	21.7	14.8	22.2	14.6	21.8	15.1
	0.4	23.5	15.3	23.3	16.2	22.8	17.2
	0.6	24.3	16.5	23.9	17.6	23.1	18.7
	0.8	24.9	17.4	24.3	18.5	23.3	19.5
	1.0	25.3	18.4	24.5	19.5	23.4	20.0
NESTA	0.2	**23.8**	22.2	22.9	**21.8**	21.5	21.0
	0.4	24.3	22.5	23.3	22.1	21.9	21.5
	0.6	24.5	22.8	23.4	22.4	22.1	21.7
	0.8	24.6	22.9	23.5	22.5	22.2	21.8
	1.0	24.6	22.9	23.4	22.4	22.1	21.7
YALL1	0.2	22.8	**22.6**	21.5	21.4	20.8	20.7
	0.4	23.3	23.1	21.9	21.8	20.9	20.9
	0.6	23.5	23.3	22.2	22.1	21.0	21.0
	0.8	23.7	23.5	22.3	22.2	21.0	21.0
	1.0	23.8	23.6	22.4	22.3	21.1	21.0
CSSR	0.2	23.2	22.0	22.6	21.6	21.6	20.8
	0.4	24.9	**23.6**	23.8	**22.8**	22.7	21.9
	0.6	25.5	**24.3**	**24.3**	**23.4**	**23.1**	**22.3**
	0.8	**25.9**	**24.8**	**24.6**	**23.8**	**23.3**	22.6
	1.0	**26.0**	**25.2**	**24.7**	**24.0**	**23.4**	**22.8**

Table 4.4: Performance comparison of state-of-the-art CS ID algorithms with proposed CSSR algorithm for the Lena image. For CSSR P=1 and Q=1. In bold blue are the highest PSNR values.

Image		Lena					
Blur Var		3		5		9	
SNR		40	30	40	30	40	30
Alg	R	PSNR, dB					
L1-LS	0.2	**26.5**	23.1	25.1	22.3	23.5	22.4
	0.4	27.3	24.1	25.6	23.0	23.7	22.5
	0.6	27.6	24.6	25.9	23.4	23.9	22.8
	0.8	27.8	25.0	26.0	23.5	24.0	22.9
	1.0	27.9	25.2	26.2	23.7	24.1	23.0
GPSR	0.2	25.3	22.2	**26.8**	23.9	**26.1**	**24.7**
	0.4	**29.3**	25.3	**28.2**	**26.3**	**26.5**	**25.8**
	0.6	**30.0**	26.9	**28.5**	**27.2**	26.5	**26.1**
	0.8	30.4	28.1	28.6	**27.7**	26.6	**26.3**
	1.0	30.7	28.7	28.7	**28.0**	26.6	**26.4**
CoSaMP	0.2	23.9	16.4	24.9	16.1	25.1	16.9
	0.4	26.2	16.8	26.7	18.0	26.4	19.5
	0.6	27.4	18.0	27.6	19.5	**26.9**	21.0
	0.8	28.2	19.1	28.1	20.6	27.1	21.9
	1.0	28.7	20.1	28.6	21.7	27.2	22.9
NESTA	0.2	26.5	**24.8**	25.4	**24.3**	23.6	23.2
	0.4	27.3	25.3	25.9	24.7	24.1	23.7
	0.6	27.6	25.7	26.2	25.1	24.2	24.0
	0.8	27.8	25.9	26.4	25.3	24.4	24.0
	1.0	27.8	25.8	26.2	25.0	24.3	24.0
YALL1	0.2	24.8	24.6	23.4	23.4	22.4	22.3
	0.4	25.7	25.5	23.9	23.9	22.8	22.8
	0.6	26.0	25.8	24.2	24.1	22.9	22.9
	0.8	26.3	26.1	24.4	24.3	23.0	23.0
	1.0	26.4	26.2	24.5	24.4	23.1	23.0
CSSR	0.2	24.0	22.4	23.8	22.7	22.6	21.7
	0.4	27.5	**26.3**	26.8	25.4	24.6	24.2
	0.6	29.5	**27.9**	28.2	26.7	26.5	25.2
	0.8	**30.6**	**28.8**	**29.0**	27.4	**27.1**	25.8
	1.0	**31.2**	**29.4**	**29.4**	27.9	**27.4**	26.2

Table 4.5: Performance comparison of state-of-the-art CS ID algorithms with proposed CSSR algorithm for the Shepp-Logan image. For CSSR P=1 and Q=1. In bold blue are the highest PSNR values.

Image		Shepp-Logan					
Blur Var		3		5		9	
SNR		40	30	40	30	40	30
Alg	R	PSNR, dB					
L1-LS	0.2	22.8	21.6	22.0	21.2	20.5	20.2
	0.4	23.1	21.8	22.3	21.5	20.7	20.4
	0.6	23.3	21.9	22.3	21.6	20.8	20.5
	0.8	23.5	22.0	22.4	21.6	20.9	20.6
	1.0	23.7	22.1	22.4	21.7	20.9	20.7
GPSR	0.2	24.1	20.5	**23.6**	20.9	**22.2**	**21.1**
	0.4	25.2	21.4	24.0	22.4	22.3	21.9
	0.6	25.4	22.7	24.1	23.1	22.3	22.1
	0.8	25.5	23.6	24.1	23.5	22.5	22.2
	1.0	25.5	24.1	24.1	23.68	22.4	22.3
CoSaMP	0.2	22.9	17.5	22.6	17.6	21.9	18.3
	0.4	23.8	19.3	23.3	19.3	22.2	19.8
	0.6	24.2	20.6	23.5	20.4	22.4	20.7
	0.8	24.6	21.4	23.6	21.2	22.4	21.2
	1.0	24.6	21.9	23.6	21.7	22.4	21.4
NESTA	0.2	22.8	22.4	22.1	21.7	20.5	20.4
	0.4	23.2	22.8	22.3	22.0	20.8	20.8
	0.6	23.4	23.1	22.4	22.2	21.0	21.1
	0.8	23.5	23.2	22.5	22.3	21.2	21.2
	1.0	23.6	23.3	22.4	22.2	21.0	21.2
YALL1	0.2	22.1	22.0	20.7	20.7	19.4	19.4
	0.4	22.3	22.3	21.0	21.0	19.6	19.6
	0.6	22.4	22.4	21.2	21.2	19.9	19.8
	0.8	22.5	22.5	21.5	21.4	20.0	20.0
	1.0	22.6	22.6	21.7	21.6	20.1	20.0
CSSR	0.2	**24.2**	**23.2**	23.1	**22.2**	20.9	21.0
	0.4	**25.4**	**25.3**	**24.1**	**24.1**	**22.4**	**22.2**
	0.6	**25.7**	**26.1**	**24.4**	**24.7**	**22.7**	**22.9**
	0.8	**25.8**	**26.4**	**24.5**	**24.9**	**22.9**	**23.2**
	1.0	**25.8**	**26.5**	**24.5**	**25.0**	**22.9**	**23.3**

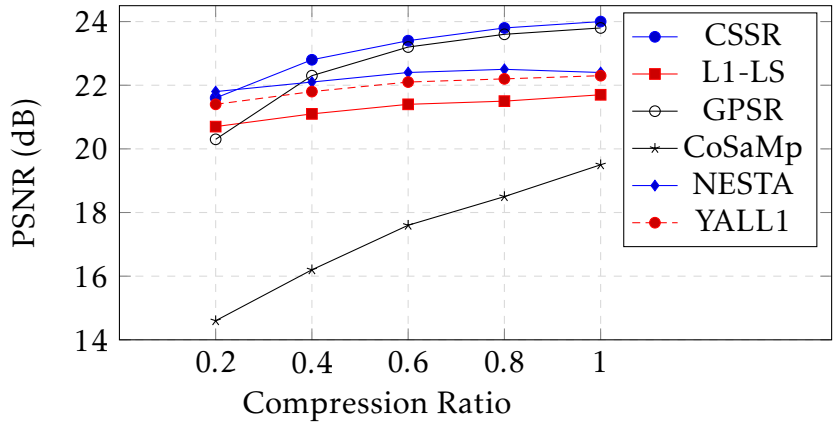

(a)

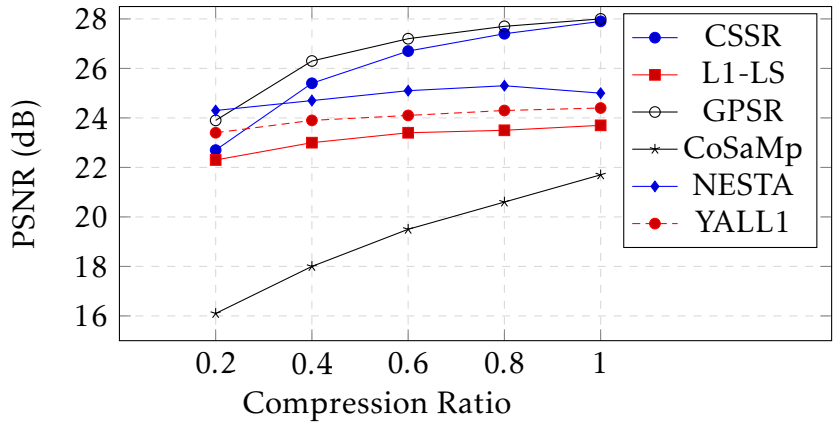

(b)

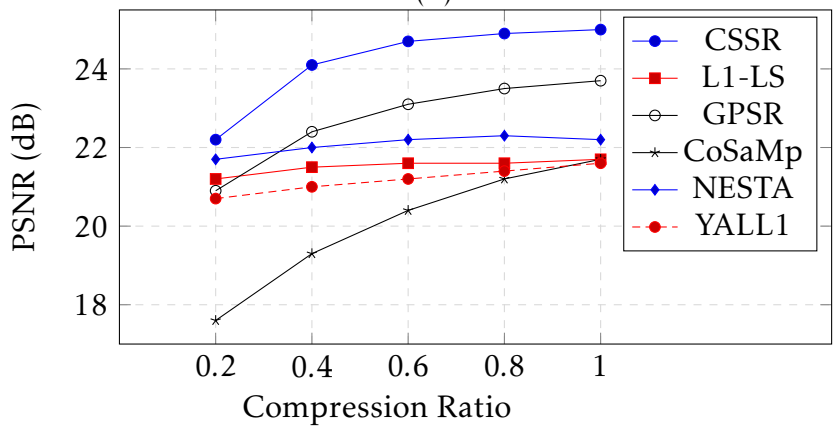

(c)

Figure 4.8: Proposed CSSR vs CS ID algorithms comparison (Blur Var=5, SNR=30dB, for CSSR P=1, Q=1). (a) Cameraman (b) Lena (c) Shepp-Logan.

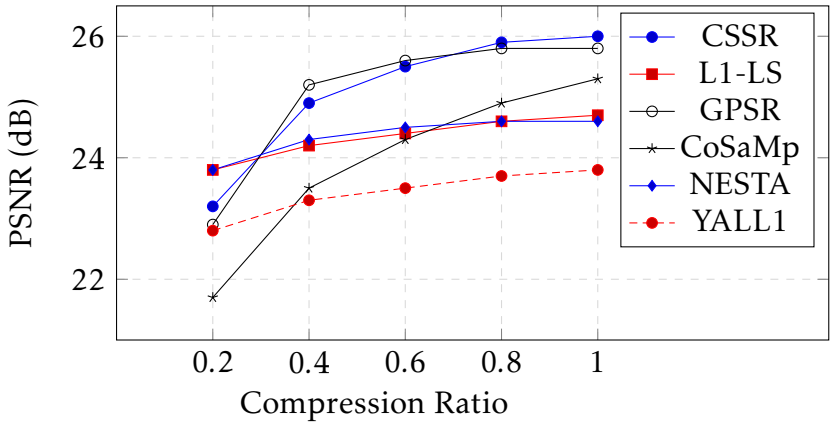

(a)

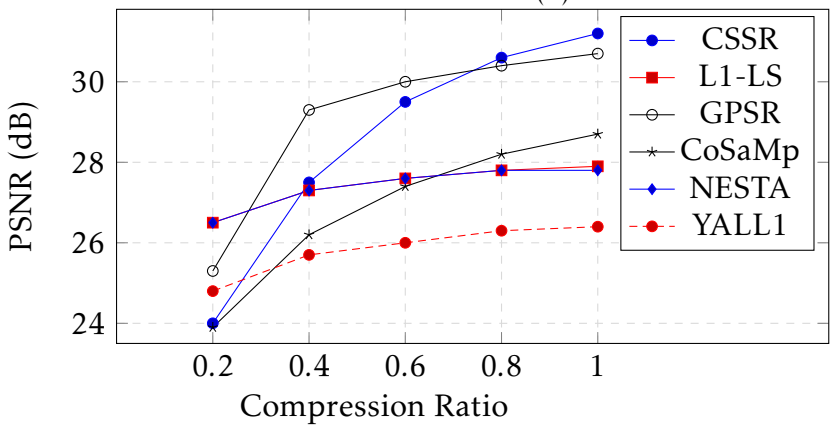

(b)

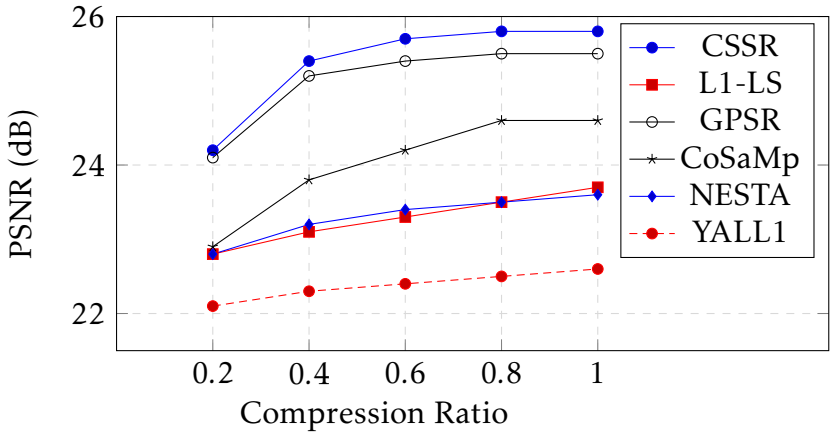

(c)

Figure 4.9: Proposed CSSR vs CS ID algorithms comparison (Blur Var=3, SNR=40dB, for CSSR P=1, Q=1). (a) Cameraman, (b) Lena, (c) Shepp-Logan.

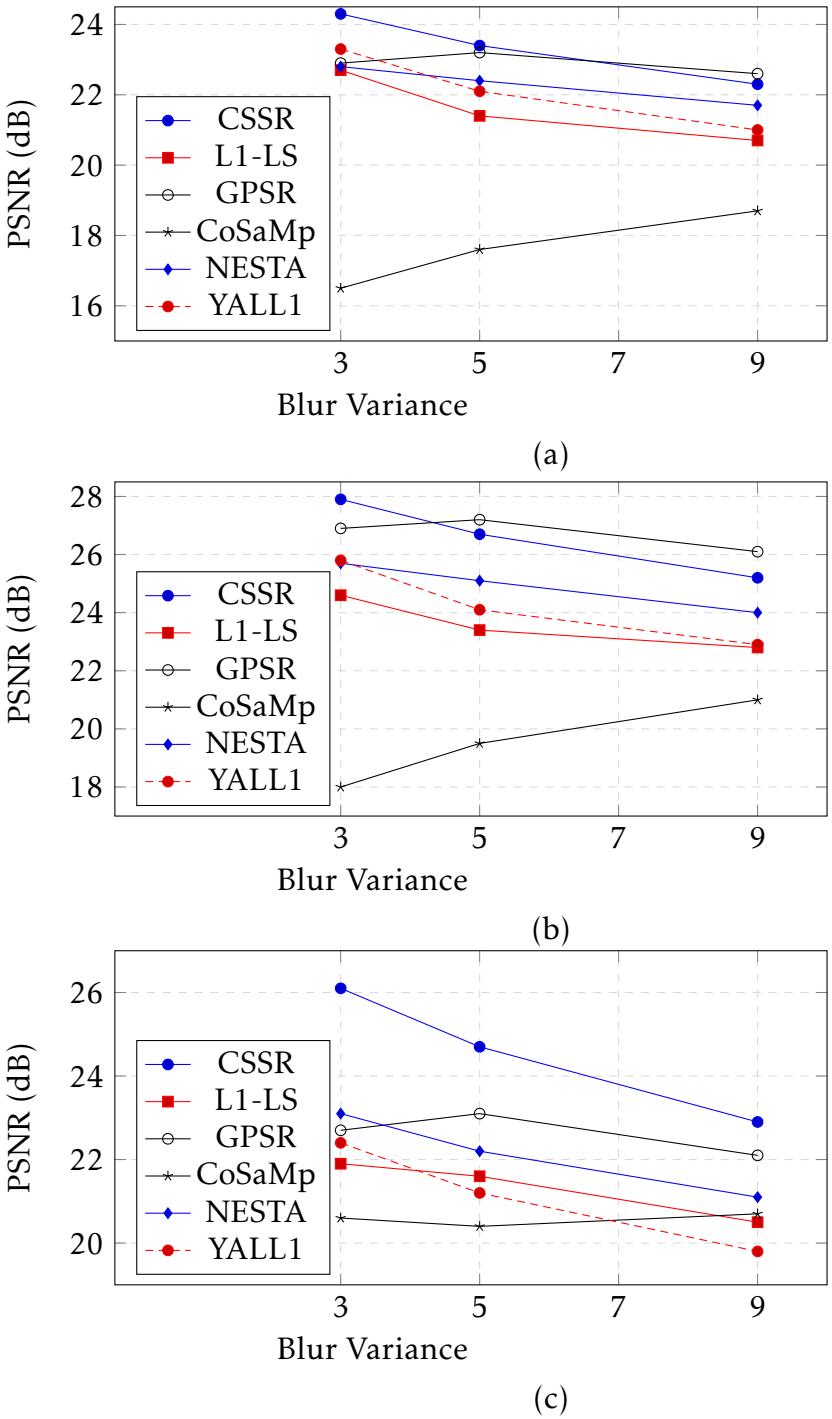

Figure 4.10: Proposed CSSR vs CS ID algorithms comparison (R=0.6, SNR=30dB, for CSSR P=1, Q=1). (a) Cameraman, (b) Lena, (c) Shepp-Logan.

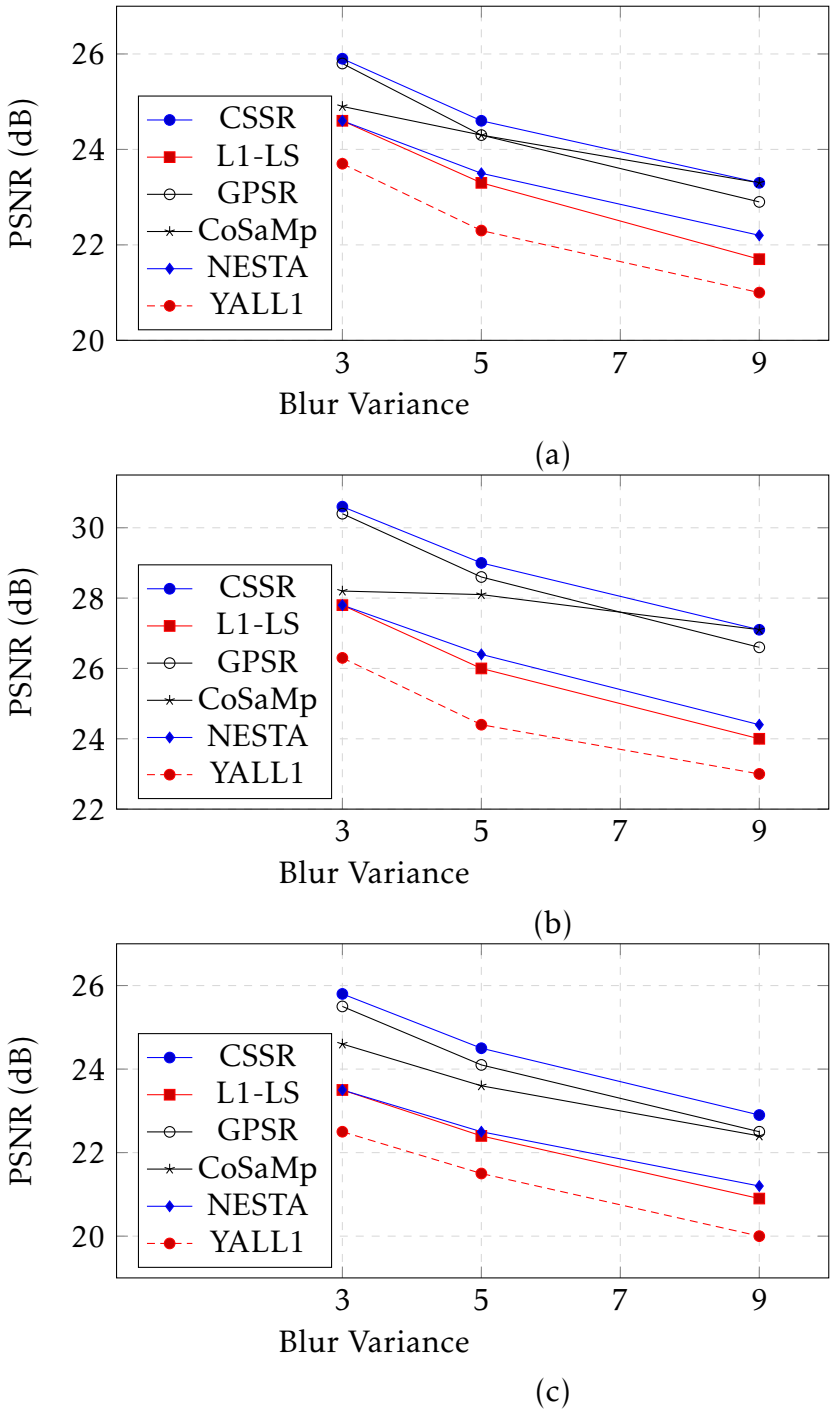

Figure 4.11: Proposed CSSR vs CS ID algorithms comparison (R=0.8, SNR=40dB, for CSSR P=1, Q=1). (a) Cameraman, (b) Lena, (c) Shepp-Logan.

Table 4.6: Comparison of state-of-the-art SR algorithms with the CSSR algorithm for Cameraman and Lena images, with Q=4 and for CSSR R=1.0. In bold blue are the highest PSNR values.

Image		Cameraman					
Blur Var		3		5		9	
SNR		40	30	40	30	40	30
Alg	P	PSNR, dB					
BIC	2	22.5	22.7	22.4	22.3	22.4	22.4
	4	20.5	20.4	20.5	20.5	20.5	20.4
L1S	2	24.1	24.5	23.9	**24.2**	24.1	**23.9**
	4	21.9	22.1	21.7	21.3	21.7	21.6
SAS	2	24.1	23.7	24.1	23.4	**24.2**	23.3
	4	22.2	22.4	22.1	22.0	22.2	22.1
FRSR	2	20.9	21.5	19.3	19.8	21.5	20.6
	4	21.1	22.3	20.9	21.2	21.1	21.8
RSR	2	22.5	22.2	21.1	21.6	21.3	22.0
	4	20.5	20.6	20.4	20.5	20.5	20.6
CSSR	2	**25.9**	**24.8**	**24.6**	23.8	23.4	22.6
	4	**25.0**	**24.1**	**24.0**	**23.3**	**23.1**	**22.3**
Image		Lena					
BIC	2	24.7	24.7	24.6	24.6	24.5	24.4
	4	21.1	21.0	21.1	21.0	21.1	21.1
L1S	2	27.0	27.4	27.2	27.5	26.7	27.4
	4	25.8	25.7	25.9	25.4	25.9	26.0
SAS	2	27.7	27.5	28.4	27.6	**28.3**	**27.5**
	4	26.4	26.3	26.9	25.9	26.5	**26.4**
FRSR	2	20.5	20.8	21.2	20.9	22.0	20.1
	4	21.9	22.4	21.8	23.2	21.8	24.9
RSR	2	23.1	25.2	25.0	25.1	24.2	23.0
	4	21.7	21.9	21.7	21.8	21.9	22.0
CSSR	2	**31.1**	**29.0**	**29.4**	**27.6**	27.3	26.0
	4	**29.4**	**27.4**	**28.2**	**26.4**	**26.7**	25.2

Table 4.7: Comparison of state-of-the-art SR algorithms with the CSSR algorithm for Shepp-Logan image, with Q=4 and for CSSR R=1.0. In bold blue are the highest PSNR values.

Image		Shepp-Logan					
Blur Var		3		5		9	
SNR		40	30	40	30	40	30
Alg	P	PSNR, dB					
BIC	2	20.5	20.5	20.5	20.8	20.3	20.3
	4	17.9	17.8	17.9	17.9	17.9	17.9
L1S	2	25.7	**27.9**	**27.9**	**30.3**	**26.2**	**27.7**
	4	20.7	20.4	21.2	21.1	21.7	21.6
SAS	2	24.1	23.3	24.1	23.2	24.1	23.2
	4	21.4	21.8	22.0	22.1	22.2	21.5
FRSR	2	20.0	20.8	20.2	21.9	20.2	21.0
	4	20.8	20.5	20.5	20.9	21.0	20.8
RSR	2	21.1	21.0	21.4	21.0	21.3	21.1
	4	18.7	18.8	18.7	18.7	18.6	18.4
CSSR	2	**25.8**	26.4	24.4	24.9	22.9	23.2
	4	**24.7**	**25.3**	**23.7**	**24.1**	**22.4**	**22.6**

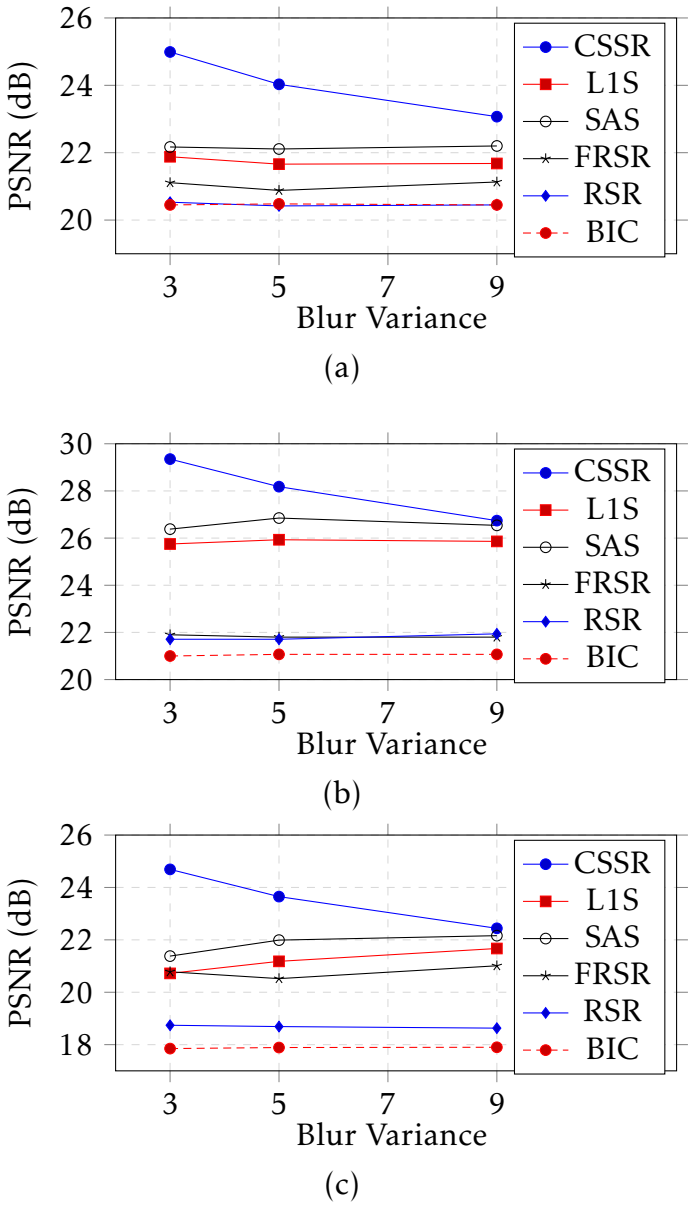

Figure 4.12: Comparison between SR algorithms and the CSSR algorithm. P=4, SNR=40dB, Q=4, and for CSSR, R=1.0. (a) Cameraman image, (b) Lena, (c) Shepp-Logan image.

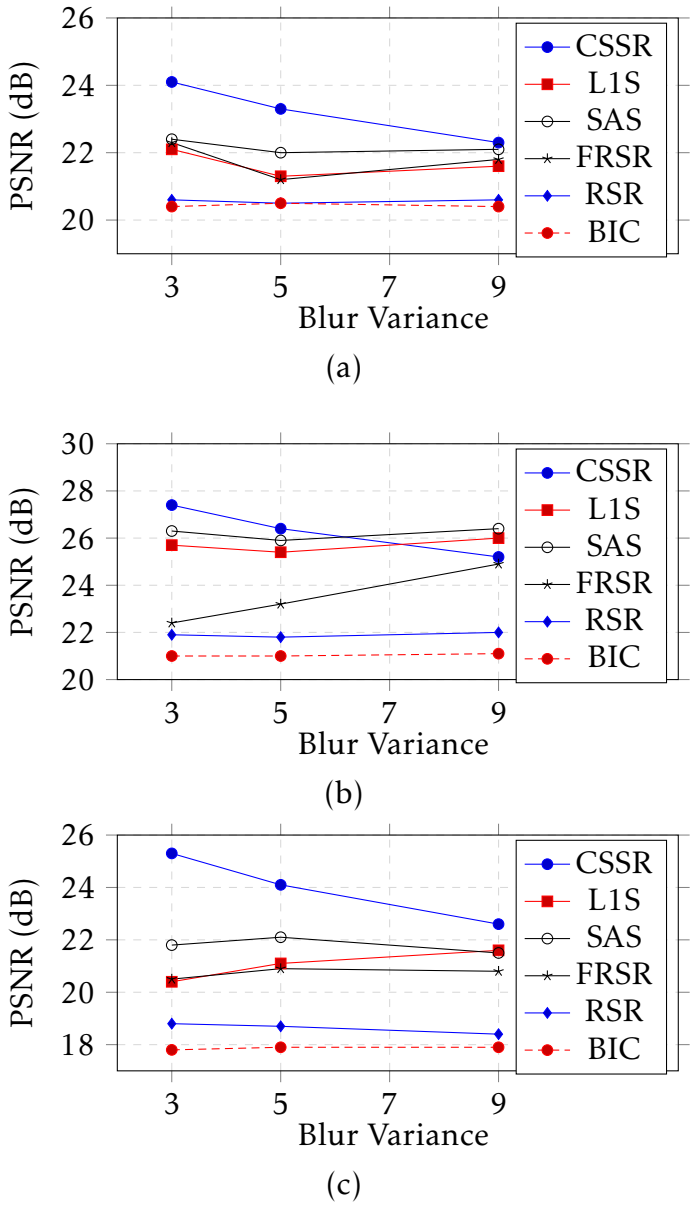

Figure 4.13: Comparison between SR algorithms and the CSSR algorithm. P=4, SNR=30dB, Q=4, and for CSSR, R=1.0. (a) Cameraman image, (b) Lena, (c) Shepp-Logan image.

4.5 CSSR: The General Case

In this section the overall behavior of the CSSR algorithm is investigated; both the compression ratio and zooming factor will be varied and the results analyzed. Notice here that we test the CSSR in its general case for different R and P values, while in the previous two sections R, P or Q were fixed at 1 to be able to compare our work with existing works which do not adapt to this general case. In this section we use the images shown in Figure 4.14, namely Satellite, Barbara, Peppers, and Alhambra images.

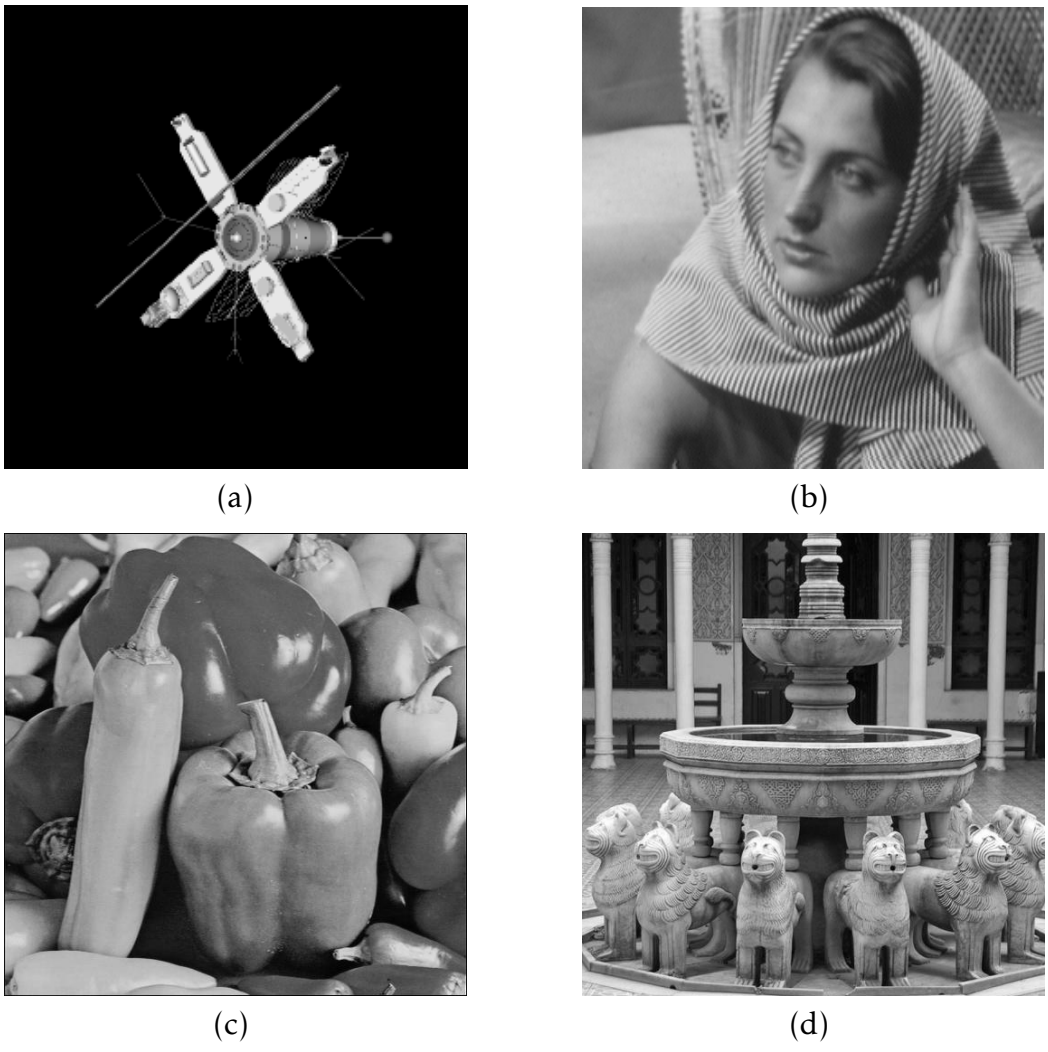

(a) (b)

(c) (d)

Figure 4.14: Original Images. (a) Satellite, (b) Barbara, (c) Peppers, (d) Alhambra.

The performance of CSSR is shown in Tables 4.8 and 4.9 for the four test images, using Q=4.

Next we will choose four examples to precisely explore the CSSR performance. For every zooming factor, two cases were chosen: in one the image is affected by simple degradations

Table 4.8: Performance of the CSSR algorithm for the Satellite and Barbara images, using $Q = 4$.

Blur Var			3		5		9	
SNR			40	30	40	30	40	30
Image	P	R	PSNR (dB)					
Satellite	2	0.2	26.5	24.9	26.0	24.4	24.9	23.8
		0.4	28.1	26.9	27.1	26.1	25.8	25.1
		0.6	28.4	27.7	27.3	26.8	26.0	25.7
		0.8	28.5	28.1	27.4	27.1	26.1	25.9
		1.0	28.5	28.3	27.4	27.3	26.1	26.0
	4	0.2	21.0	20.7	20.9	20.1	20.1	19.7
		0.4	27.0	25.8	26.3	25.1	25.3	24.2
		0.6	27.5	27.0	26.7	26.2	25.6	25.1
		0.8	27.6	27.3	26.8	26.6	25.7	25.5
		1.0	27.6	27.4	26.8	26.7	25.8	25.6
Barbara	2	0.2	19.0	19.5	19.7	19.6	19.1	18.7
		0.4	22.5	21.9	22.2	21.6	21.7	21.2
		0.6	23.5	22.8	23.2	22.5	22.7	22.1
		0.8	24.1	23.4	23.6	23.0	23.1	22.5
		1.0	24.5	23.8	23.9	23.3	23.3	22.8
	4	0.2	15.1	15.3	15.7	16.2	15.3	15.9
		0.4	18.4	19.0	18.0	19.0	18.0	18.8
		0.6	21.5	20.7	21.6	20.7	21.3	20.2
		0.8	23.0	22.2	22.9	22.0	22.6	21.6
		1.0	24.0	23.2	23.5	22.9	23.1	22.4

Table 4.9: Performance of the CSSR algorithm for the Peppers and Alhambra images, using $Q = 4$.

Blur Var			3		5		9	
SNR			40	30	40	30	40	30
Image	P	R	PSNR (dB)					
Peppers	2	0.2	16.2	17.6	15.5	17.3	13.7	16.8
		0.4	24.3	21.9	23.8	22.2	22.7	21.2
		0.6	27.3	25.3	26.1	24.3	24.6	23.0
		0.8	29.1	26.8	27.6	25.6	25.7	24.0
		1.0	30.2	27.9	28.4	26.5	26.4	24.7
	4	0.2	13.0	13.0	13.0	12.9	12.3	12.9
		0.4	15.1	15.0	15.3	15.2	15.0	15.4
		0.6	18.4	16.3	23.3	16.4	22.5	20.4
		0.8	26.2	25.2	25.5	23.5	24.4	22.5
		1.0	28.1	26.0	27.0	25.1	25.6	23.8
Alhambra	2	0.2	15.0	18.8	15.0	18.6	18.3	18.2
		0.4	24.2	22.4	21.1	21.9	22.5	21.0
		0.6	26.5	24.5	25.4	23.6	23.9	22.4
		0.8	28.0	25.9	26.5	24.8	24.7	23.3
		1.0	28.9	26.9	27.1	25.6	25.1	23.9
	4	0.2	12.3	13.7	12.7	14.0	13.0	13.7
		0.4	13.3	15.7	18.4	17.1	18.4	16.9
		0.6	21.7	20.7	22.1	20.4	21.1	19.7
		0.8	25.2	23.2	24.6	22.8	23.4	21.7
		1.0	27.2	25.5	25.9	24.5	24.3	23.2

while in the other is affected with hard degradations. These are:

- Case 1. P=2, Blur Variance=3, SNR=40 dB.
- Case 2. P=2, Blur Variance=5, SNR=30 dB.
- Case 3. P=4, Blur Variance=3, SNR=40 dB.
- Case 4. P=4, Blur Variance=5, SNR=30 dB.

Figures 4.15 and 4.16 show plots of the PSNR vs R. These plots, show how the PSNR, as a function of compression ratio, is affected when changing P, blur variance, and the noise added to the input images. As expected, PSNR increases when decreasing the zooming factor, decreasing the blur, increasing R, and increasing the SNR of the observed image.

Let us now visually assess the quality of the CSSR method by watching the estimated images for some examples. To do so we choose R=0.8 to show the estimated images in Figure 4.17 In all these experiments the number of observations was fixed at Q=5, while the values of P and the blur variance have been varied. Figures 4.17 to 4.20(a-d) used respectively P=2, Blur Var 3, P=2, Blur Var=5, P=4, Blur Var 3, and P=4, Blur Var=5.

All the estimated images shown in Figures 4.17 to 4.20(a-d) present a good visual quality. In the next sub-section we investigate the performance of the CSSR algorithm further to the case where only one input image is available.

4.5.1 CSSR from a single image

In this section, the performance of the CSSR algorithm is investigated when the input is a single image. Although it is not a normal case for such a problem, however, the CSSR can be adapted for this problem. Notice here that the problem is simpler since there are no registration parameters to be estimated, however, the performance is expected to be worse than when multiple input images are available. Tables 4.10 and 4.11 show the results obtained for the four test images.

To compare this with the multiple input case, with Q=4, we choose P=4, Blur Var=3, SNR=40 dB for all test images. The plots are shown in Figures 4.21 and 4.22. The plots show how increasing the input images can affect positively the estimated image quality. However, at very low ratios R, which are not practical to be adapted, a single image processing may, in some cases, give a better performance.

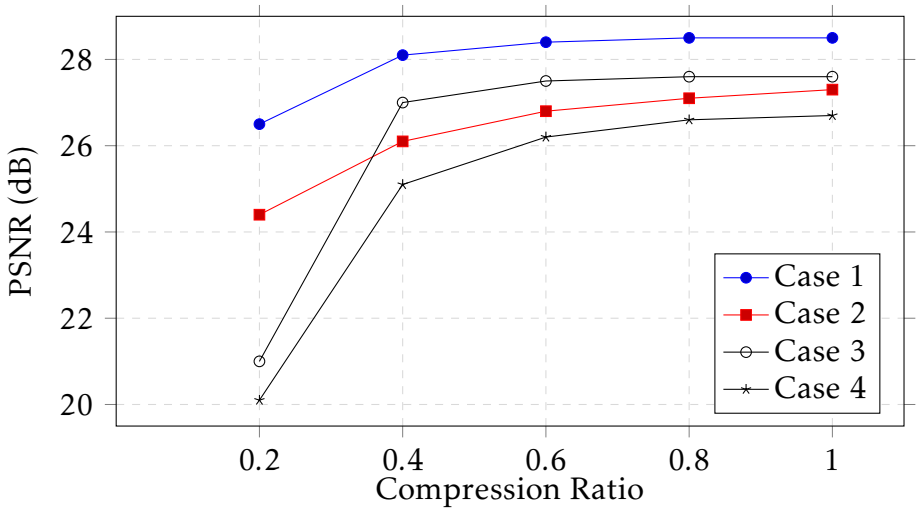

(a)

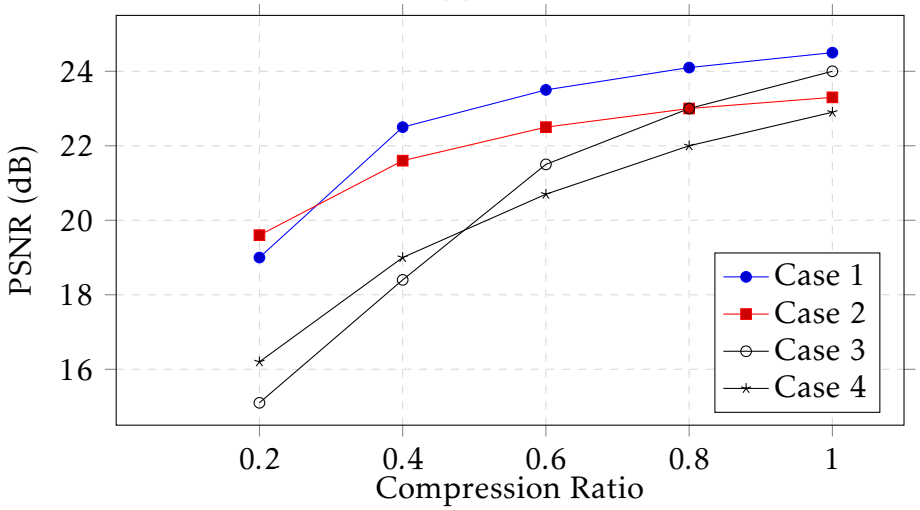

(b)

Figure 4.15: Performance of the CSSR algorithm (Q=4). Case 1: P=2, Blur Var=3, SNR=40 dB, Case 2: P=2, Blur Var=5, SNR=30 dB, Case 3: P=4, Blur Var=3, SNR=40 dB, Case 4: P=4, Blur Var=5, SNR=30 dB. (a) Satellite image, (b) Barbara image.

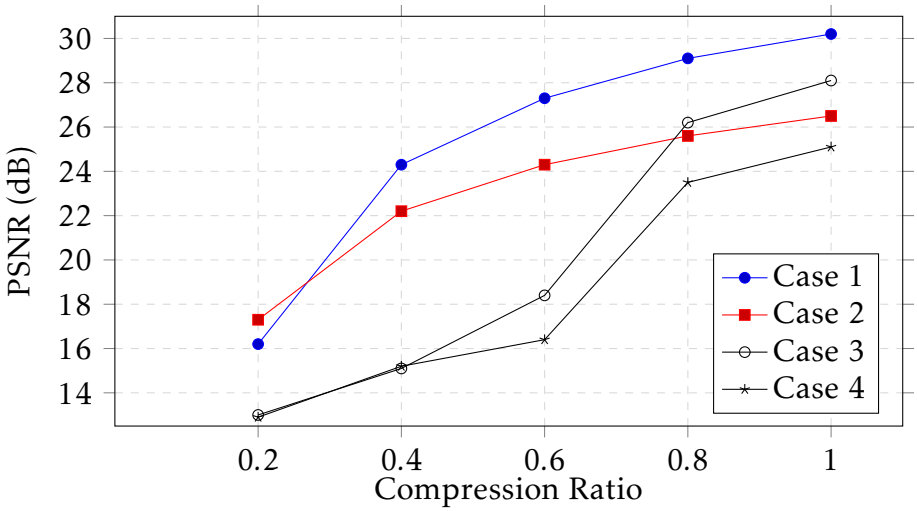

(a)

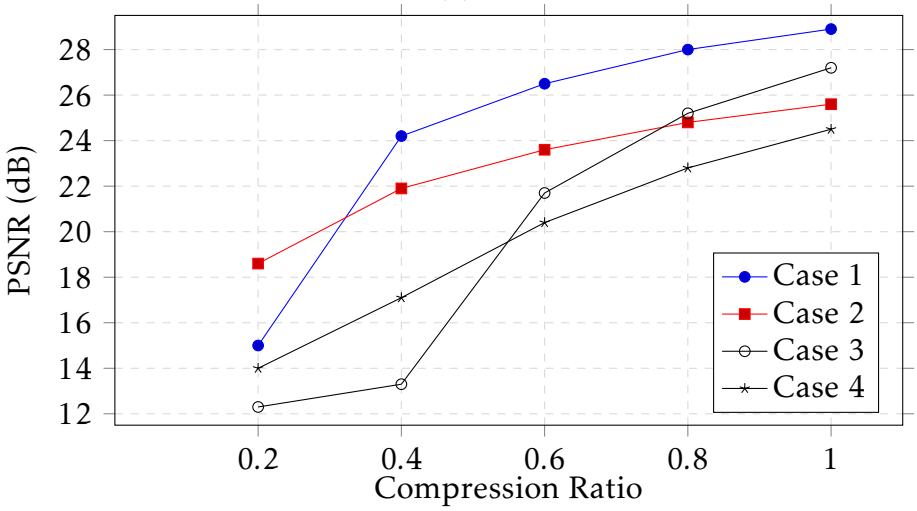

(b)

Figure 4.16: Performance of the CSSR algorithm (Q=4). Case 1: P=2, Blur Var=3, SNR=40 dB, Case 2: P=2, Blur Var=5, SNR=30 dB, Case 3: P=4, Blur Var=3, SNR=40 dB, Case 4: P=4, Blur Var=5, SNR=30 dB. (a) Peppers image, (b) Alhambra image

Table 4.10: Performance of the CSSR algorithm for the Satellite and Brabara images, using a single observation ($Q = 1$).

Blur Var			3		5		9	
SNR			40	30	40	30	40	30
Image	P	R	PSNR (dB)					
Satellite	2	0.2	25.3	23.7	24.9	23.5	24.4	23.1
		0.4	27.4	26.2	26.6	25.5	25.4	24.6
		0.6	27.9	27.1	26.9	26.2	25.7	25.2
		0.8	28.0	27.6	26.9	26.6	25.7	25.5
		1.0	28.0	27.7	27.0	26.7	25.7	25.6
	4	0.2	22.0	20.2	21.3	20.1	20.6	20.2
		0.4	25.7	24.5	25.3	24.1	24.5	23.5
		0.6	26.1	25.8	25.9	25.4	25.2	24.6
		0.8	26.1	26.1	26.0	25.8	25.3	25.0
		1.0	26.1	26.2	26.0	25.9	25.4	25.1
Barbara	2	0.2	18.5	18.6	18.5	18.3	18.5	18.0
		0.4	20.6	20.4	20.7	20.2	20.6	19.9
		0.6	22.4	21.8	22.3	21.5	22.0	21.1
		0.8	23.5	22.7	23.1	22.4	22.7	21.9
		1.0	24.1	23.3	23.5	22.7	23.0	22.4
	4	0.2	16.5	14.5	16.3	16.4	15.9	16.4
		0.4	18.4	15.5	17.9	17.9	17.6	18.0
		0.6	20.2	20.1	19.9	19.6	19.7	19.5
		0.8	22.1	21.5	21.6	21.3	21.4	21.0
		1.0	23.0	22.6	23.0	22.4	22.8	22.0

Table 4.11: Performance of the CSSR algorithm for the Peppers and Alhambra images, using a single observation ($Q = 1$).

Blur Var			3		5		9	
SNR			40	30	40	30	40	30
Image	P	R	PSNR (dB)					
Peppers	2	0.2	15.5	14.6	15.1	14.7	14.3	14.8
		0.4	18.5	16.1	18.1	16.2	21.0	19.7
		0.6	24.8	23.4	12.3	22.7	23.2	21.8
		0.8	27.3	25.2	26.1	24.3	24.6	23.0
		1.0	29.0	26.6	27.3	25.3	25.5	23.8
	4	0.2	14.2	12.7	13.3	12.8	12.5	13.1
		0.4	16.6	13.6	16.6	13.8	16.6	14.1
		0.6	19.5	14.5	19.4	14.7	17.8	15.0
		0.8	23.6	22.4	23.0	21.8	22.5	21.3
		1.0	25.6	24.4	25.5	23.9	24.7	22.9
Alhambra	2	0.2	15.1	15.6	17.6	15.7	17.6	16.8
		0.4	20.6	19.9	20.9	19.8	19.5	19.2
		0.6	23.7	22.3	23.4	21.8	22.4	21.0
		0.8	26.1	24.4	25.0	23.4	23.5	22.1
		1.0	27.5	25.7	25.9	24.4	24.0	22.9
	4	0.2	14.2	13.2	14.3	13.4	14.0	13.7
		0.4	16.4	16.6	16.3	16.4	16.3	16.5
		0.6	19.5	19.3	19.1	19.0	18.9	18.7
		0.8	22.1	21.5	21.7	21.1	21.4	20.6
		1.0	23.6	23.1	23.6	22.9	23.2	22.0

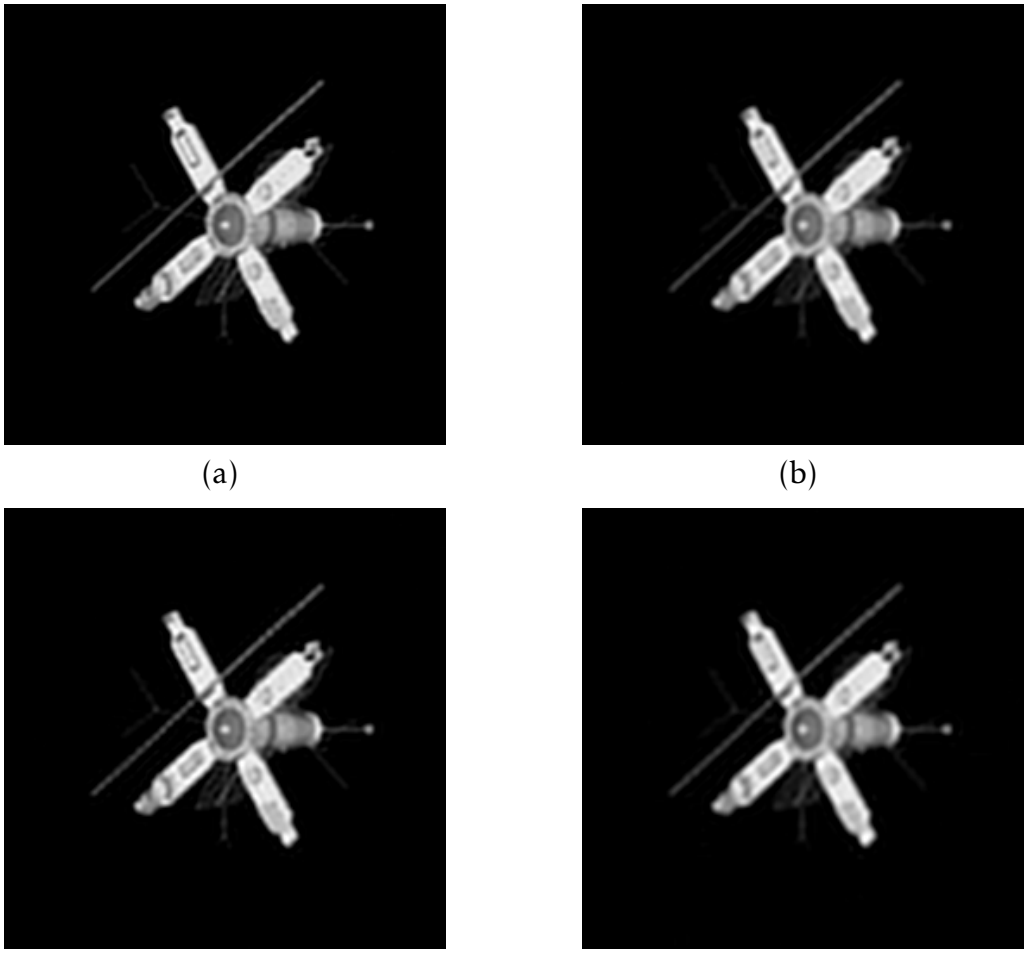

(a) (b)

(c) (d)

Figure 4.17: Estimated Satellite Images using the proposed CSSR method (R=0.8 and Q=5). (a) P=2, Blur Var=3, (b) P=2, Blur Var=5, (c) P=4, Blur Var=3, (d) P=4, Blur Var=5.

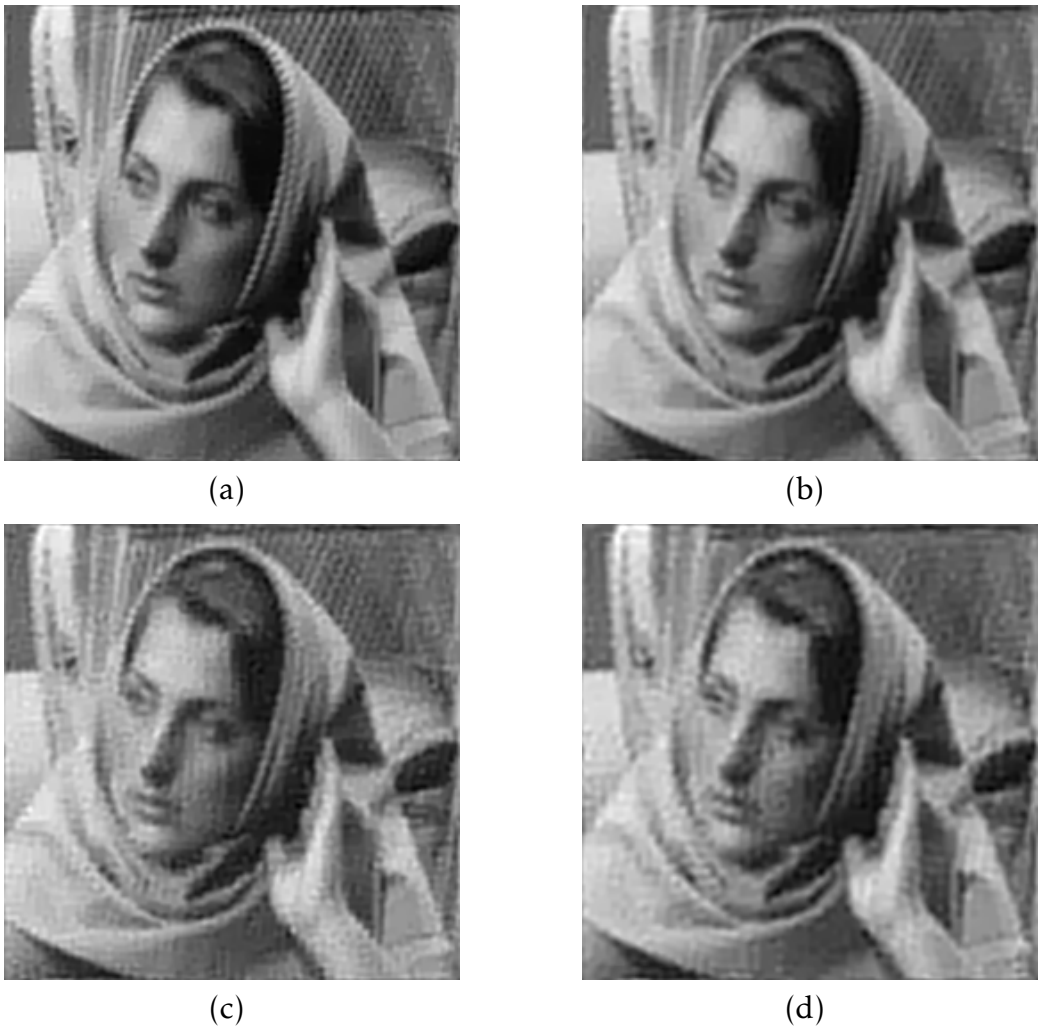

(a) (b)

(c) (d)

Figure 4.18: Estimated Barbara Images using the proposed CSSR method (R=0.8 and Q=5). (a) P=2, Blur Var=3, (b) P=2, Blur Var=5, (c) P=4, Blur Var=3, (d) P=4, Blur Var=5.

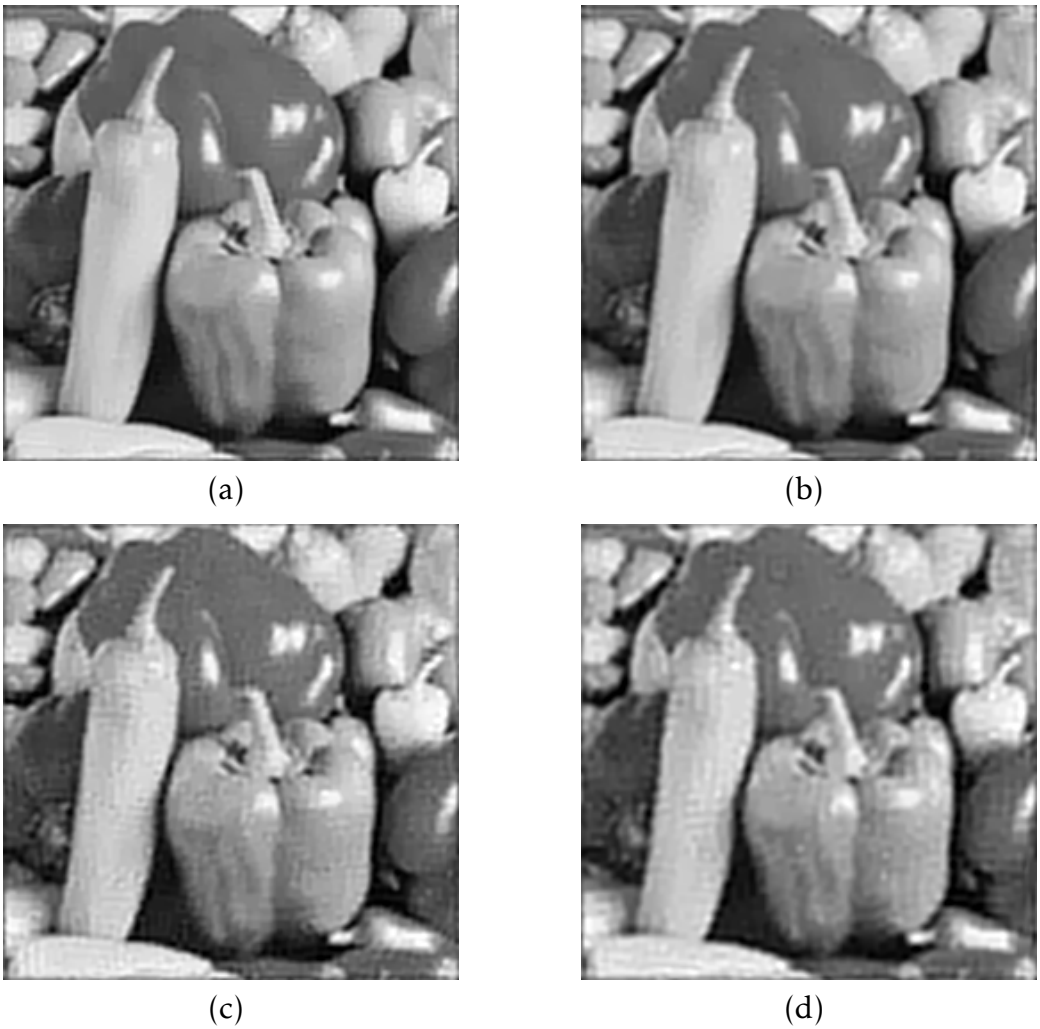

(a) (b)

(c) (d)

Figure 4.19: Estimated Peppers Images using the proposed CSSR method (R=0.8 and Q=5). (a) P=2, Blur Var=3, (b) P=2, Blur Var=5, (c) P=4, Blur Var=3, (d) P=4, Blur Var=5.

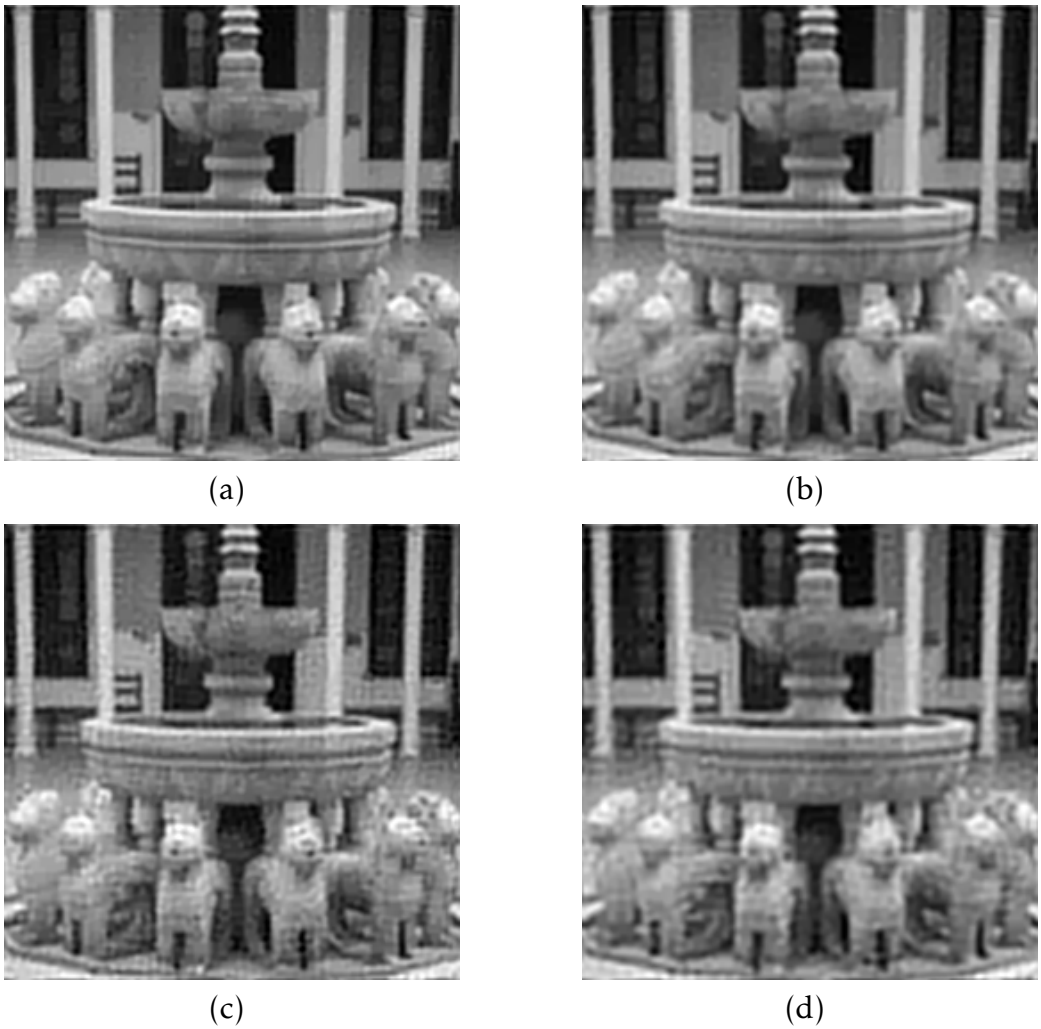

(a) (b)

(c) (d)

Figure 4.20: Estimated Alhambra Images using the proposed CSSR method (R=0.8 and Q=5). (a) P=2, Blur Var=3, (b) P=2, Blur Var=5, (c) P=4, Blur Var=3, (d) P=4, Blur Var=5.

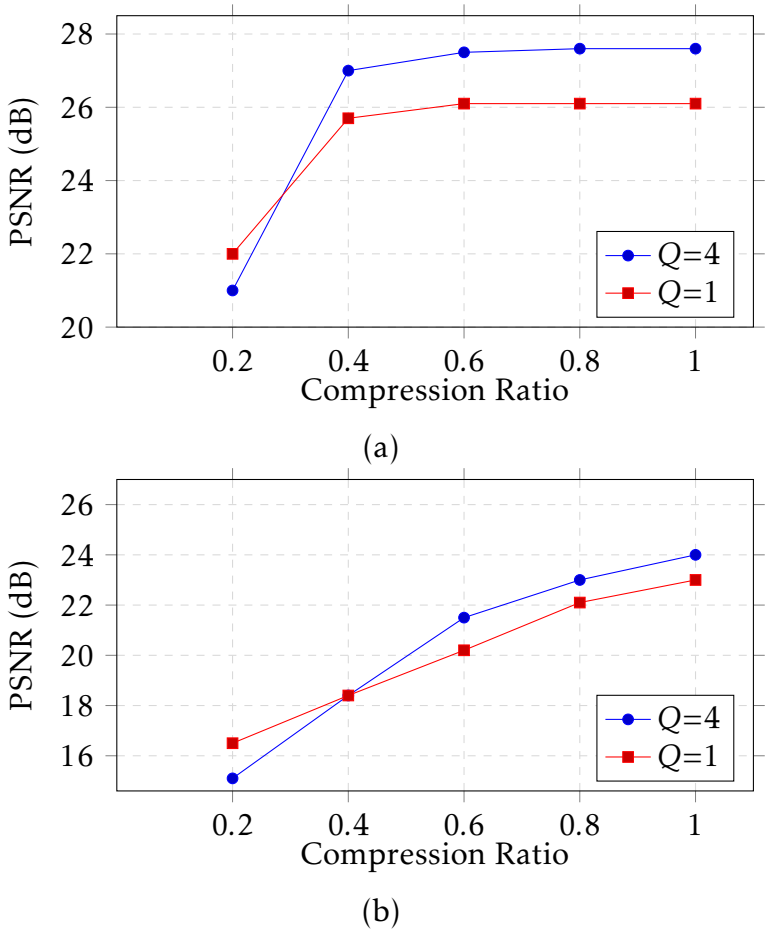

Figure 4.21: CSSR performance for multiple and single input images. (P=4, Blur Var=3, SNR=40 dB. on (a) Satellite, (b) Barbara.

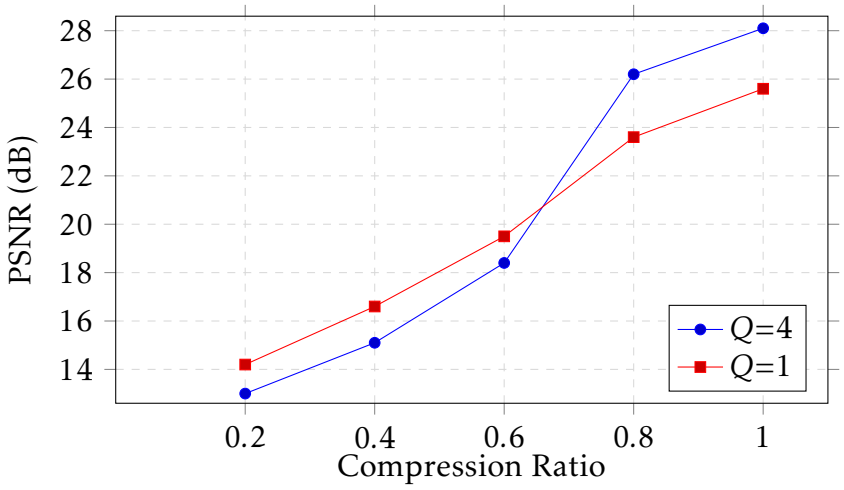

(a)

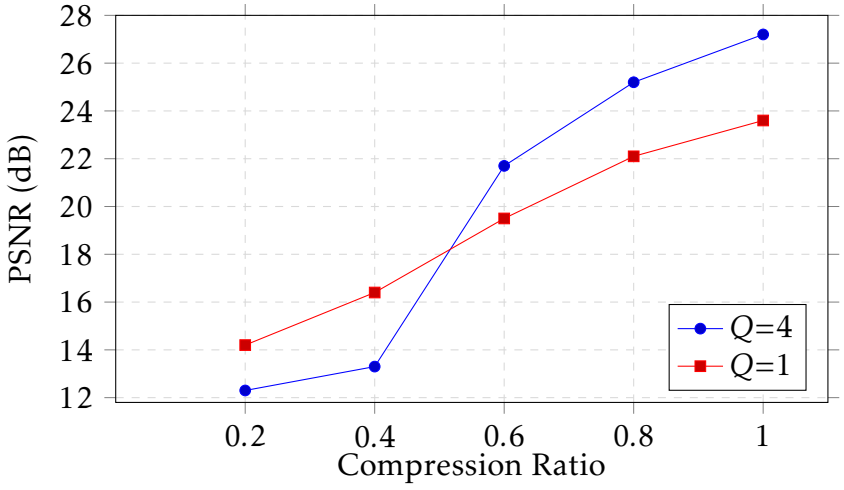

(b)

Figure 4.22: CSSR performance for multiple and single input images. (P=4, Blur Var=3, SNR=40 dB. on (a) Peppers, (b) Alhambra.

Table 4.12: Performance of the sequential approach using $Q = 4$.

Blur Var			3		5		9	
SNR			40	30	40	30	40	30
Image	P	R	PSNR (dB)					
Satellite	2	0.2	22.4	24.0	22.6	23.6	21.6	23.0
		0.4	26.0	26.2	25.6	25.5	24.4	24.6
		0.6	25.7	26.7	26.4	25.9	25.2	24.9
		0.8	27.6	26.9	26.7	26.0	25.5	25.0
		1.0	27.9	27.0	26.9	26.1	25.6	25.1
	4	0.2	17.4	19.1	17.2	18.8	16.6	18.5
		0.4	23.3	24.3	22.9	23.8	22.3	23.2
		0.6	26.2	25.4	25.5	24.8	24.4	24.1
		0.8	26.9	25.6	26.1	25.1	25.0	24.4
		1.0	27.1	25.6	26.4	25.1	25.3	24.4
Barbara	2	0.2	17.5	19.3	17.1	19.2	16.0	18.3
		0.4	20.0	21.4	19.7	21.2	18.9	20.7
		0.6	21.5	22.4	21.4	22.1	20.5	21.6
		0.8	22.6	22.9	22.4	22.6	21.6	22.1
		1.0	23.2	23.2	22.8	22.8	22.1	22.3
	4	0.2	15.0	15.3	15.1	15.2	14.1	15.2
		0.4	16.4	16.9	16.3	17.0	16.0	17.0
		0.6	18.7	17.7	18.8	17.8	18.5	17.8
		0.8	20.8	18.3	20.7	18.4	20.3	18.5
		1.0	22.3	18.5	22.0	18.6	21.4	18.6

4.5.2 CSSR vs Sequential Approach

As mentioned earlier, the alternate approach is expected to produce a better estimated image quality. The next experiment has been executed on both the Satellite and Barbara images. We used four simulated CS LR images to test the sequential and the CSSR alternate estimations. The obtained results are tabulated in Table 4.12, using Q=4 in all cases.

Figure 4.23 shows plots of the PSNR vs R, for the Satellite image, for the two approaches. P=4, for the two cases in Figure 4.23(a) Blur Var=5, SNR=30dB and Figure 4.23(b) Blur Var=3, SNR=40 dB. Similarly, Figure 4.24 shows the results obtained for the Barbara image, for the two approaches, under the same conditions. Again the plots show, as expected, how the alternate approach outperforms the sequential approach. In all cases the obtained PSNR using CSSR is better than when using the sequential approach. In the plots of the Satellite image in Figure 4.23(a) the alternate CSSR improves the PSNR by more than 1.2 dB when compared to the sequential approach for all Rs, while in Figure 4.24(a), the estimated Barbara image using CSSR has a 4 dB increment in PSNR compared to the sequential estimate, for the case when

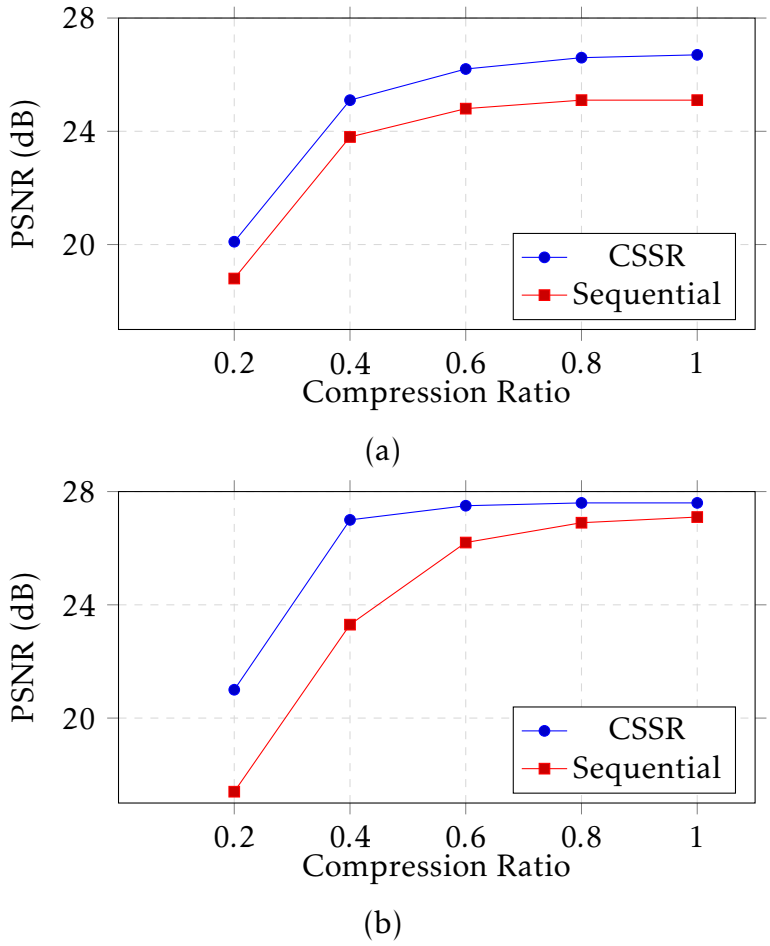

Figure 4.23: Comparison of the proposed CSSR vs the sequential approach for the Satellite image, (Q=4, P=4), using (a) Blur Var=5, SNR=30 dB, (b) Blur Var=3, SNR=40 dB.

R=1, Blur Var=5, and SNR=30 dB.

4.5.3 CSSR1 vs CSSR2

Now in this sub-section the performance is tested for two different registration approaches. To distinguish the two used approaches, we denote by CSSR1 the one using App3 applying Equation (3.41), and CSSR2 the App4 approach using Equation (3.51). Tables 4.13 and 4.14 show the obtained results for both the Satellite and Barbara images, we used Q=4 in all experiments.

Figure 4.25 shows the plots for the Satellite image (using P=4 and Q=4). Figure 4.25(a) analyzes the case when Blur Var=5 and SNR=30 dB, while Figure 4.25(b) analyzes the case when Blur Var=3, SNR=40 dB. Similarly, Figure 4.26 shows the plots for the Barbara image (P=4 and Q=4): Figure 4.26(a) for the case when Blur Var=5 and SNR=30 dB, and Figure 4.26(b) for the case when Blur Var=3, SNR=40 dB. This proves that the two registration approaches are

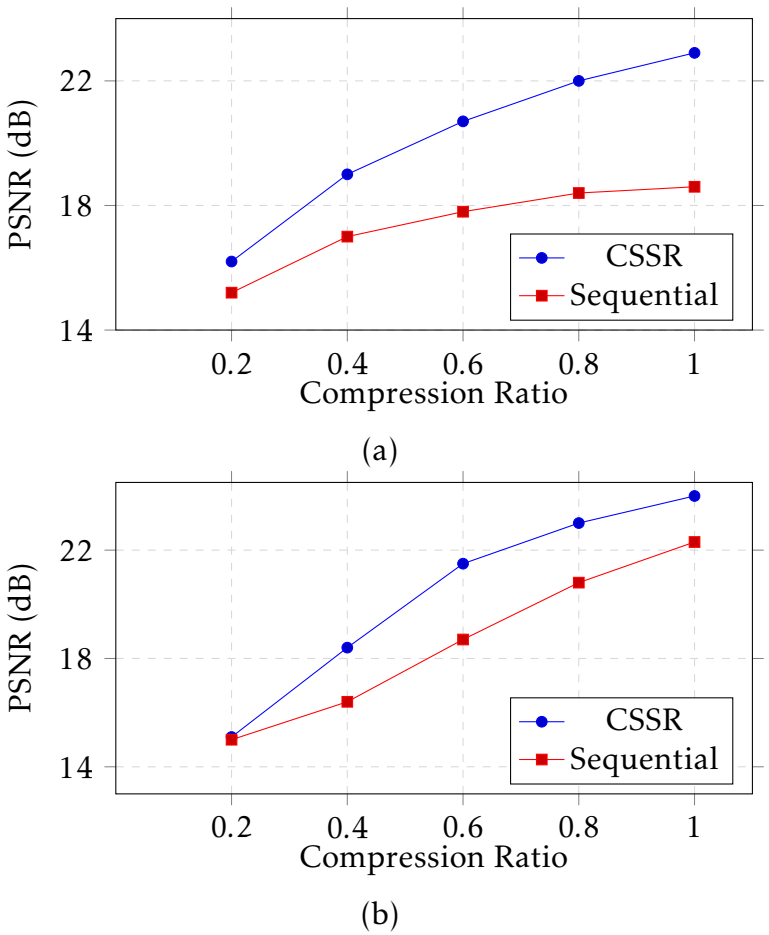

Figure 4.24: Comparison of the proposed CSSR vs the sequential approach for the Barbara image, (Q=4, P=4), using (a) Blur Var=5, SNR=30 dB, (b) Blur Var=3, SNR=40 dB.

Table 4.13: Comparison of CSSR1 vs CSSR2 algorithms for the Satellite image, using $Q = 4$.

Blur Var			3		5		9	
SNR			40	30	40	30	40	30
P	Alg	R	PSNR (dB)					
2	CSSR1	0.2	26.5	24.9	26.0	24.4	24.9	23.8
		0.4	28.1	26.9	27.1	26.1	25.8	25.1
		0.6	28.4	27.7	27.3	26.8	26.0	25.7
		0.8	28.5	28.1	27.4	27.1	26.1	25.9
		1.0	28.5	28.3	27.4	27.3	26.1	26.0
	CSSR2	0.2	26.5	24.9	26.0	24.4	24.9	23.8
		0.4	28.1	26.9	27.1	26.1	25.8	25.1
		0.6	28.4	27.7	27.3	26.8	26.0	25.7
		0.8	28.5	28.1	27.4	27.1	26.1	25.9
		1.0	28.5	28.3	27.4	27.3	26.1	26.6
4	CSSR1	0.2	21.0	20.7	20.9	20.1	20.1	19.7
		0.4	27.0	25.8	26.3	25.1	25.3	24.2
		0.6	27.5	27.0	26.7	26.2	25.6	25.1
		0.8	27.6	27.3	26.8	26.6	25.7	25.5
		1.0	27.6	27.4	26.8	26.7	25.8	25.6
	CSSR2	0.2	21.0	20.7	20.8	20.1	20.1	19.6
		0.4	27.0	25.8	26.3	25.1	25.3	24.2
		0.6	27.5	27.0	26.7	26.2	25.6	25.1
		0.8	27.6	27.3	26.8	26.6	25.7	25.5
		1.0	27.6	27.5	26.8	26.7	25.8	25.6

Table 4.14: Comparison of CSSR1 and CSSR2 algorithms for the Barbara image, using $Q = 4$.

Blur Var			3		5		9	
SNR			40	30	40	30	40	30
P	Alg	R	PSNR (dB)					
2	CSSR1	0.2	19.0	19.5	19.7	19.6	19.1	18.7
		0.4	22.5	21.9	22.2	21.6	21.7	21.2
		0.6	23.5	22.8	23.2	22.5	22.7	22.1
		0.8	24.1	23.4	23.6	23.0	23.1	22.5
		1.0	24.5	23.8	23.9	23.3	23.3	22.8
	CSSR2	0.2	19.9	19.8	19.7	19.6	19.0	18.7
		0.4	22.5	21.8	22.2	21.6	21.7	21.2
		0.6	23.6	22.8	23.2	22.5	22.7	22.1
		0.8	24.1	23.4	23.6	23.0	23.1	22.5
		1.0	24.5	23.8	23.9	23.3	23.3	22.8
4	CSSR1	0.2	15.1	15.3	15.7	16.2	15.3	15.9
		0.4	18.4	19.0	18.0	19.0	18.0	18.8
		0.6	21.5	20.7	21.6	20.7	21.3	20.2
		0.8	23.0	22.2	22.9	22.0	22.6	21.6
		1.0	24.0	23.2	23.5	22.9	23.1	22.4
	CSSR2	0.2	15.0	15.3	15.7	16.2	15.3	15.9
		0.4	18.4	19.0	18.0	19.0	18.0	18.7
		0.6	21.5	20.7	21.6	20.7	21.3	20.2
		0.8	23.1	22.2	22.9	22.0	22.6	21.6
		1.0	24.0	23.2	23.5	22.9	23.1	22.4

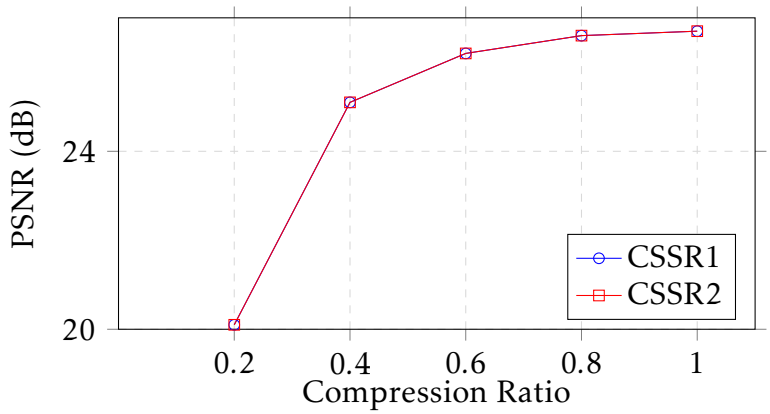

(a)

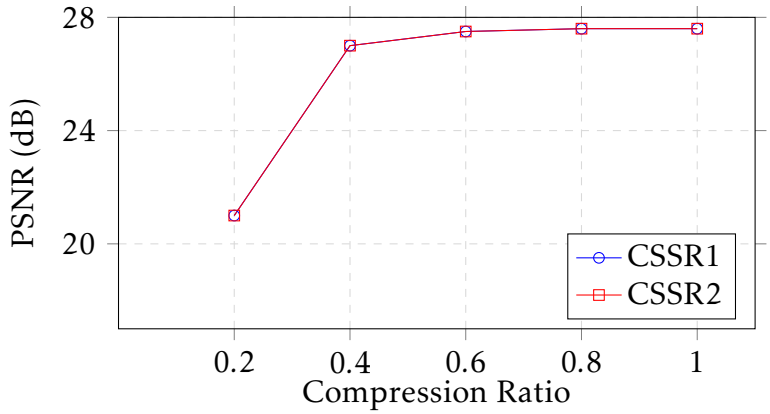

(b)

Figure 4.25: Comparison of the proposed CSSR1 vs CSSR2 for the Satellite image, (Q=4, P=4), using (a) Blur Var=5, SNR=30 dB, (b) Blur Var=3, SNR=40 dB.

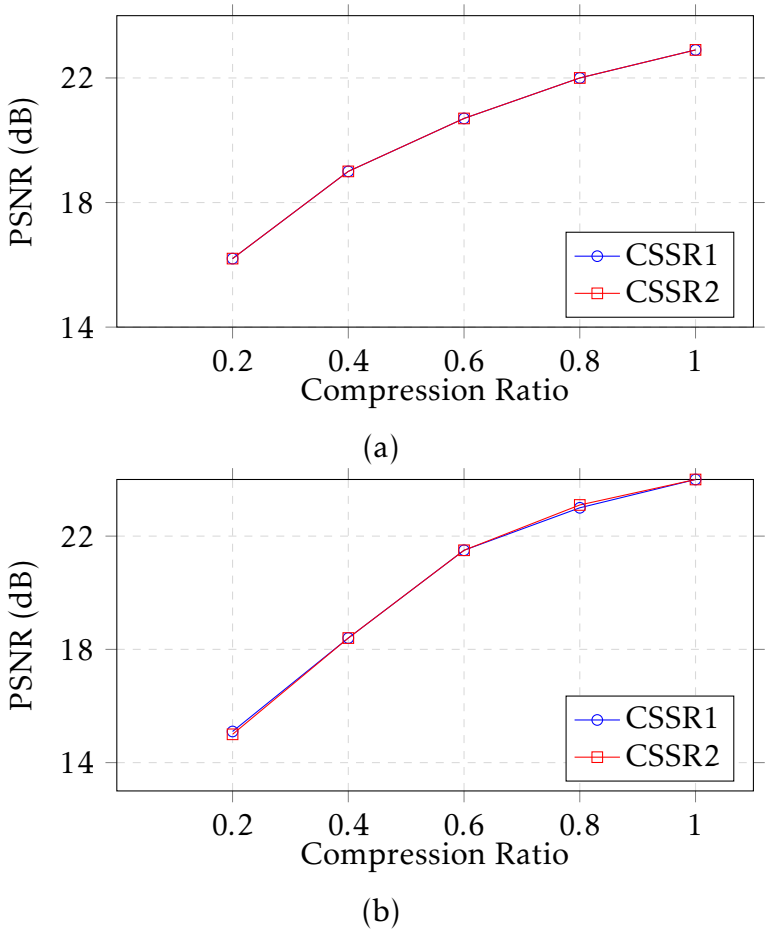

Figure 4.26: Comparison of the proposed CSSR1 vs CSSR2 algorithms for the Barbara image, (Q=4, P=4), using (a) Blur Var=5, SNR=30 dB, (b) Blur Var=3, SNR=40 dB.

effective and accurate and can be adopted interchangeably. This is clear in the plots where the curves coincide.

Experimental results were performed on additional simulated and real images in our published works [18–20].

4.6 CSSR of PMMW Images

Due to their characteristics, Millimeter Wave (MMW) images are used in applications like weather operations, low visibility navigation, and the imaging of people for concealed object and threat detection [4, 90, 91], just to name a few.

Based on their interest, image processing techniques have recently started to be applied to these images. For instance, Passive Millimeter Wave (PMMW) image enhancement has been addressed in [90, 92–95] to perform detection tasks. In [93] the high frequency components of those images were restored using a MAP estimator, and they were then added to the input image to produce an HR image. Registration and fusion of visible and MM images as well as segmentation of MMW images have been addressed in [90, 94, 95].

Unfortunately PMMW systems have two serious shortcomings: the long acquisition time needed to produce a PMMW image and the poor resolution of captured images. CS systems, with its reduced image acquisition time, have been applied to PMMW imaging, see[55, 56, 96, 97]. In [96, 97] the authors utilize Hadamard masks to reduce the acquisition time in PMMW imagers. In [98] a PMMW imaging system with extended depth-of-field that can produce images with reduced number of samples is presented. CS and Blind Image Deconvolution have been combined in [5]. By and large the resolution of MMW images is small, therefore making their analysis a challenging task.

In our works [18, 20] HR images were super resolved for the first time from multiple CS observations of unregistered LR PMMW images. We believe that PMMW images represent an important application area where CS and LR to HR techniques can be combined to enhance the performance of related application capabilities of current PMMW imaging systems.

Let us next present the obtained experimental results performed on real input images, acquired by a PMMW imager. These images were synthetically compressed using a circulant Toeplitz matrix, to serve as a measurement matrix, following the Bernoulli probability distribution.

In the first experiment, four real PMMW images of a person were acquired, shown in Figure 4.27(a). The estimated image using bilinear interpolation from one reconstructed LR image is shown in Figure 4.27(b), and the estimated using CSSR is shown in Figure 4.27(c), both using P=2, R=1.

In the second experiment we used four images, shown in Figure 4.28(a), of a man free of threats. These images were synthetically compressed with R=0.8. The interpolated version of one reconstructed image is shown in Figure 4.28(b), while the estimated image using the CSSR algorithm is shown in Figure 4.28(c), both using P=2. Notice here that the interpolated image shows, by error, a cut near the hand, which means that the man has a threat attached to him, which is not the case. This is clear in the estimated image using CSSR which shows the continuity near the left hand.

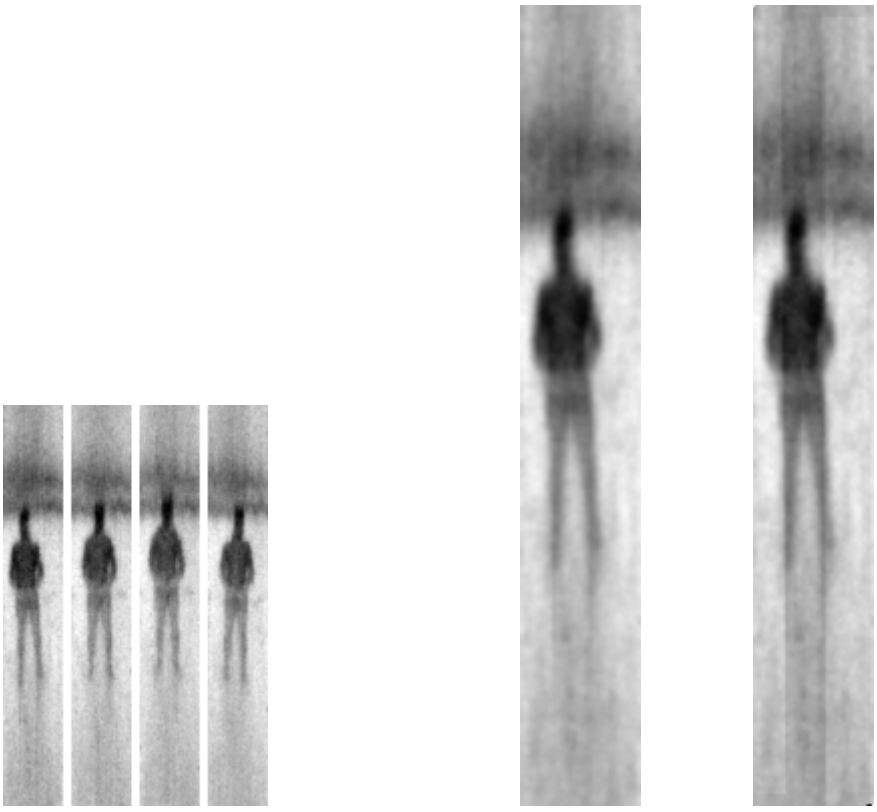

(a) (b) (c)

Figure 4.27: PMMW image of a man free of threats (Q=4, R=1, P=2).(a) Four noisy real observations, (b) Bilinear interpolation from one reconstructed LR image, (c) Estimated image using CSSR algorithm.

(a) (b) (c)

Figure 4.28: PMMW image of a man free of threats (Q=4, R=0.8, P=2) (a) Four noisy real observations, (b) Bilinear interpolation from one reconstructed LR image, (c) Estimated image using CSSR algorithm.

The next experiment used four real PMMW LR observations, of a man hiding a threat attached to his left arm, as shown in Figure 4.29(a). The estimated HR image using bilinear interpolation of one reconstructed LR image, is shown in Figure 4.29(b), and the estimated using the CSSR algorithm, with Q=4, is shown in Figure 4.29(c), using P=2, R=0.8. Also, the corresponding estimated images using P=4, R=0.8 are shown in Figure 4.29(d) for bilinear interpolation, and Figure 4.29(e) for the CSSR algorithm. The obtained images clearly show the better reconstruction capabilities of the proposed method, this can be observed by the clear discontinuity of the arm indicating the attached threat.

The next experiment uses seven real PMMW images of a man with a threat attached to his chest. The seven images, four of which are shown in Figure 4.30(a), were synthetically compressed using R=0.8, then used to estimate the image shown in Figure 4.30(c) using P=2. This result can be compared with the interpolated image from one reconstructed image in Figure 4.30(d).

4.7 CCSSR of Color Images

There is no much work dealing with color images from CS observations. [99] proposed a method for color imaging via compressed sensing. It works on the color channels and random projections from each channel, RGB, are acquired separately. The reconstruction process makes use of the correlation between the three color channels and it is based on group sparse optimization.

In [100], the single-pixel CS camera has been combined with a Bayer color filter to acquire CS color images, then joint sparsity models were applied to recover the three RGB channels. [65] estimated SR images from a single LR CS observation and applied this to color images. In [58] spatial multiplexing cameras were used to sample the scene through a series of coded projections, this was applied to CS video super resolution and color videos.

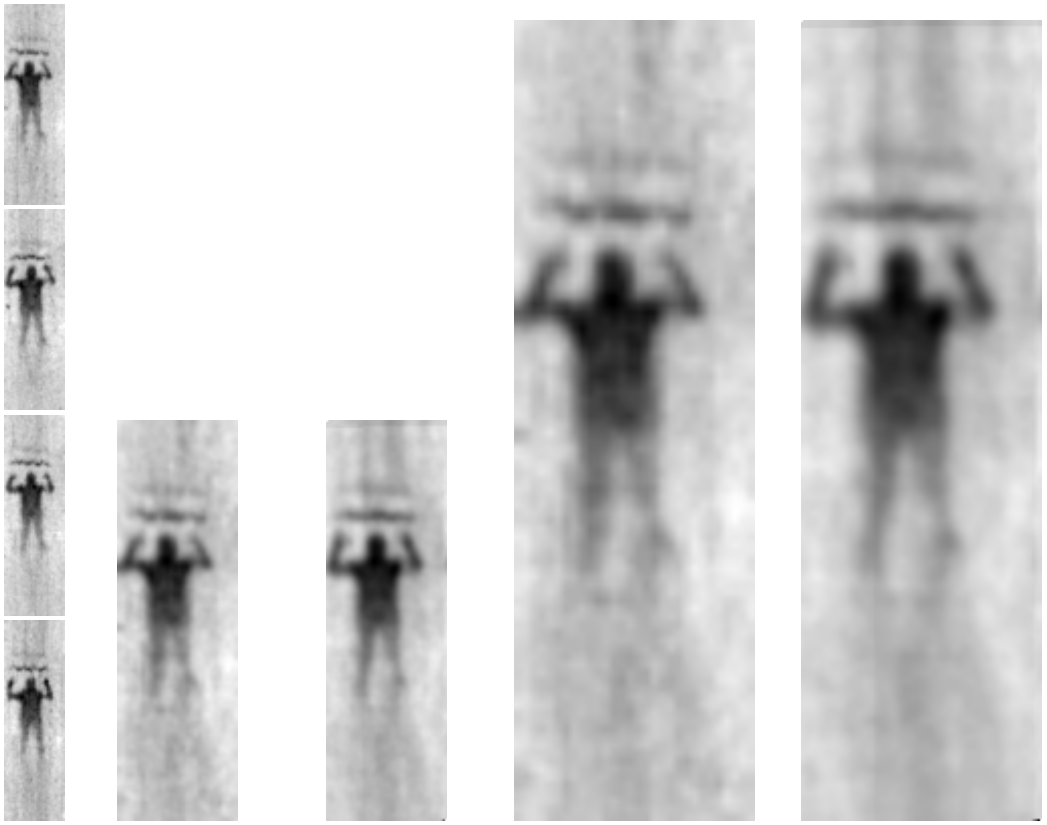

(a) (b) (c) (d) (e)

Figure 4.29: PMMW image of a man with a threat attached to his arm (Q=4, R=0.8). (a) LR images, (b) Bilinear interpolation from one reconstructed image, P=2, (c) Estimated HR image using the CSSR algorithm, P=2, (d) Bilinear interpolation from one reconstructed image, P=4, (e) Estimated HR image using the CSSR algorithm, P=4.

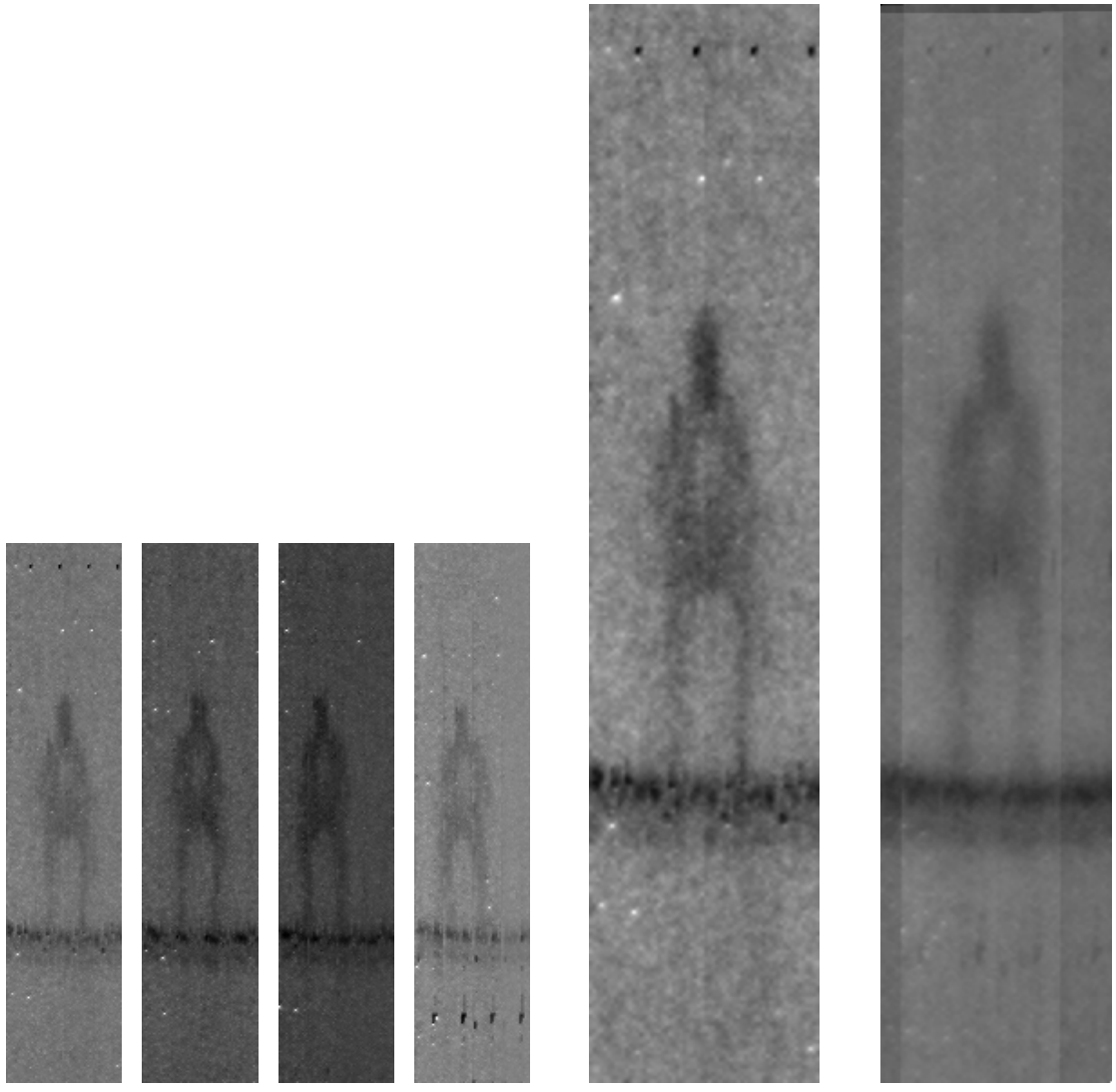

Figure 4.30: PMMW image of a man with a threat attached to his chest (Q=7, R=0.8, P=2). (a) LR images, (b) Bilinear interpolation from one reconstructed LR image, (c) Estimated HR image using the CSSR algorithm.

Next we present experimental results obtained using the proposed CCSSR algorithm, as an important application of the CSSR paradigm to color images. The experiments were performed using both simulated and synthetically CS real color input images. We carried out a set of experiments on the images shown in Figures 4.31(a-c): Barbara, Lena, and Peppers images. The images have been warped, then degraded by Gaussian blurs of different known variances and down-sampled. The LR RGB channels have been compressed separately using a circulant Toeplitz matrix following the Bernoulli probability distribution. White Gaussian noise, with SNR=40 dB, has been finally added to the compressed channels.

Figures 4.31(d,e) show, respectively, examples of a simulated LR and a CS-LR observation for the Barbara image using motion vector $\mathbf{s} = [.1222, -2, 3]^t$, blur variance 7, P= 2 and R=0.5. We used a 3-level Haar wavelet transform as the transform basis W, and Peak Signal to Noise Ratio (PSNR) as the performance measure. The stopping criterion used was

$$\frac{norm(\mathbf{x}^k - \mathbf{x}^{k-1})}{norm(\mathbf{x}^{k-1})} \leq 10^{-3} \tag{4.4}$$

In the first experiment Q=3 observations and a zooming factor P=1 have been used in order to compare our method with the following CS reconstruction methods: Nagesh et. al [99] (Na) , Wakin et al [101] (Wa), Angshul L2,1 (L1), L2,0.4 (L4), and SL2,0 (SL)[99]. Results are tabulated in Table 4.15. Figure 4.32 shows a comparison between the results obtained using these CS algorithms and the obtained using our proposed CCSSR algorithm, where PSNR vs R curves are shown for the Lena image using P=1.0 and Q=3.

Table 4.15: Comparison of CS algorithms with the proposed CCSSR algorithm for CCSSR P=1.0, Q=3. In bold blue are the highest PSNR values.

Image	Alg	Na	Wa	L1	L4	SL	CCSSR
	R	PSNR Values (dB)					
Barbara	.1	25.1	24.8	26.1	**26.7**	26.5	21.3
	.2	27.1	26.6	28.0	28.5	28.3	**29.9**
	.3	28.8	27.9	29.3	30.0	29.7	**34.0**
Lena	.1	26.1	25.9	27.0	**27.6**	27.5	25.8
	.2	28.3	27.7	29.0	29.7	29.5	**31.6**
	.3	30.0	29.2	30.7	31.7	31.1	**37.0**
Peppers	.1	25.0	24.5	25.6	**26.3**	26.0	24.8
	.2	27.1	26.1	27.9	28.5	28.1	**32.5**
	.3	29.8	28.1	30.5	21.4	30.9	**35.2**

In the second experiment we investigate the performance of the proposed CCSSR algorithm for practical P and R values. For all images we used Gaussian blur of variance 5, SNR=40dB, and Q=3. The results are tabulated in Table 4.16 for P=2 and 4. Shown in Figure 4.33(a,b) are curves of the PSNR vs R for the three images used in our study, for the cases P=2 and P=4, respectively.

(a)

(b)

(c)

(d)

(e)

Figure 4.31: Original Images (a) Barbara, (b) Lena, and (c) Peppers. (d) Simulated LR Barbara image ($\mathbf{s} = [.1222, -2, 3]^t$, blur variance 7, P=2), (e) simulated CS observation (R=0.5, SNR=40 dB). The black line represents the added zero-valued entries to illustrate a square image.

The reconstructed Peppers images are shown in Figures 4.34(a,b), using R=0.6, Blur Var=5, SNR=40dB, and Q=3, for the two cases P=2 and P=4, respectively.

In the third experiment we use real LR images of a toy, which have been synthetically compressed using R=0.8. We used a 16 input image sequence to reconstruct the HR image, with P=2, shown in Figure 4.35(d), while Figure 4.35(c) shows the reconstructed image obtained using only the first 4 input images of the previous sequence, shown in Figure 4.35(a). Figure 4.35(b) shows an interpolated image from the first reconstructed LR image.

The next experiment is similar to the third and uses real images of a car. Figures 4.36(c,d) show the results obtained using CCSSR for respectively 4 and 16 CS observations from a sequence of 16 input images whose first 4 images are shown in Figure 4.36(a). Figure 4.36(b) shows an interpolated image. We used P=2 in this experiment.

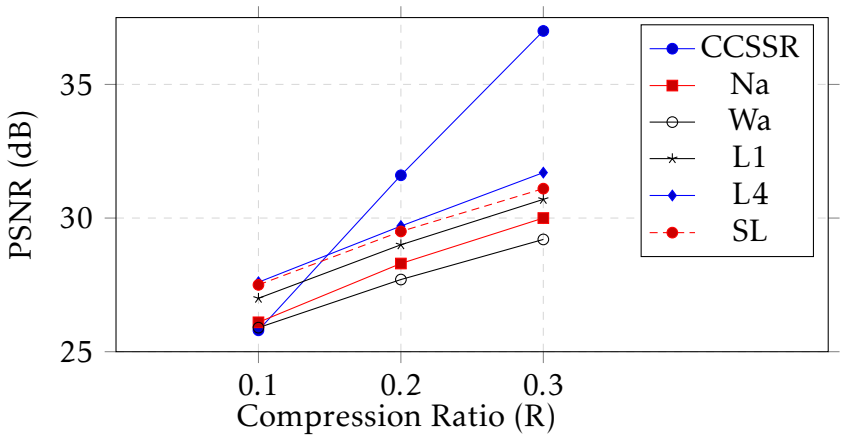

Figure 4.32: Comparison between CS algorithms and the CCSSR algorithm for the Lena image. For CCSSR, P=1, Q=3.

Table 4.16: CCSSR algorithm vs R (blur var 5, SNR=40dB, and Q=3).

Image	R	0.2	0.4	0.6	0.8	1.0
	P	PSNR Values (dB)				
Barbara	2	22.4	26.5	28.1	28.9	29.5
	4	16.6	20.7	25.6	27.2	28.1
Lena	2	23.3	28.4	29.9	30.4	30.6
	4	17.5	21.4	26.9	28.5	29.0
Peppers	2	23.0	27.0	28.7	29.4	29.9
	4	15.6	22.9	26.2	27.6	28.5

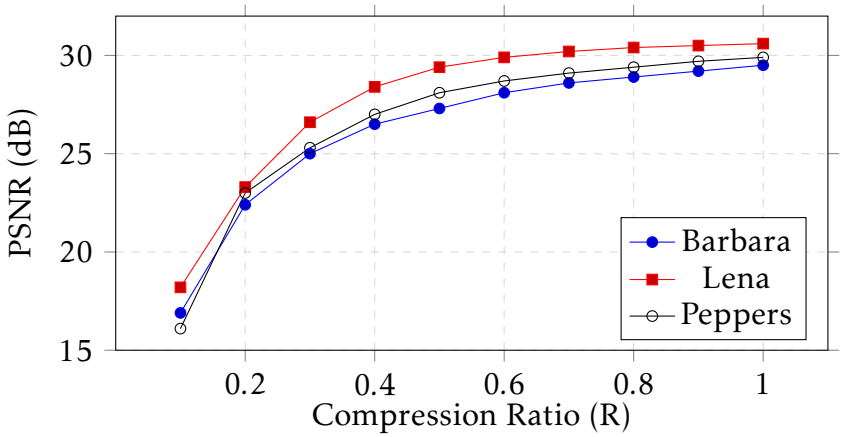

(a)

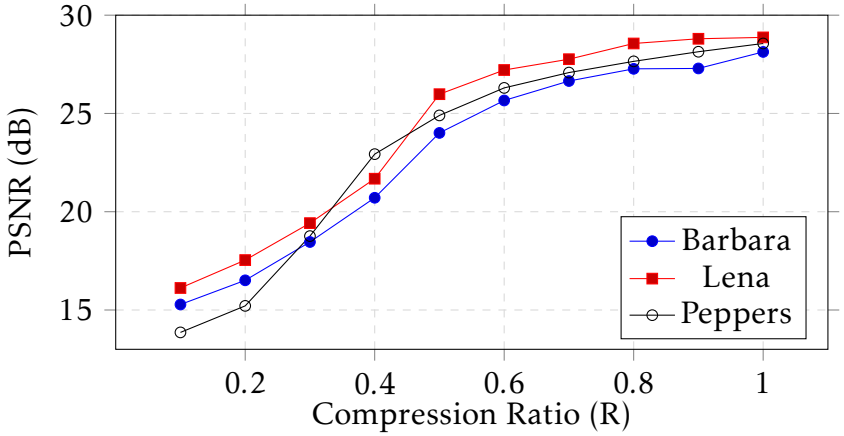

(b)

Figure 4.33: Performance of the proposed CCSSR vs R. Blur Var=5, SNR=40dB, Q=3. (a) P=2, (b) P=4.

(a) (b)

Figure 4.34: Reconstructed Peppers Images using the CCSSR algorithm. R=0.6, Blur Var=5, SNR=40dB, and Q=3. (a) P=2, (b) P=4,

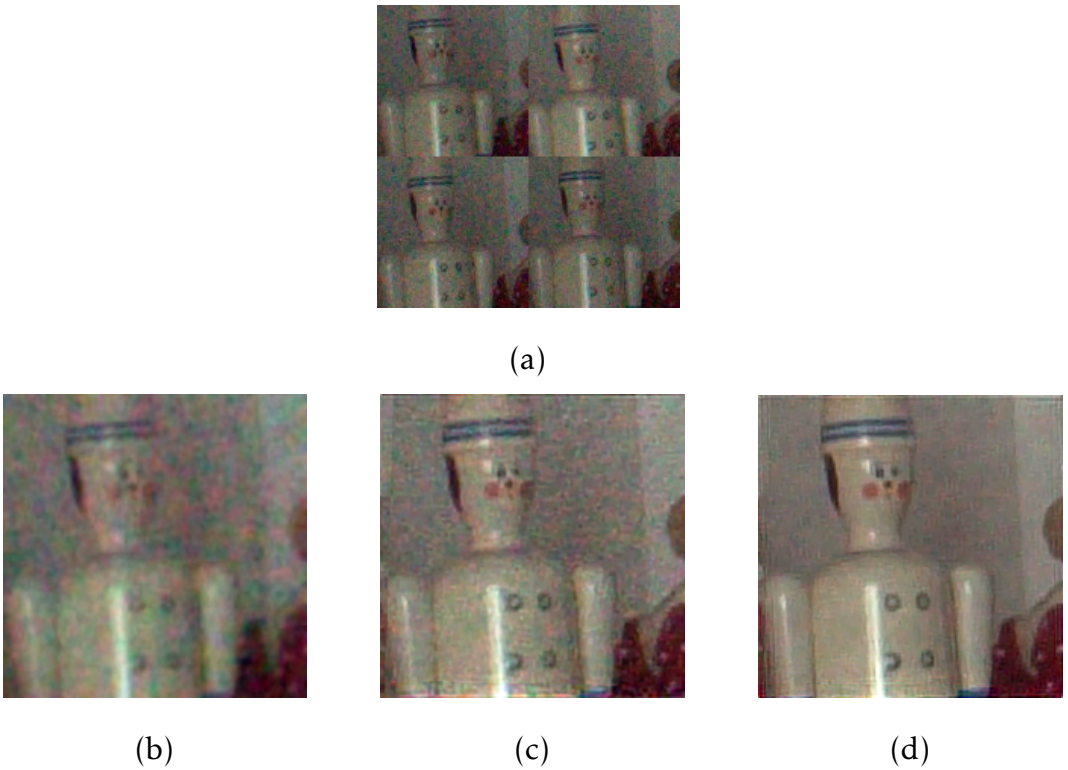

(a)

(b) (c) (d)

Figure 4.35: Image super resolution from real observations, R=0.8, P=2. (a) First 4 LR images (b) Bilinear interpolation of one reconstructed LR image, (c) Estimated HR image using the CCSSR algorithm, with Q=4, (d) Estimated HR image using the CCSSR algorithm, with Q=16.

(a)

(b)

(c)

(d)

Figure 4.36: Image super resolution from real observations, R=0.8, P=2. (a) First 4 LR images (b) Bilinear interpolation of one reconstructed LR image, (c) Estimated HR image using the CCSSR algorithm, with Q=4, (d) Estimated HR image using the CCSSR algorithm, with Q=16.

Chapter 5

Conclusions and Future Work

5.1 Conclusions

In this dissertation we have proposed a novel framework to reconstruct SR images from multiple unregistered LR images acquired using CS techniques. Any classical SR and/or CS techniques can be incorporated in the developed methodology. The degradation model of this novel combined problem has been modeled and a CSSR approach has been proposed in this work.

The CSSR method lowers the sampling frequency, transmission rates, the bandwidth of the image signal, and the memory requirements to store and/or send the image. Moreover, the acquisition time can be lowered, which is very important in medical and PMMW imaging applications. The enhanced SR image quality is advantageous in pattern recognition, medical diagnostics, and to emphasize a specific area of an image in surveillance cameras and satellite applications.

The proposed HR reconstruction uses a new robust sparsity promoting prior and solves a linear equation in $\mathbf{x}$ (the HR image), using conjugate gradient method. The transformed coefficient vector estimation is an ℓ_1 norm subject to a quadratic term optimization problem. The registration parameters can be estimated using four different procedures, to finally obtain accurate results, since any SR estimation process is highly dependent on the performance of the registration estimation step. The parameters can be estimated from the estimated HR image, or the LR images themselves, with the estimation from reconstructed LR images being less sensitive to the initial conditions. Furthermore we found that the estimation at LR level results in better quality of the reconstructed image.

The proposed optimization framework uses ADMM to jointly estimate all the unknowns including HR image, LR images, and registration parameters. We have experimentally shown that this simultaneous reconstruction outperforms the sequential method, that first performs LR reconstruction to then obtain an HR image from a set of LR observations. The sequential approach estimates every unknown just once, while the alternate approach iteratively updates the estimated unknowns. The better performance of the alternate approach is due to the additional information provided during the estimation process.

We also showed experimentally the enhancement obtained due to the multiple input images when compared with a single one. This is expected due to the additional information every input image provides. However, the multiplicity necessitates accurate registration estimation procedure which inherently affects the overall process.

The proposed framework has been tested and compared, at a unity compression ratio, with state-of-the-art SR algorithms which do not use compression in their work. It has also been compared, at a unity zooming factor, with state-of-the-art ID algorithms that deblur CS images, which do not use down-sampling in their work. Both comparisons used synthetic images and showed better performance of the proposed CSSR over others. The performance of CSSR when using practical values of P and R has also been tested and analyzed.

Besides, the CSSR effectiveness has been demonstrated experimentally on synthetically CS noisy real images. This represents the practical application of the CSSR method, which showed very good results.

The proposed CSSR method has been tested on PMMW images. These images usually have poor quality and limited resolution, which makes super resolving them a challenging task and is a hard test of the CSSR approach. The CSSR could be used to improve the quality of PMMW images. This is expected to improve threat detection rates, which is an expected field of future research. Notice here that the nature of PMMWI is similar to astronomical and medical images, and the good performance of the proposed CSSR algorithm can be extended to these images.

The proposed approach can also be applied to true color CS images. The separately sensed channels are utilized in a joint registration estimation to effectively and accurately estimate registration parameters for the three channels. The obtained results present an excellent image quality, even better than the obtained using previous CS reconstruction methods which correlate the color channels.

5.2 Future work

We finally comment on few areas of interest where we plan to continue our work on Compressed Sensing applied to LR images.

- To formulate the CSSR using Bayesian modeling and inference. This will allow us to estimate all the model parameters in an automatic manner.
- To include the estimation of the blur in the CSSR problem.
- To use image priors which cannot be formulated as super Gaussian distributions.
- To apply the developed framework to video sequences.
- To apply the proposed framework to images which are observed using the Bayer pattern.

Bibliography

[1] Chris Solomon and Toby Breckon. *Fundamentals of Digital Image Processing: A practical approach with examples in Matlab*. John Wiley & Sons, 2011.

[2] Sung Cheol Park, Min Kyu Park, and Moon Gi Kang. Super-resolution image reconstruction: a technical overview. *Signal Processing Magazine, IEEE*, 20(3):21–36, 2003.

[3] Peyman Milanfar. *Super-resolution imaging*. CRC Press, 2010.

[4] L. Yujiri, M. Shoucri, and P. Moffa. Passive millimeter wave imaging. *Microwave Magazine, IEEE*, 4(3):39–50, Sept 2003.

[5] B. Amizic, L. Spinoulas, R. Molina, and A.K. Katsaggelos. Compressive blind image deconvolution. *Image Processing, IEEE Transactions on*, 22(10):3994–4006, Oct 2013.

[6] Aggelos K Katsaggelos, Rafael Molina, and Javier Mateos. Super resolution of images and video. *Synthesis Lectures on Image, Video, and Multimedia Processing*, 1(1):1–134, 2007.

[7] Filip Šroubek and Jan Flusser. Multichannel blind iterative image restoration. *Image Processing, IEEE Transactions on*, 12(9):1094–1106, 2003.

[8] X. Zhou, J. Mateos, F. Zhou, R. Molina, and A. K. Katsaggelos. Variational dirichlet blur kernel estimation. *IEEE Transactions on Image Processing*, 24(12):5127–5139, Dec 2015.

[9] Jing Tian and Kai-Kuang Ma. A survey on super-resolution imaging. *Signal, Image and Video Processing*, 5(3):329–342, 2011.

[10] Yi Tang, Hong Chen, Zhanwen Liu, Biqin Song, and Qi Wang. Example-based super-resolution via social images. *Neurocomputing*, 172:38–47, 2016.

[11] Dandan Si, Yuanyuan Hu, Zongliang Gan, Ziguan Cui, and Feng Liu. Edge directed single image super resolution through the learning based gradient regression estimation. In *Image and Graphics*, pages 226–239. Springer, 2015.

[12] Yanzi Wang, Jiulun Fan, Jian Xu, and Xiaomin Wu. Learning-based super-resolution via canonical correlation analysis. *literatures*, 8(6), 2015.

[13] E.J. Candes and M.B. Wakin. An introduction to compressive sampling. *Signal Processing Magazine, IEEE*, 25(2):21–30, March 2008.

[14] M. Fornasier and H. Rauhut. Compressive sensing. In *Handbook of mathematical methods in imaging*, pages 187–228. Springer, 2011.

[15] EJ Candes and J Romberg. Practical signal recovery from random projections. *Wavelet Applications in Signal and Image Processing XI, Proc. SPIE Conf.*, 5914, 2005.

[16] Emmanuel J Candes and Terence Tao. Decoding by linear programming. *Information Theory, IEEE Transactions on*, 51(12):4203–4215, 2005.

[17] B. Amizic, L. Spinoulas, R. Molina, and A.K. Katsaggelos. Variational bayesian compressive blind image deconvolution. In *Signal Processing Conference (EUSIPCO), 2013 Proceedings of the 21st European*, pages 1–5, Sept 2013.

[18] W. AlSaafin, S. Villena, M. Vega, R. Molina, and A.K. Katsaggelos. Compressive sensing super resolution from multiple observations with application to passive millimeter wave images. *Digital Signal Processing*, pages 180–190, 2016.

[19] Wael Saafin, Miguel Vega, Rafael Molina, and Aggelos K. Katsaggelos. Image super-resolution from compressed sensing observations. In *Image Processing (ICIP), 2015 IEEE International Conference on*, pages 4268–4272, Sept 2015.

[20] Wael Saafin, Salvador Villena, Miguel Vega, Rafael Molina, and Aggelos K. Katsaggelos. Pmmw image super resolution from compressed sensing observations. In *Signal Processing Conference (EUSIPCO), 2015 23rd European*, pages 1815–1819, Aug 2015.

[21] Wael Saafin, Miguel Vega, Rafael Molina, and Aggelos K. Katsaggelos. Compressed sensing super resolution of color images. In *Signal Processing Conference (EUSIPCO), 2016 24th European*, Aug 2016.

[22] RY Tsai and Thomas S Huang. Multiframe image restoration and registration. *Advances in computer vision and Image Processing*, 1(2):317–339, 1984.

[23] Gabriel Cristóbal, Elena Gil, Filip Šroubek, Jan Flusser, Carlos Miravet, and Francisco de Borja Rodríguez. Superresolution imaging: a survey of current techniques. In *Optical Engineering+ Applications*, pages 70740C–70740C. International Society for Optics and Photonics, 2008.

[24] Hui Ji and Cornelia Fermuller. Robust wavelet-based super-resolution reconstruction: theory and algorithm. *Pattern Analysis and Machine Intelligence, IEEE Transactions on*, 31(4):649–660, 2009.

[25] Said E El-Khamy, Mohiy M Hadhoud, Moawad I Dessouky, Bassiouny M Salam, and FE Abd El-Samie. Regularized super-resolution reconstruction of images using wavelet fusion. *Optical Engineering*, 44(9):097001–097001, 2005.

[26] Nirmal K Bose, Nilesh Ahuja, et al. Superresolution and noise filtering using moving least squares. *Image Processing, IEEE Transactions on*, 15(8):2239–2248, 2006.

[27] Michael E Tipping and Christopher M Bishop. Bayesian image super resolution, September 12 2006. US Patent 7,106,914.

[28] Salvador Villena, Miguel Vega, Rafael Molina, and Aggelos K Katsaggelos. Bayesian super-resolution image reconstruction using an l1 prior. In *Image and Signal Processing and Analysis, 2009. ISPA 2009. Proceedings of 6th International Symposium on*, pages 152–157. IEEE, 2009.

[29] Richard R Schultz and Robert L Stevenson. Extraction of high-resolution frames from video sequences. *Image Processing, IEEE Transactions on*, 5(6):996–1011, 1996.

[30] S. Villena, M. Vega, S.D. Babacan, R. Molina, and A.K. Katsaggelos. Bayesian combination of sparse and non-sparse priors in image super resolution. *Digital Signal Processing*, 23(2):530–541, 2013.

[31] Lyndsey C Pickup, David P Capel, Stephen J Roberts, and Andrew Zisserman. Bayesian methods for image super-resolution. *The Computer Journal*, 52(1):101–113, 2009.

[32] Stefanos P Belekos, Nikolaos P Galatsanos, and Aggelos K Katsaggelos. Maximum a posteriori video super-resolution using a new multichannel image prior. *Image Processing, IEEE Transactions on*, 19(6):1451–1464, 2010.

[33] S.D. Babacan, R. Molina, and A.K. Katsaggelos. Variational bayesian super resolution. *IEEE Transactions on Image Processing*, 20(4):984–999, 2011.

[34] S. Farsiu, M.D. Robinson, M. Elad, and P. Milanfar. Fast and robust multiframe super resolution. *IEEE Transactions on Image Processing*, 13(10):1327–1344, 2004.

[35] Marcelo VW Zibetti, Fermín SV Bazán, and Joceli Mayer. Estimation of the parameters in regularized simultaneous super-resolution. *Pattern Recognition Letters*, 32(1):69–78, 2011.

[36] Antonio Marquina and Stanley J Osher. Image super-resolution by tv-regularization and bregman iteration. *Journal of Scientific Computing*, 37(3):367–382, 2008.

[37] Y. He, KH. Yap, L. Chen, and L-P Chau. A nonlinear least square technique for simultaneous image registration and super-resolution. *Image Processing, IEEE Transactions on*, 16(11):2830–2841, 2007.

[38] SS Panda, G Jena, and SK Sahu. Image super resolution reconstruction using iterative adaptive regularization method and genetic algorithm. In *Computational Intelligence in Data Mining-Volume 2*, pages 675–681. Springer, 2015.

[39] Jianchao Yang, John Wright, Thomas S Huang, and Yi Ma. Image super-resolution via sparse representation. *Image Processing, IEEE Transactions on*, 19(11):2861–2873, 2010.

[40] Kwang In Kim and Younghee Kwon. Single-image super-resolution using sparse regression and natural image prior. *Pattern Analysis and Machine Intelligence, IEEE Transactions on*, 32(6):1127–1133, 2010.

[41] Jinjun Wang, Shenghuo Zhu, and Yihong Gong. Resolution enhancement based on learning the sparse association of image patches. *Pattern Recognition Letters*, 31(1):1–10, 2010.

[42] Kamal Nasrollahi and Thomas B Moeslund. Super-resolution: a comprehensive survey. *Machine vision and applications*, 25(6):1423–1468, 2014.

[43] Antonin Chambolle, Vicent Caselles, Daniel Cremers, Matteo Novaga, and Thomas Pock. An introduction to total variation for image analysis. *Theoretical foundations and numerical methods for sparse recovery*, 9(263-340):227, 2010.

[44] Karl Nelson, Asim Bhatti, and Saeid Nahavandi. Performance evaluation of multi-frame super-resolution algorithms. In *Digital Image Computing Techniques and Applications (DICTA), 2012 International Conference on*, pages 1–8. IEEE, 2012.

[45] Ken D Sauer, Sean Borman, Charles Bouman, et al. Parallel computation of sequential pixel updates in statistical tomographic reconstruction. In *Image Processing, 1995. Proceedings., International Conference on*, volume 2, pages 93–96. IEEE, 1995.

[46] David Capel and Andrew Zisserman. Computer vision applied to super resolution. *Signal Processing Magazine, IEEE*, 20(3):75–86, 2003.

[47] Jean-Luc Starck, Michael Elad, and David L Donoho. Image decomposition via the combination of sparse representations and a variational approach. *Image Processing, IEEE Transactions on*, 14(10):1570–1582, 2005.

[48] Salvador Villena, Miguel Vega, S Derin Babacan, Rafael Molina, and Aggelos K Katsaggelos. Using the kullback-leibler divergence to combine image priors in super-resolution image reconstruction. In *Image Processing (ICIP), 2010 17th IEEE International Conference on*, pages 893–896. IEEE, 2010.

[49] A. Zomet, A. Rav-Acha, and S. Peleg. Robust super-resolution. In *Computer Vision and Pattern Recognition, 2001. CVPR 2001. Proceedings of the 2001 IEEE Computer Society Conference on*, volume 1, pages I–645–I–650 vol.1, 2001.

[50] Divya Gupta and Mahendra Kumar Patil. A review on image registration. *International Journal of Engineering Research Technology (IJERT)*, 3(2):2630–2633, 2014.

[51] Alan C Bovik. *Handbook of image and video processing*. Academic press, 2010.

[52] Netalee Efrat, Daniel Glasner, Alexander Apartsin, Boaz Nadler, and Anat Levin. Accurate blur models vs. image priors in single image super-resolution. In *Proceedings of the IEEE International Conference on Computer Vision*, pages 2832–2839, 2013.

[53] M.F. Duarte, M.A. Davenport, D. Takhar, J.N. Laska, Ting Sun, K.F. Kelly, and R.G. Baraniuk. Single-pixel imaging via compressive sampling. *Signal Processing Magazine, IEEE*, 25(2):83–91, March 2008.

[54] Wai Lam Chan, Kriti Charan, Dharmpal Takhar, Kevin F Kelly, Richard G Baraniuk, and Daniel M Mittleman. A single-pixel terahertz imaging system based on compressed sensing. *Applied Physics Letters*, 93(12):121105, 2008.

[55] W. L. Chan, K. Charan, D. Takhar, K. F. Kelly, R.G. Baraniuk, and D.M. Mittleman. A single-pixel terahertz imaging system based on compressed sensing. *Applied Physics Letters*, 93(12):121105–121105–3, Sep 2008.

[56] A. Heidari and D. Saeedkia. A 2d camera design with a single-pixel detector. In *Infrared, Millimeter, and Terahertz Waves, 2009. IRMMW-THz 2009. 34th International Conference on*, pages 1–2, Sept 2009.

[57] T. Li, X. Wang, W. Wang, and A. K. Katsaggelos. Compressive video sensing with limited measurements. *Journal of Electronic Imaging*, 22(4):043003–043003, 2013.

[58] A.C. Sankaranarayanan, C. Studer, and R.G. Baraniuk. Cs-muvi: Video compressive sensing for spatial-multiplexing cameras. In *Computational Photography (ICCP), 2012 IEEE International Conference on*, pages 1–10, April 2012.

[59] T. Edeler, K. Ohliger, S. Hussmann, and A. Mertins. Multi image super resolution using compressed sensing. In *Acoustics, Speech and Signal Processing (ICASSP), 2011 IEEE International Conference on*, pages 2868–2871, May 2011.

[60] A. Fannjiang and W. Liao. Super-resolution by compressive sensing algorithms. *CoRR*, abs/1211.5870, 2012.

[61] H.P. Babcock, J.R. Moffitt, Y. Cao, and X. Zhuang. Fast compressed sensing analysis for superresolution imaging using l1-homotopy. *Optics Express*, 21(23):28583–28596, 2013.

[62] J. Fang, J. Li, Y. Shen, H. Li, and S. Li. Super-resolution compressed sensing: An iterative reweighted algorithm for joint parameter learning and sparse signal recovery. *Signal Processing Letters, IEEE*, 21(6):761–765, June 2014.

[63] C. He, L. Liu, L. Xu, M. Liu, and M. Liao. Learning based compressed sensing for sar image super-resolution. *Selected Topics in Applied Earth Observations and Remote Sensing, IEEE Journal of*, 5(4):1272–1281, 2012.

[64] S. Yang, F. Sun, M. Wang, Z. Liu, and L. Jiao. Novel super resolution restoration of remote sensing images based on compressive sensing and example patches-aided dictionary learning. In *Multi-Platform/Multi-Sensor Remote Sensing and Mapping (M2RSM), 2011 International Workshop on*, pages 1–6. IEEE, 2011.

[65] P. Sen and S. Darabi. Compressive image super-resolution. In *Signals, Systems and Computers, 2009 Conference Record of the Forty-Third Asilomar Conference on*, pages 1235–1242, Nov 2009.

[66] L. Spinoulas, B. Amizic, M. Vega, R. Molina, and A.K. Katsaggelos. Simultaneous bayesian compressive sensing and blind deconvolution. In *Signal Processing Conference (EUSIPCO), 2012 Proceedings of the 20th European*, pages 1414–1418, Aug 2012.

[67] K. Koh, S. J Kim, and S. P Boyd. An interior-point method for large-scale l1-regularized logistic regression. *Journal of Machine learning research*, 8(8):1519–1555, 2007.

[68] M. Figueiredo, R. Nowak, and S. Wright. Gradient projection for sparse reconstruction: Application to compressed sensing and other inverse problems. *Selected Topics in Signal Processing, IEEE Journal of*, 1(4):586–597, 2007.

[69] D. Needell and J. A. Tropp. Cosamp: Iterative signal recovery from incomplete and inaccurate samples. *Applied and Computational Harmonic Analysis*, 26(3):301–321, 2009.

[70] S. Becker, J. Bobin, and E. J. Candès. Nesta: a fast and accurate first-order method for sparse recovery. *SIAM Journal on Imaging Sciences*, 4(1):1–39, 2011.

[71] J. Yang and Y. Zhang. Alternating direction algorithms for l1-problems in compressive sensing. *SIAM Journal on Scientific Computing*, 33(1):250–278, 2011.

[72] Waheed U Bajwa, Jarvis D Haupt, Gil M Raz, Stephen J Wright, and Robert D Nowak. Toeplitz-structured compressed sensing matrices. In *Statistical Signal Processing, 2007. SSP'07. IEEE/SP 14th Workshop on*, pages 294–298. IEEE, 2007.

[73] Gesen Zhang, Shuhong Jiao, Xiaoli Xu, and Lan Wang. Compressed sensing and reconstruction with bernoulli matrices. In *Information and Automation (ICIA), 2010 IEEE International Conference on*, pages 455–460, June 2010.

[74] Wotao Yin, Simon Morgan, Junfeng Yang, and Yin Zhang. Practical compressive sensing with toeplitz and circulant matrices. In *Visual Communications and Image Processing 2010*, pages 77440K–77440K. International Society for Optics and Photonics, 2010.

[75] Mohd Awais Farooque and Jayant S Rohankar. Survey on various noises and techniques for denoising the color image. *International Journal of Application or Innovation in Engineering & Management (IJAIEM)*, 2(11):217–221, 2013.

[76] Sumit Budhiraja Meenakshi. A survey of compressive sensing based greedy pursuit reconstruction algorithms. 2015.

[77] Honglin Huang and Anamitra Makur. Backtracking-based matching pursuit method for sparse signal reconstruction. *Signal Processing Letters, IEEE*, 18(7):391–394, 2011.

[78] Joel A Tropp and Anna C Gilbert. Signal recovery from random measurements via orthogonal matching pursuit. *Information Theory, IEEE Transactions on*, 53(12):4655–4666, 2007.

[79] Wei Dai and Olgica Milenkovic. Subspace pursuit for compressive sensing signal reconstruction. *Information Theory, IEEE Transactions on*, 55(5):2230–2249, 2009.

[80] Deanna Needell and Roman Vershynin. Signal recovery from incomplete and inaccurate measurements via regularized orthogonal matching pursuit. *Selected Topics in Signal Processing, IEEE Journal of*, 4(2):310–316, 2010.

[81] Mark A Davenport, Marco F Duarte, Yonina C Eldar, and Gitta Kutyniok. Introduction to compressed sensing. *Preprint*, 93:1–64, 2011.

[82] S-J Kim, K. Koh, M. Lustig, S. Boyd, and D. Gorinevsky. An interior-point method for large-scale l1-regularized least squares. *Selected Topics in Signal Processing, IEEE Journal of*, 1(4):606–617, Dec 2007.

[83] S Derin Babacan, Rafael Molina, Minh N Do, and Aggelos K Katsaggelos. Bayesian blind deconvolution with general sparse image priors. In *Computer Vision–ECCV 2012*, pages 341–355. Springer, 2012.

[84] Vinay Jeengar, SN Omkar, Amarjot Singh, Maneesh Kumar Yadav, and Saksham Keshri. A review comparison of wavelet and cosine image transforms. *International Journal of Image, Graphics and Signal Processing (IJIGSP)*, 4(11):16, 2012.

[85] Bruno Amizic, Rafael Molina, and Aggelos K Katsaggelos. Sparse bayesian blind image deconvolution with parameter estimation. *EURASIP Journal on Image and Video Processing*, 2012(1):1–15, 2012.

[86] S. Boyd, N. Parikh, E. Chu, B. Peleato, and J. Eckstein. Distributed optimization and statistical learning via the alternating direction method of multipliers. *Foundations and Trends® in Machine Learning*, 3(1):1–122, 2011.

[87] Y.-H. Xiao and Z.-F. Jin. An alternating direction method for linear-constrained matrix nuclear norm minimization. *Numerical Linear Algebra with Applications*, 19(3):541–554, 2012.

[88] R Tyrrell Rockafellar. *Convex analysis*. Number 28. Princeton university press, 1997.

[89] K. Lange. *Optimization*. Springer-Verlag, 2013.

[90] H. Chen, S. Lee, R. Rao, M. Slamani, and P. Varshney. Imaging for concealed weapon detection: a tutorial overview of development in imaging sensors and processing. *Signal Processing Magazine, IEEE*, 22(2):52–61, 2005.

[91] C. Zheng, X. Yao, A. Hu, and J. Miao. A passive millimeter-wave imager used for concealed weapon detection. *Progress In Electromagnetics Research B*, 46:379–397, 2013.

[92] J. Yang, J. Wang, and L. Li. A new algorithm for passive millimeter-wave image enhancement. In *Signal Processing Systems (ICSPS), 2010 2nd International Conference on*, volume 3, pages V3–507. IEEE, 2010.

[93] Y. Li, Y. Li, J. Chen, and Y. Hou. Passive millimeter-wave image restoration based on improved algorithm of nonlinear extrapolation in frequency space. *International Journal of Digital Content Technology and its Applications*, 5(5):42–49, 2011.

[94] P. Chen, T. Zou, J. Chen, Z. Gao, and J. Xiong. The application of improved pso algorithm in pmmw image ostu threshold segmentation. In *Applied Mechanics and Materials*, volume 721, pages 779–782. Trans Tech Publ, 2015.

[95] H. Lee, D. Lee, S. Yeom, J. Son, V. Guschin, and S. Kim. Passive millimeter wave imaging and analysis for concealed object detection. In *Data Mining and Intelligent Information Technology Applications (ICMiA), 2011 3rd International Conference on*, pages 98–101. IEEE, 2011.

[96] N. Gopalsami, S. Liao, T. W Elmer, E. R Koehl, A. Heifetz, A. C Raptis, L. Spinoulas, and A. K Katsaggelos. Passive millimeter-wave imaging with compressive sensing. *OPTICAL ENGINEERING*, 51(9), SEP 2012.

[97] N Gopalsami, TW Elmer, Shaolin Liao, R Ahern, A Heifetz, AC Raptis, M Luessi, D Babacan, and AK Katsaggelos. Compressive sampling in passive millimeter-wave imaging. In *SPIE Defense, Security, and Sensing*, pages 80220I–80220I. International Society for Optics and Photonics, 2011.

[98] V. Patel and J. Mait. Passive millimeter-wave imaging with extended depth of field and sparse data. In *Acoustics, Speech and Signal Processing (ICASSP), 2012 IEEE International Conference on*, pages 2521–2524. IEEE, 2012.

[99] A. Majumdar and R. Ward. Compressed sensing of color images. *Signal Processing*, 90(12):3122–3127, 2010.

[100] P. Nagesh and B. Li. Compressive imaging of color images. In *Acoustics, Speech and Signal Processing, 2009. ICASSP 2009. IEEE International Conference on*, pages 1261–1264. IEEE, 2009.

[101] Michael B Wakin, Jason N Laska, Marco F Duarte, Dror Baron, Shriram Sarvotham, Dharmpal Takhar, Kevin F Kelly, and Richard G Baraniuk. An architecture for compressive imaging. In *Image Processing, 2006 IEEE International Conference on*, pages 1273–1276. IEEE, 2006.